University of Alberta

A CASE STUDY: TIME-LAPSE SEISMIC MONITORING OF A THIN HEAVY OIL RESERVOIR

by

Yajun Zhang 

A thesis submitted to the Faculty of Graduate Studies and Research
in partial fulfillment of the requirements for the degree of

Doctor of Philosophy

in

Geophysics

Department of Physics

Edmonton, Alberta
Fall 2006

Your file Votre référence
ISBN: 978-0-494-23136-4
Our file Notre référence
ISBN: 978-0-494-23136-4

Abstract

This thesis presents a case study on time-lapse seismic monitoring. The target area is located at East Senlac in the vicinity of Alberta and Saskatchewan border, a heavy oil reservoir in the Western Canadian Sedimentary Basin. In order to observe rock property related seismic anomalies, two perpendicular seismic lines have been set up. One seismic line along the N-S direction is subject to Steam Assisted Gravity Drainage (SAGD) while the other seismic line along the W-E direction is not affected. This case study covers the subjects of feasibility study, processing strategy, repeatability evaluation, seismic attribute analysis, and impedance inversion.

Systematic feasibility study is conducted by prediction of rock properties based on Gassmann's equation, technical risk assessment, forward modelling and seismic survey design. The first stage simulation of oil substitution by steam indicates that it is feasible to perform time-lapse seismic monitoring project, but great challenge might be encountered. Continuous gas injection barely induces seismic variations. In the aspect of seismic data processing, better seismic quality is obtained by employing the prestack simultaneous processing (PSP) strategy. The three metrics, Pearson correlation, normalized root-mean-squares and predictability are employed to quantify the post-stack seismic repeatability. Higher repeatability along the W-E direction than along the N-S direction shows different local geology environment. The non-uniform CMP stack fold distribution is found the main factor to affect seismic repeatability. The seismic attribute, power spectra calculated from the N-S seismic surveys demonstrate that higher frequency energy tend to increase with time due to the possible decrease in pore pressure and pore tem-

perature. On the other hand, the inverted impedance using the recently proposed hybrid data transformation shows mixed impedance variations. The continuous gas injection and the simultaneous drop in temperature and pressure are possibly the main reason to result in this mixed impedance variations.

Acknowledgements

First of all, I would like to thank my supervisor Dr. Douglas R. Schmitt for his time, effort, guidance and financial support. I would also like to thank Wendell Pardasie, Dean Rokosh, Michael Lazorek, Mahmadou Diallo, Yingbin Liu, Marek Welz and Len Tober who helped acquire seismic data. Thanks for Geophysical Exploration and Development Corporation (GEDCO) the permission of use of VISTA software and Colorado School of Mines to allow the use of Seismic Unix (SU) software.

I extend my appreciation to my examining committee members for agreeing to read my thesis and for their valuable suggestions.

I would also like to acknowledge Jason (Zhigang) Han, Juefu Wang, Henning Kuhl, Ulrich Theune and my other fellow students for many fruitful discussions at the University of Alberta. Many thanks to the administrative support from Lynn Chandler and Sarah Derr. Funding for this work initially came through the Seismic Heavy Oil Consortium and the sponsors of that work are thanked for the funding that allowed for the data in this thesis to be collected as well as fund portions of my stipend during my stay at the University of Alberta. The latter parts of my work were supported by the Discovery grant to Dr. Schmitt from Natural Sciences and Engineering Research Council of Canada.

To all of my friends, I extend my gratitude for their kindness, support and encouragement throughout all these years. Special thanks go to Nana Li for the many enjoyable hours of swimming and playing badminton.

Finally, I would like to thank my family for always being there to support me and for always having confidence in me.

Contents

List of Tables

List of Figures

List of symbols

Δ Increment

$\delta(t)$ Unit impulse function

ε Constant

η Viscosity

κ Permeability

λ Seismic wavelength

μ_d Shear frame modulus

μ_{eff} Effective shear modulus

ρ_0 Reference density

ρ_d Dry sample density

ρ_{eff} Effective mass density

ρ_f Fluid mass density

ρ_{Me} Methane density

ρ_O Oil density

ρ_s Solid material mass density

ρ_{St} Steam density

ρ_W Water density

σ Standard deviation.

τ Time delay

ϕ Porosity

ω Angular frequency

API Fluid density defined by American Petroleum Institute

$BPEM$ Bandwidth and phase equalization method

CDP Common depth point

CMP Common mid point

EOR Enhanced oil recovery

ES East Senlac

f Seismic frequency

GHG Green house gas

GOR Gas-oil-ratio

Hz Hertz

$\mathbf{I}$ Identity matrix

I_{im} Impedance

I_p Acoustic impedance

ICM Iterated conditional modes

IWM Iterated window maximization

K_{cp} Fluid compress contrast

K_d Bulk frame modulus

K_{eff} Effective bulk modulus

K_f Fluid bulk modulus

K_{Me} Methane bulk modulus

K_O Oil bulk modulus

K_s Bulk modulus of the solid minerals

K_{St} Steam bulk modulus

K_W Water bulk modulus

L Lumley

L_c Spatial diffusion scale between uniform and patchy saturation

MFM Matched filtering method

NMO Normal move out

$NMO_{stretch}$ Normal move out stretch

$NRMS$ Normalized root mean squares

PCS Published case study

$PEAR$ Pearson correlation

PPP Prestack parallel processing

$PRED$ Predictability

PSP Prestack simultaneous processing

RMS Root mean squares

S_{Me} Methane saturation

S_O Oil saturation

S_{St} Steam saturation

S_W Water saturation

SA Simulated annealing

$SAGD$ Steam assisted gravity drainage

$SMLR$ Single most likely replacement

t Time

u Unit function

v_{NMO} Stacking velocity

V_P P-velocity

V_S S-velocity

VSP Vertical seismic profile

w Source wavelet

x Offset

XEQ Cross-equalization

Preface

Geophysics is a comprehensive subject, one goal of which is to probe the interior of the earth. The purpose of geophysical science is to describe, interpret, and understand the subsurface structures and the processes active within the earth. Exploration geophysicists, in particular, have long attempted to image geological structure in order to discover potential natural resources. However, the focus of applied petroleum geophysicists is now shifting from exploration to production; geophysical methods are being adapted to monitor both the reservoir production and the local environment in addition to searching for resources.

Using geophysical methods to monitor potential subsurface changes, especially fluid flow movement, has been an active area of investigation during the last decade (e.g. *Greaves and Fulp*, 1987; *Nur*, 1989). The variations in a geophysical response can be observed with repeated surveys acquired at the same location. This is the so called time-lapse geophysics. Usually, time-lapse techniques have different requirements from conventional surveys although there remains a great deal of inertia due to the success of traditional methods in imaging complex structures. Most current surveys employ techniques developed from the perspective of seismic exploration for structural or stratigraphic traps of oil or gas. Such studies are usually carried out over many kilometres of 2D lines or many square kilometers in 3D surveys. These may not be optimal for acquiring appropriate seismic data at the scale necessary for adequate monitoring of fluid movement. In the design of an optimal data acquisition system, cost-efficiency, fidelity, resolution, and repeatability are the major concerns.

As conventional petroleum resources are depleted, more and more hydrocarbons necessary to power much of modern civilization will come from non-conventional reserves. Heavy oils and bitumens are one large component of these "new" resources, especially

in the Western Canadian Sedimentary Basin. However, such heavy oils are too viscous to be produced by conventional methods. Thus, techniques such as steam assisted gravity drainage (SAGD) are employed to enhance heavy oil recovery. During the process of steam or gas injection, fluid-flow variations within the reservoir can be potentially monitored from seismic data. Sometimes, bypassed oil zones can also be identified.

Interpretation of time-lapse data requires information from a variety of sources. This mainly includes knowledge from rock property measurements of the core and geophysical log samples, in situ temperatures, pore pressures, confining stresses, knowledge from fluid saturations, production and injection history data, geological model construction, reservoir simulation, and forward seismic modelling. Although the generated forward seismic modelling may not completely represent the real situation, it can provide insight into active reservoir processes on the meaning of observed geophysical changes in terms of the variations in the rock properties. The well log data can provide the fundamental geological and physical parameters which can be used to generate forward seismic modelling. The forward seismic modelling can, in turn, help understand how seismic response changes with different rock property parameters. Introducing changes to this starting point can also be helpful to verify the validity of the temporal seismic variations. This, in turn, helps optimize the seismic processing scheme. A quantitative interpretation can be attempted once the rock property parameters are properly inverted from the time-lapse seismic data.

This thesis mainly focuses on a case study of a 'Lloydminster style' heavy oil reservoir from west-central Saskatchewan. The steps to accomplish this include the construction of geological and a corresponding physical property models, generation of a forward seismic model leading to the prediction and interpretation of seismic variations under *in-situ* reservoir conditions. This requires the solution of a number of technical problems associated with development of time-lapse seismic data processing protocols, evaluation and quantification of seismic repeatability, and interpretation of time-lapse seismic variations by integrating extracted seismic attributes, inverted acoustic impedance, and simulated time-lapse rock properties.

Heavy oil and recovery technology

According to *Cupcic* (2003), heavy oil can be broadly classified as four types based on downhole viscosity. The first type is medium heavy oil. The viscosity is located within the range (0.01Pa·s, 0.1Pa·s). The second type is called extra heavy oil. The corresponding viscosity is within the range (0.1Pa·s, 10Pa·s). These two types of oil are mobile at reservoir conditions. The third type is tar sands and bitumen. The viscosity is greater than 10 Pa·s. Such oil is not mobile under normal reservoir conditions. The last type is oil shales. The source of reservoir is the solid kerogen that forms a substantial fraction of the rock itself. Oil shales are for all practical purposes impermeable and hydrocarbons are obtained by first mining and then 'retorting' the material.

Based on the present statistics (e.g. *Cupcic*, 2003), huge potential heavy oil reserves have been found. They are equivalent to the worldwide conventional oil reserves. However, eighty percent of the heavy oils are distributed as extra heavy oil, tar sands and bitumen. The largest deposits have been found in Canada and Venezuela. Worldwide, less than 1% of the heavy oils have been produced or are under active production. This is because the production capacity is limited by the viscosity limited recovery factors and because the heavy oils and bitumens contain less of the more desirable lighter hydrocarbons employed in transportation fuels and until recently were not as desirable. There are a variety of technologies used to produce such heavy oils. These include mining extraction, cold production, and many varieties of steam or solvent injection have already been successfully used in practice. These technologies all have their own advantages and disadvantages.

In Alberta, bituminous sands are mined directly in some of the largest mining operations on earth. Currently, there are three operational mines extracting ore from the Athabasca oil sands near Fort McMurray, Alberta, with more mines currently in the development stage. In these processes, the oil sand 'ore' is directly dug out of the earth and shipped to separation facilities where the bitumen is separated from the sand and other materials. This bitumen is then upgraded by the addition of hydrogen to make a synthetic crude. These mines today produce upwards of 30% of Canada's needs, a percentage that is likely only to increase as the production of conventional oil within the

Western Canada Sedimentary Basin continues to decrease annually by nearly 10%, as mining extraction technologies have a high recovery factor and limited green house gas (GHG) emissions. The amount of the resource that may be extracted in this fashion, however, is limited to those near surface reserves that may be economically extracted. It is estimated that upwards of 90% of the Athabasca reservoir, however, is too deep for mining to be effective and in this situation in situ extraction technologies must be employed.

Cold production is a proven technology. Within the family of *in situ* production technologies, so called cold heavy oil production (CHOP) is the simplest. In this technology, sand is produced with the heavy oil, the sand-oil mixture is removed using a special augur pump constructed of a long lasting elastometric material that does not wear as quickly as metal would under such circumstances. It has the advantages of lower cost and no GHG emissions. But its disadvantage is that less than 15% of the oil in place may be recovered with typical recovery factors of only 5 to 10%. This process is not suitable for very heavy oils and bitumens because the oil still must flow. As well, it is unknown whether this process is advantageous to longer term production of the reservoir.

Huff and puff technology is also a proven technology. The advantage is that it requires limited costs. The disadvantage is that recovery factors are only 15% to 20%. It also has the problems of high energy consumption and consequent GHG emissions.

More efficient technologies, such as *in-situ* combustion (e.g. *Greaves and Fulp*, 1987) or solvent injection (e.g. *Johnstad et al.*, 1995; *Meunier and Huguet*, 1998; *Harris et al.*, 1996), have been developed. The *in-situ* combustion technology, firstly developed in 1960's, has been shown to have high recovery efficiency which reaches as high as 60%. However, fewer successful operations have been reported so far. This is mainly due to the operational and safety problems. Another technology, solvent injection, has similar recovery factors. However, this technology is not mature enough for industrial application due to the slow diffusion and the difficult initial start-up.

Since the 1980's, more mature and efficient technologies, such as Steam Assisted Gravity Drainage (SAGD) (*Butler and Yee*, 2002, e.g.), are the proven technologies, and have been used for several pilot projects in Alberta and elsewhere. They have the advantages of quick thermal diffusion and up to 60% high recovery factors. However, huge energy inputs are required with corresponding large GHG emissions produced in the ap-

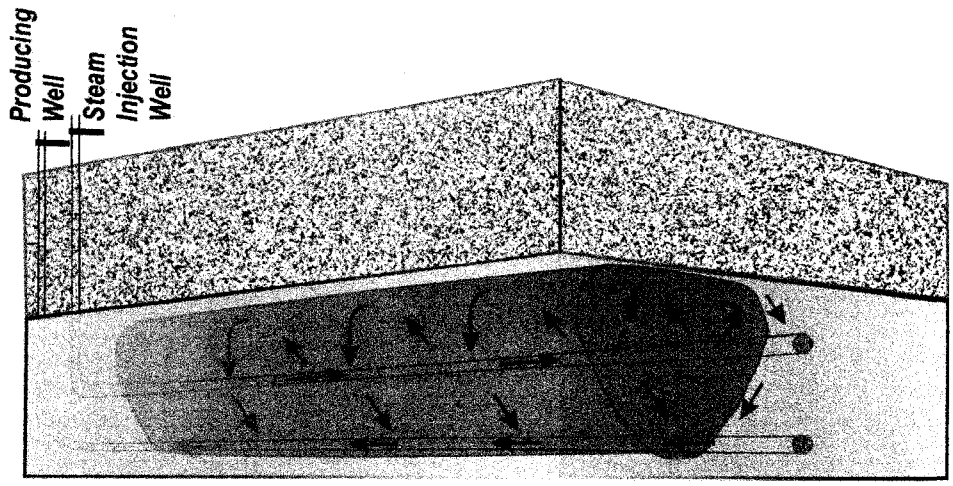

Figure 1: Caricature of the SAGD process.

plication of this technology. As such any improvements to the method, even incidental ones, should be welcome. Seismic monitoring is one such technique that has the potential to allow for greater efficiencies. In this thesis, a SAGD process is monitored and more details on this are provided in the next section.

SAGD and seismic monitoring

During the process of SAGD (see Figure 1), steam is continuously injected into an upper horizontal well which is located about 2-5 meters above and parallel to a lower horizontal producing well near the base of the reservoir. The steam gradually heats the surrounding heavy oil, and therefore reduces the oil viscosity. Most of the produced oil is thought to come from the perimeter of the steam chamber with the temperature about 2-30°C cooler than in the steam chamber. During this process, the injected steam rises to the top of the reservoir and fills the originally oil occupied volume. Generally, prior to the onset of oil production, steam is injected into both horizontal wells to establish communication. Once the economic limit of steam injection is reached, steam injection ceases, and non-condensable gas is injected to maintain steam chamber pressure and to act as insulation to thermal heat loss. The injected gas gradually migrates toward the edge of the steam chamber, and interfingers with the reservoir. However, gas preferentially rises at the

expense of lateral expansion. Furthermore, the injected gas, to a small extent, lowers the average temperature of the steam chamber. This process is similar to what was employed in the East Senlac, Saskatchewan, and that is the focus of this study.

In this thesis, a number of aspects of time lapse geophysical factors on the monitoring of SAGD scenario are developed. SAGD is a relatively expensive process and as such there should be a large potential for geophysical monitoring to assist. It is useful to note that all of the enhanced oil recovery techniques are not infallible. However, failure of such methods are never reported in the literature or open press. For example, a serious problem is caused by blockage of flow wither by improper well completion or by the heterogeneity of the reservoir itself. Geophysical technique can help to locate such problems.

Scope of the thesis

Chapter 1 - Introduction

Time-lapse seismic studies rely on changes in the physical properties due to variations in the *in situ* conditions. In this chapter, rock physics as the basis of time-lapse seismic monitoring will be briefly described. The factors which will affect seismic velocities will be analyzed. These factors mainly include the fluid composition, the temperature, and the pressure. Additionally, recent development on time-lapse seismic monitoring will be briefly reviewed from the published case studies.

Chapter 2 - Time-lapse seismic impedance inversion by using the hybrid data transformation method

In time lapse seismic studies, the reservoir is described in terms of its seismic velocity and density structure, the product of which is called impedance. In this chapter, a new method to invert impedance variations by using the hybrid data transformation will be proposed and will be tested on the two typical models including the triangle structure and the thin-bed structure. These models simulate structures that might be encountered in real reservoirs.

Chapter 3 - Background to the Senlac case study: An assessment of the feasibility of time lapse seismic monitoring

It is important to attempt to understand what kind of changes may be induced in the reservoir during production in order to assess the feasibility of time lapse studies and to provide insight on future interpretation. In this chapter, geology and reservoir characters for East Senlac area, the site of the case studies outlined in this thesis, will be briefly described. Then feasibility study will be systematically analyzed. Four aspects are involved in this feasibility study, including elastic parameter estimation, technical risk assessment, forward seismic modelling generation, and time-lapse seismic survey design.

Chapter 4 - The art of time-lapse seismic data processing

In general, processing of time lapse seismic data requires more care to preserve the data fidelity and to allow for meaningful comparisons later. In the first part, the general time-lapse seismic processing strategies will be described in detail. Meanwhile, the difference between different processing schemes will be compared through illustrated numerical examples. In the second part, the basic principles of cross-equalization will be described. The difference between the two methods, matched filtering and bandwidth-phase equalization will be compared. The strategies of how to cross-equalize the East Senlac seismic surveys will also be presented.

Chapter 5 - Seismic repeatability study

This study is unique in that a number of measurements were made at different dates and a good deal of effort was taken to ensure repeatability as much as possible. Consequently, in this chapter, seismic repeatability will be systematically investigated. This includes the repeatability analysis on the shot and geophone positions, the source signatures, and the final post-stack seismic profiles. The three metrics including Pearson correlation, predictability, and normalized root-mean-squares will be employed in the quantified repeatability analysis of post-stack seismic data.

Chapter 6 - Time-lapse seismic attribute analysis and integrated interpretation

In this chapter, we attempt to integrate the seismic and production information. In the first part, the recorded East Senlac SAGD history data will be presented and time-lapse rock properties will be simulated. In the second part, seismic attribute, the power spectrum and the cumulative power spectrum along the W-E direction and along the N-S direction will be calculated. Different geologic environments will be diagnosed based on the different features of the extracted seismic attributes. In the third part, as a complimentary seismic attribute, the time-lapse seismic "impedance" will be inverted by using the recently proposed hybrid data transformation method. The inverted "impedance" will be interpreted with the assistance of the simulated time-lapse rock properties.

Discussion and Conclusions

This consists of a discussion of the successes and the failures in this thesis. As well, some thoughts as to future research directions for time lapse seismology are necessary. All the published abstracts since 2002 are listed in *Zhang et al.* (2002), *Zhang and Schmitt* (2002), *Zhang and Schmitt* (2003b), *Zhang and Schmitt* (2003a), *Zhang and Schmitt* (2004a), *Mu et al.* (2004), *Zhang and Schmitt* (2004b), *Zhang and Schmitt* (2005a), and *Zhang and Schmitt* (2005b).

Chapter 1

Introduction

Time-lapse seismic monitoring is the process of acquiring and analyzing multiple seismic surveys which are repeated at the same site over calendar time. The main purpose is to image fluid-flow effects in a producing reservoir. If each survey is "3-D seismic", then the resulting set of time-lapse data is called "4-D seismic", with the fourth dimension being calendar time. In addition to 4-D seismic, there are some other types of time-lapse seismic monitoring including repeated 2-D surface seismic, surface-to-borehole vertical seismic profile (VSP), and borehole-to-borehole cross-well seismic geometries.

The potential advantage of time-lapse seismic monitoring is the ability to detect subsurface rock property variations in areas not directly sampled by the wells. The basic premise of time-lapse seismic monitoring is to diagnose and to isolate rock property variations distributed within the reservoir area during the process of production. In two or more time-lapse seismic surveys, the differences in the seismic images should only be due to production induced variations rather than variations due to differences in seismic acquisition or processing. This is the basic concept of time-lapse seismic reservoir monitoring.

In the first part of this chapter, rock physics as the basis of time-lapse seismic monitoring will be described. In the second part, development on time-lapse seismic monitoring will be reviewed from the published case studies.

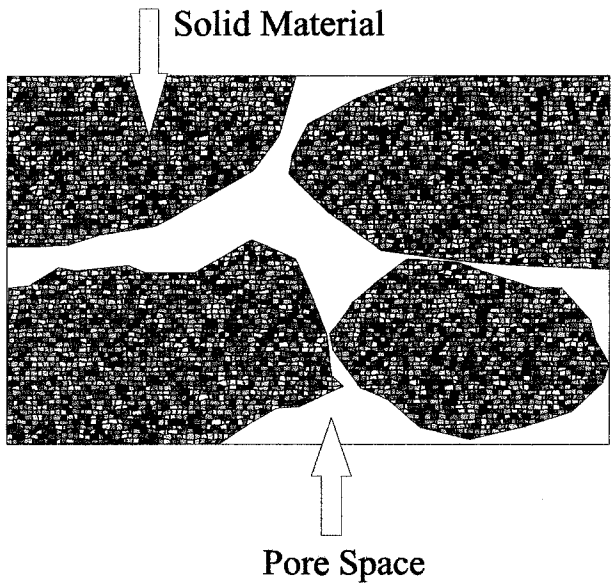

Figure 1.1: Cartoon of porous rock.

1.1 Rock physics as the basis of seismic monitoring

Propagation of seismic waves through the earth depends on the subsurface media composition. The *in situ* velocities are determined by many factors including the composition, porosity, confining stress, pore fluid pressure, temperature, and elastic properties of the material, to name only a few. Generally, three traditional disciplines are involved in time-lapse seismic monitoring: fluid flow simulation, rock physics, and reflection seismology. The fluid flow equations of reservoir simulation attempt to describe changes in pore pressure, temperature and multi-phase saturations resulting from production and injection of fluids in porous media. Rock physics, as a bridge between fluid flow and reflection seismology, transforms these engineering parameters to seismic compressional-wave and shear-wave propagation velocities and elastic impedances. The cartoon of porous rock is illustrated in Figure 1.1. Wave theory describes the propagation of seismic waves through such media and how the reflected amplitudes and travel times, which contain fluid flow information, are appropriately quantified. As the basis of seismic monitoring, rock physics will be described in this section.

1.1.1 Saturated rock properties

The P-wave V_P and S-wave V_S velocities for an isotropic rock can be formulated as (e.g. *Lay and Wallace*, 1995):

$$V_P = \sqrt{\frac{K_{eff} + 4/3\mu_{eff}}{\rho_{eff}}} \tag{1.1}$$

$$V_S = \sqrt{\frac{\mu_{eff}}{\rho_{eff}}} \tag{1.2}$$

where K_{eff}, μ_{eff}, and ρ_{eff} individually represents the effective bulk modulus, the effective shear modulus, and the effective mass density. The V_P and V_S are the estimated velocities for the fluid-saturated porous medium. The effective bulk modulus K_{eff} principally depends on four parameters, including the bulk modulus of the solid minerals (K_s), the fluid bulk modulus (K_f), the bulk modulus of the rock matrix frame (K_d), and the porosity (ϕ). These elastic parameters are implicitly dependent on confining and pore fluid pressure, fluid saturation, and temperature. Damage to the reservoir may be another factor which has not been considered in most studies.

The effective bulk modulus K_{eff} can be estimated by using Gassmann's equation (*Gassmann*, 1951; *Berryman*, 1999):

$$K_{eff} = K_d + \frac{(1 - K_d/K_s)^2}{(1 - K_d/K_s - \phi)/K_s + \phi/K_f} \tag{1.3}$$

Application of Gassmann's equation is based on several assumptions. The first assumption is that the rock properties are homogeneous and isotropic, and that the whole pore space is completely connected. The second assumption is that Gassmann's equation is valid only at low enough frequencies so that pore pressures are equalized over a scale which is much greater than a pore dimension, and much less than the wavelength of the passing seismic wave. This implies that pore fluid moves together with the rock frame.

Gassmann's theory is expected to predict the behavior of the material as the frequency approaches zero and consequently Gassmann's formula applies only in the limit of low frequency. There remains a good deal of discussion with regards to the validity of applying Gassmann's relation to seismic wave propagation. More involved theories, such as those developed by *Biot* (1966) for 'global flow' or by *Mavko and Mukerji* (1998) for 'local flow', attempt to overcome this low frequency assumption. Here, however, it is

assumed that Gassmann's formula will adequately provide us with indications of the elastic changes expected within the porous and saturated rock for purposes of modelling while recognizing that in many ways relying on this assumption may be deficient. One further assumption is that the problem may be considered as purely mechanical; other chemical, surface tension, or mineral surface wetting issues are ignored.

The effective shear modulus μ_{eff} is usually assumed to not be affected by fluid saturation, and to be equal to the shear frame modulus, μ_d,

$$\mu_{eff} = \mu_d \tag{1.4}$$

The effective or bulk density ρ_{eff} for the saturated rock is given by the formula:

$$\rho_{eff} = (1 - \phi)\rho_s + \phi\rho_f \tag{1.5}$$

here ρ_s is the density of solid material, and ρ_f is the fluid density distributed within pore space. The fluid density ρ_f can be calculated by the following weighted sum:

$$\rho_f = \sum_{i=1}^{N} S_i\rho_i, \tag{1.6}$$

Here S_i is the saturation of the i^{th} fluid component, and ρ_i is its density. This of course assumes that the fluids are immiscible.

Gassmann's equation 1.3 looks complicated but is simple to calculate if the requisite moduli and the porosity are known. Usually it is straightforward to obtain values of K_f and K_s under the conditions expected *in situ*. However, the drained modulus is much more difficult to obtain. Gassmann himself used a pack of spherical mineral grains to attempt to obtain some representative values for these moduli. The problem essentially depends on numerous factors, the most important of which is the character of the porosity within the material. Hence, empirical methods in which K_d is determined as a function of effective pressure and temperature are often important. The frame bulk modulus K_d and the frame shear modulus μ_d can be calculated by using the laboratory measured velocities of the rock frame (e.g *Theune*, 2003). This experiment conceptually should be carried out at zero frequency by allowing fluid to flow unrestrictedly out or into the pore space. In practice, it is often assumed that the measurement of a "dry" sample provides

an adequate measure of these frame moduli which can be expressed as:

$$K_d = \rho_d(V_P^2 - 4/3V_S^2) \tag{1.7}$$

$$\mu_d = \rho_d V_S^2 \tag{1.8}$$

In general, if the pore fluids include more than two phases, a mixture's effective fluid bulk modulus K_f can be estimated according to the number of fluid components, saturations, and bulk moduli:

$$\frac{1}{K_f} = \sum_{i=1}^{N} \frac{S_i}{K_i} \tag{1.9}$$

$$K_f = \sum_{i=1}^{N} S_i K_i \tag{1.10}$$

The formula 1.9 is valid for immiscible fluids which are mixed uniformly at very small scales (also called Reuss average effective fluids). Formula 1.10 is applicable for the fluids which are heterogeneous in saturations over scales larger than the characteristic diffusion length. This phenomena is also called patchy saturation (*Mavko and Mukerji*, 1998) which gives an upper bound. The corresponding fluids are also called Voigt average effective fluids. For the Reuss average effective fluids, pore pressure can equilibrate over spatial scales smaller than: $L_c \approx \sqrt{\kappa K_f / f\eta}$, where f is seismic frequency, κ, permeability, η, viscosity, and K_f fluid phase bulk modulus (*Mavko and Mukerji*, 1998). Sometimes, pore pressure can be disturbed, e.g. by local fluid flow with the presence of open microcracks (*King and Marsden*, 2002).

According to *Mavko and Mukerji* (1998), critical saturation scales separating uniform from patchy behavior are typically of the order 0.1-1cm for laboratory measurements and tens of centimeters for field seismic frequencies. For low seismic frequencies, the velocities corresponding to patchy (Voigt) and uniform (Reuss) saturations provide the upper and lower bounds expected for the given saturations. For well consolidated rocks, both the upper and lower bounds can be estimated by using Gassmann's relations with Voigt or Reuss average effective fluids. For the unconsolidated or high porosity rocks, effects of patchy saturation become more important and should be considered, especially when modelling the time-lapse seismic response which is dependent on velocity distribution (*Smith et al.*, 2003).

1.1.2 Velocity variations due to the pore fluid composition, pressure and temperature

Pore fluid composition effect on velocity

Since elastic moduli and density of any mixture can be calculated under fixed temperature and pressure, the compressional velocity and shear velocity can be estimated by using formulas 1.1 and 1.2. In principle, the variations in seismic velocity with different pore fluids can be monitored during the process of enhanced oil recovery. For example, if all the gas in the pore space is replaced by fluid, the compressional velocities will increase significantly under the constant pressure and temperature. However, velocity variations become complicated during the process of oil substitution by steam. Figure 1.2 shows how compressional and shear velocity ideally change during this process. In this example, the confining pressure is assumed to be 20 MPa and the pore pressure 5 MPa. Effective pressure (the difference between confining pressure and pore pressure) remains at the constant 15 MPa. The initial oil saturation is assumed to be 85%, and the water saturation 15%. During the thermal process that reservoir temperature rises from 30°C to 200°C, it is observed from Figure 1.2 that the V_P decreases significantly with steam saturation. When the hot steam with 275°C gradually increases to substitute the 200°C oil, the V_P decreases rather quickly when the steam saturation is less than 4%. After that, the V_P quasi-linearly increases with steam saturation. In contrast, during the same process, all the shear velocity V_S increases linearly with the steam saturation.

Temperature effect on seismic velocities

Temperature dependent variations of seismic velocities are mainly due to the rock property variations represented by the two parameters, the bulk modulus and the density. In general, when temperature increases, compressional velocity usually decreases, and shear velocity increases slightly. But this is not always the case. In some special cases, shear wave velocity may decrease slightly (e.g. *Timur*, 1977; *Eastwood*, 1993). Much of the decline in compressional velocity in saturated rocks is due to decreased values of K_f.

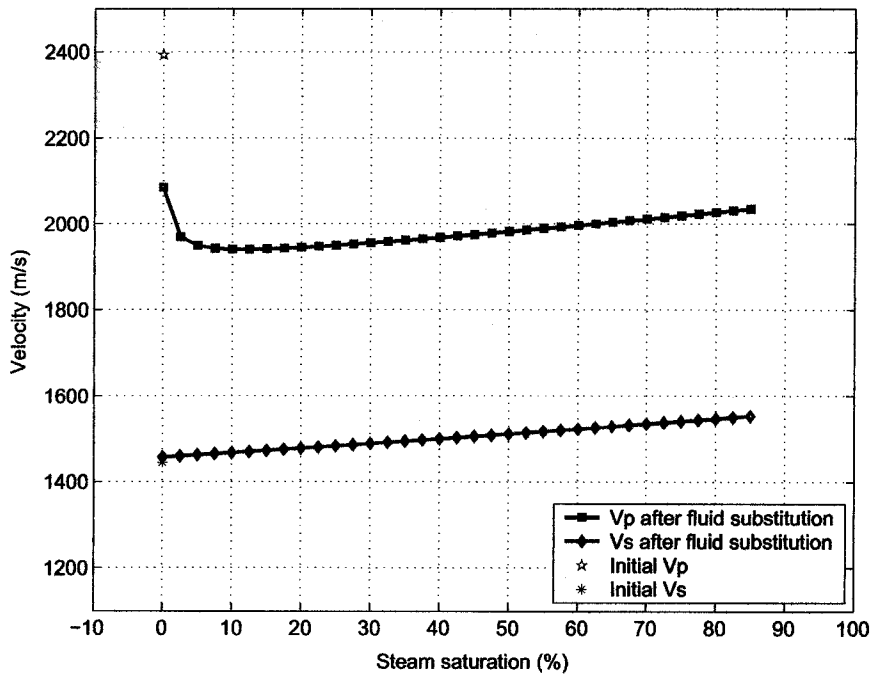

Figure 1.2: The estimated compressional velocity and shear velocity subject to thermal and fluid substitution processes.

Pressure effect on seismic velocities

There are two concepts essential to understand seismic velocities which change as a function of pressure. The first concept is that of the lithostatic pressure and the tectonic stresses which are essentially the load of the vertical overburden and the loading due to plate tectonic or other regional effects, respectively. In laboratory measurements, this pressure is called the confining pressure. The second concept is pore pressure. It is the pressure of the fluids that reside in the pore space. The effective pressure that acts on materials is usually taken to be the simple difference between lithostatic pressure (or confining pressure) and pore pressure. The moduli of rocks can be highly dependent on the effective pressure and consequently changes in the effective pressure will result in variations in the seismic velocities. During the SAGD process with the lithostatic pressure remaining constant, pore pressure will change when steam is injected and fluids are removed. As such, changes in physical properties with effective pressure may need to be considered.

Usually, velocities tend to increase with the effective pressure (e.g. *King*, 1966; *Christensen and Wang*, 1985a,b; *Han et al.*, 1986; *Eberhart-Phillips et al.*, 1989). The explanation for this behavior is that the pores close at higher pressures. This compaction consequently increases the effective stiffness of the rock and results in the better grain - to - grain coupling which directly leads to the velocity increase. This increase, however, is not unlimited. Once all cracks and pores are closed, despite the continuous increase in the effective pressure, the velocity only increases slightly. However, we can usually safely ignore variations in the mineral properties over the range of pressure and temperature encountered in a typical heavy oil reservoir although more study of clays in particular is needed. When the effective pressure remains constant, the velocity is usually considered not to change (e.g. *Wyllie et al.*, 1958; *Christensen and Wang*, 1985b) in clean sandstone rocks. However, as a special case, for example, the highly compressible clay is filled inside grains and pores, velocity will change, i.e., compressional velocity increases and shear velocity decreases (e.g. *King*, 1966; *Christensen and Wang*, 1985a). In this case, velocity will change under the constant effective pressure with the same increment in the pore pressure and in the confining pressure. There are other factors that are now only

being considered in time lapse monitoring. An important one is likely the fact that during production the materials themselves are changed, a variation that may be referred to as damage. Rocks can either dilate or compact. The oil sands may be a special case as it is believed that heavy oil portions may even provide some of the supporting cementing material, this 'cement' will be removed with heating.

1.2 Time-lapse seismic monitoring development

Some of the initial concepts of time-lapse seismic monitoring were inspired by rock property measurements in the mid 1980s at Stanford University. *Nur et al.* (1984) suggested that a large velocity decrease might be observed in repeated subsurface seismic surveys during thermal enhanced oil recovery (EOR) process, especially during the process of steam injection. In the mid-late 1980s and early 1990s, in order to enhance oil recovery, several initial field experiments have been conducted in Canada (e.g. *Pullin et al.*, 1987; *Eastwood et al.*, 1994) and Indonesia (e.g. *Lumley et al.*, 1995) by injecting steam, and in the US (e.g. *Greaves and Fulp*, 1987) by fire flooding. Subsequent projects have been carried out in order to monitor isothermal gas-fluid movement in the North Sea (*Johnstad et al.*, 1995) and in the Paris basin (*Meunier and Huguet*, 1998).

A variety of factors directly affect the results of time-lapse seismic monitoring. These factors include the reservoir rock and fluid properties, the *in situ* pore pressure and pore temperature, the seismic acquisition, processing, and interpretation. Generally, in order to ensure the success of time-lapse seismic monitoring, it is essential to perform feasibility study to assess the potential risk involved. This can be accomplished by employing the most widely used technical spreadsheet proposed by *Lumley et al.* (1997). As for other aspects including seismic acquisition, processing, and interpretation, the relevant technologies are still in development and we hope to make new contributions in this thesis.

1.2.1 Rock physics as the basis of time-lapse seismic monitoring

The first public domain quantitative laboratory measurements on heavy-oil saturated core samples were conducted at Stanford University in the mid 1980s. The experiments have indicated that a dramatic ultrasonic velocity decrease was observed when these

samples were heated (*Nur et al.*, 1984; *Wang and Nur*, 1986, 1990; *Nur*, 1989). Continuous gas injection without changing the temperature further reduced velocity (*Nur*, 1989). Based on these laboratory observations measured on the heavy-oil saturated core samples, *Nur et al.* (1984) predicted that there would be a high probability of success in monitoring thermal EOR fronts if the seismic energy and the seismic resolution were adequately set. However, rock properties themselves are found also to have significant impact on this process.

Based on rock physical property measurement, several time-lapse seismic monitoring field experiments have been conducted (e.g. *Pullin et al.*, 1987; *Eastwood et al.*, 1994; *Lumley*, 1995; *Lumley et al.*, 1995; *Jenkins et al.*, 1997) during steam injection into heavy oil reservoirs.

In addition to steam injection, gas injection such as methane and CO_2 has also been used to enhance oil recovery and to monitor gas-fluid movement. This has been demonstrated by the laboratory measurement conducted by *Domenico* (1976) which shows that a rock's impedance, the product of compressional wave velocity and density, can be greatly reduced in the presence of free gas in a reservoir without changing temperatures. Several pilot projects have been carried out by injecting gas. The well known gas monitoring projects include the North Sea gas cap expansion (e.g. *Johnstad et al.*, 1995), the Paris basin gas storage project (e.g. *Meunier and Huguet*, 1998), and the west Texas CO_2 injection (e.g. *Harris et al.*, 1996).

From the published case studies, it is found that reservoirs with high gas-oil-ratio (GOR) oil and unconsolidated high-porosity sands have the greatest success opportunity for time-lapse seismic monitoring (e.g. *Anderson et al.*, 1997; *Sonneland et al.*, 1997; *Ebrom and Scott*, 1998; *Hirsche and Harmony*, 1998; *Lumley et al.*, 1999). Reservoirs with average-porosity and consolidated rocks (e.g. *Moore*, 1997; *He et al.*, 1998; *Johnston et al.*, 1998) are suitable for time-lapse seismic monitoring, but difficulties may be encountered. Reservoirs with dead oil and water, or stiff or low-porosity rocks (e.g. *Johnstad et al.*, 1995; *Hirsche et al.*, 1997; *Wang et al.*, 1998; *Walls et al.*, 1998; *Talley et al.*, 1998) are thought to be less feasible for time-lapse seismic monitoring.

1.2.2 Factors to affect time-lapse seismic monitoring

The factors that directly affect time-lapse seismic monitoring include a feasibility study, acquisition design, seismic processing, and comprehensive interpretation. Each component will be briefly reviewed based on the published case studies. The details of its implementation will be described in the subsequent chapters with the presentation of a case study from the East Senlac area.

Feasibility

The feasibility study is usually conducted prior to carrying out time-lapse seismic monitoring. The commonly used technique in the oil industry is the technical spreadsheet developed by *Lumley et al.* (1997). This spreadsheet includes reservoir and seismic aspects. Some parameters, such as seismic velocity and density, can be predicted based on core sample measurement. The selected core samples should represent the typical *in situ* reservoir saturations, pressures, and temperatures (e.g. *Wang*, 1997; *Hirsche et al.*, 1997). The seismic velocity and density can also be obtained from other sources, such as from reservoir simulations (e.g. *Lumley et al.*, 1994). The predicted parameters can be used to generate forward seismic models. In addition to predicting the relevant parameters and generating forward seismic models, it is also important to consider how to design optimal acquisition system so that rock property induced seismic variations can be monitored in the field time lapse experiment.

Acquisition

Once a feasibility study has been completed and a decision has been made of approving a time-lapse seismic monitoring project, the next important task is to design and to acquire calendar seismic surveys. During the process of seismic data acquisition, to maintain repeatability between the calendar surveys is very important in the time-lapse seismic monitoring (e.g. *Moldoveanu et al.*, 1996; *Beasley et al.*, 1997; *Ebrom et al.*, 1997; *Rennie et al.*, 1997; *El-Emam et al.*, 1998; *Porter-Hirsche and Hirsche*, 1998; *Landro*, 1999a; *Aritman*, 2001). When the source/receiver coordinates and the recording geometries are completely the same, random noise is possibly the main factor to influence the repeatability between the calendar surveys (e.g. *Porter-Hirsche and Hirsche*, 1998). In general, repeatability can be

improved by burying detectors at greater depths (e.g. *Moldoveanu et al.*, 1996). A high degree of repeatability can also be achieved without permanently emplaced detectors or accurately re-located shot positions (e.g. *El-Emam et al.*, 1998). However, the repeatability decreases rapidly as the accuracy of the positioning of the repeated surveys decreases (e.g. *Landro*, 1999a). Especially, care should be taken that repeatability tends to decrease when the acquisition instrumentation, geometry and/or source characteristics are changed (e.g. *El-Emam et al.*, 1998). Sometimes, when different sources are used in the seismic survey acquisition, the method, such as the instantaneous phase correction (e.g. *Aritman*, 2001) can be employed to improve seismic repeatability.

In summary, the factors, such as geometry design, acquisition instrument, source / detector characters, even small variations in water table, tides, ambient noise conditions, to name a few, can have significant effect on the repeatability between the acquired seismic surveys. Some negative effects produced at the acquisition stage can be minimized by the improved performance and better field design. However, some effects, such as the near surface effects, are impossible to overcome at the acquisition stage, and they can only be solved or ameliorated at the subsequent processing stages.

Processing

In order to detect seismic variations within the reservoir area, high fidelity processing procedures should be employed. The selection of consistent parameters is suggested at the processing stage. Meanwhile, the data dependent processing procedures should be avoided since such procedures may produce unexpected noise or artifacts within the supposedly static geology environment (e.g. *Ross and Altan*, 1997). The data dependent processing is also called noise sensitive processing which may include deconvolution, refraction statics, surface consistent statics, and migration.

The cross-equalization (XEQ) is another important component in the time-lapse seismic processing. The main purpose of XEQ is to minimize residual reflector energy so that the calendar seismic surveys can be properly compared with each other (e.g. *Ross et al.*, 1996; *Altan*, 1997; *Eastwood et al.*, 1998; *Harris and Henry*, 1998; *Rickett and Lumley*, 1998, 2001; *Li et al.*, 2001; *Zhang and Schmitt*, 2002). In general, the four elements of geometry and timing corrections, energy balancing, bandwidth equalization and phase correction

can be included in XEQ (*Ross et al.*, 1996). In a practical implementation, a wavelet operator is usually estimated to shape and match the reflection data from one survey to another. Typically, an operator is estimated within the static zones above the reservoir that should not experience changes with time. The extracted operator is then applied so that the non-repeatability caused variations can be minimized. Ideally, the difference between the two data sets after XEQ should be zero everywhere within the supposedly static reflection area, and the only variations within zone of the interest should be related to the dynamic physical variations. This is the basic assumption inherent in the XEQ.

The matched filtering and the bandwidth-phase equalization method are the commonly used XEQ methods (*Rickett*, 1997; *Rickett and Lumley*, 2001). These methods themselves are supposed to simultaneously estimate a correction for static time shift, phase, and spectral differences between surveys (*Rickett and Lumley*, 2001). Usually, the survey that has a greater and higher bandwidth is chosen to match the survey that has a relatively narrower and lower bandwidth; attempting to increase the bandwidth of a survey can produce unexpected noise that is irrelevant to real physical variations within the dynamic reservoir area (*Rickett*, 1997; *Rickett and Lumley*, 2001). In practice, the selection of the XEQ method used is usually determined case by case. One factor to consider is that many of the existing seismic imaging procedures are developed with structural imaging, and not with data fidelity of fluid movement, repeatability, or high spatial resolution in mind.

Calibration and Interpretation

After time-lapse seismic surveys have been consistently processed and properly cross-equalized, calibration should be made prior to interpretation so that possible seismic variations can be reasonably tied to other existing types of data (e.g. *Ecker et al.*, 1999). These calibration data may include nearby well logs, core sample measurements, and relevant production history data (e.g. *Ecker et al.*, 1999). Once calibration is completed, seismic variations can be interpreted. These variations or anomalies may be produced by the factors, such as saturation variations in oil, water, or gas (e.g. *Anderson et al.*, 1997; *Sonneland et al.*, 1997; *He et al.*, 1998), dynamic variations in terms of temperature and pressure (*Lumley*, 1995; *Lumley et al.*, 1995; *Jenkins et al.*, 1997), geological structural varia-

tions due to geomechanical compaction (e.g. *Walls et al.*, 1998), or fracturing (e.g. *Johnston et al.*, 1998). Quantitative interpretation on the parameter such as saturation, temperature and pressure, (e.g. *Lumley et al.*, 1999; *Tura and Lumley*, 1998, 1999a,b; *Landro*, 1999b) can be further estimated.

In the process of interpretation, uncertainties sometimes can be taken into account (e.g. *Ecker et al.*, 1999; *Landro*, 2002). At present, there are very few public case studies discussing this issue. Strict data requirement is the main factor. For example, in the estimation of steam thickness and temperature variations (*Ecker et al.*, 1999) and in the estimation of saturation changes (or pressure changes) (*Landro*, 2002), uncertainties can be taken into account when the accurate rock property parameters are available.

Once interpretation and analysis are completed, recommendation can be made for the future reservoir management (e.g. *Waite and Sigit*, 1997).

Chapter 2

Time-lapse seismic impedance inversion by using the hybrid data transformation method

2.1 Introduction

During the production, the *in situ* conditions of stress, pore pressure, fluid saturation and temperature evolve; and these conditions directly influence the seismic velocities and bulk densities. It is these parameters linked through the impedance $I_{im} = \rho V$ that control the overall seismic response. If one is able to obtain via inversion of an observed seismic response this impedance; then one is able to better constrain what changes have occurred in the reservoir. In practice, it is usually assumed that the convolutional model described in many textbooks describes the formulation of a seismogram. As a result, one goal of current reflection seismic exploration is to obtain impedance information which changes as a function of depth or as a function of reflection travel time. The impedance expressed in a logarithmic format can be approximated as a function of reflectivity (e.g. *Peterson et al.*, 1955; *Sengbush et al.*, 1961; *Oldenburg et al.*, 1983) which can be directly inverted from reflection seismic data. In order to effectively estimate reflectivity from seismic data, several restrictions are usually imposed, some of which include the assumption of no multiples or no transmission losses. The accuracy of the estimated impedance is dependent on the magnitude of the inverted reflectivity. For example, if the reflectivity is within the range of [-0.3,+0.3], the error of estimated impedance is about 3% (*Oldenburg et al.*, 1983); if the reflectivity is within the range [-0.2,+0.2], the inverted impedance error

is less than 1.37% (*Hardage*, 1987; *Ghosh*, 2000).

In order to invert for reflectivity, a method such as sparse spike deconvolution can be employed. The precondition of this method is that the inverted reflectivity is sparse, and it contains only a limited number of randomly located, non-trivial reflection coefficient spikes. The commonly used spike deconvolution methods include single most likely replacement (SMLR) (*Kormylo and Mendel*, 1980), iterated conditional modes (ICM) (*Lavielle*, 1991), iterated window maximization (IWM)(*Kaaresen and Taxt*, 1998), simulated annealing (SA) (*Ingber*, 1989), and L1-based simplex algorithm (*Press et al.*, 1997). All these methods can be used to locate the correct reflectivity positions and the corresponding amplitudes for the resolvable structures. Resolvable here means that a given layer is sufficiently thick that the reflections from its top and bottom are sufficiently separate that they are clearly distinguished. Thin layers are not as easily detected as the top and bottom reflections image or "tune" together.

For the unresolvable structures, such as thin-beds and ramp structures, reflectivity can not be correctly inverted by the direct use of the above mentioned deconvolution methods. However, through careful observation on the thin bed structure, the reflected seismic wave shape is found to be identical to that of the 1^{st} derivative of the input source wavelet (e.g. *Widess*, 1973). For the ramp structure, the wave shape of the seismic response is identical to that of the integral of the input source wavelet at the boundary discontinuities and close to zero in between these discontinuities (e.g. *Hilterman*, 2001). Therefore, in order to correctly invert reflectivity for these two special structures, the seismic wave shape should be appropriately modified. To effectively deal with these special structures, a new method, called here, the hybrid data transformation will be proposed in this chapter. Similar algorithm with minor modification can be extended to the application of time-lapse seismic data.

In the process developed here, the input is the difference between the monitor seismic survey and the reference seismic survey. The inverted "reflectivity" is the reflectivity difference between these two surveys, and the estimated "impedance" is the impedance difference in a logarithmic format. Use of the seismic difference as input data can significantly reduce the number of non-zero reflections and also reduce the non-uniqueness of the inverted solutions (e.g. *Sarkar et al.*, 2003; *Gluck et al.*, 2000).

In the first part of this chapter, the mathematical formula of "reflectivity" will be derived in detail. The three type structures, thick block resolvable structure, thin-bed structure, and two ramps consisted triangle structure will be tested. In the second part, synthetic examples will be generated to demonstrate the effectiveness of this new proposed inversion algorithm.

2.2 The method to invert "reflectivity" and "impedance"

2.2.1 Motivation

There is some relevance of the derived seismic wave shape to the basic wavelet (e.g. *Sengbush et al.*, 1961; *Hilterman*, 2001). If the zero-phase Ricker wavelet which causes less distortion between interface is selected as the basic source wavelet, its 1^{st} derivative and its integral (Figure 2.1) correlate with responses from some physical structures (Figure 2.2). For example, at point "A", the structure is divided into two thick blocks which contain different velocities and constant densities. The reflected wave shape is identical to the basic wavelet for such isolated reflection. At "B", the structure consists of a thin bed with small velocity disturbance added. The seismic wave shape generated by thin bed is similar to the 1^{st} derivative of the source wavelet. "C" and "D" correspond to the top and bottom transition points of the thick ramp structure. The seismic wave shapes are identical to the shape of basic wavelet integral. Within the depth range from "C" to "D", the seismic response nearly vanishes due to the very small increases in reflectivity.

These observations are independent of the selected source wavelet. For example, similar effects (Figure 2.4) by using the minimum phase wavelet as basic wavelet shown in Figure 2.3 instead can be observed.

These relationships between particular velocity structures and the seismic wavelet tuning effects are very important in the estimation of reflectivity and impedance, especially for the special thin bed and ramp structures. For the thick block structure, reflectivity can be correctly inverted by the direct use of the spike deconvolution method. From the inverted reflectivity, the logarithmic impedance can be further estimated. However, for the thin bed and ramp structures, the above mentioned deoconvolution method can not be directly employed to invert for reflectivity. A new method, the hybrid data

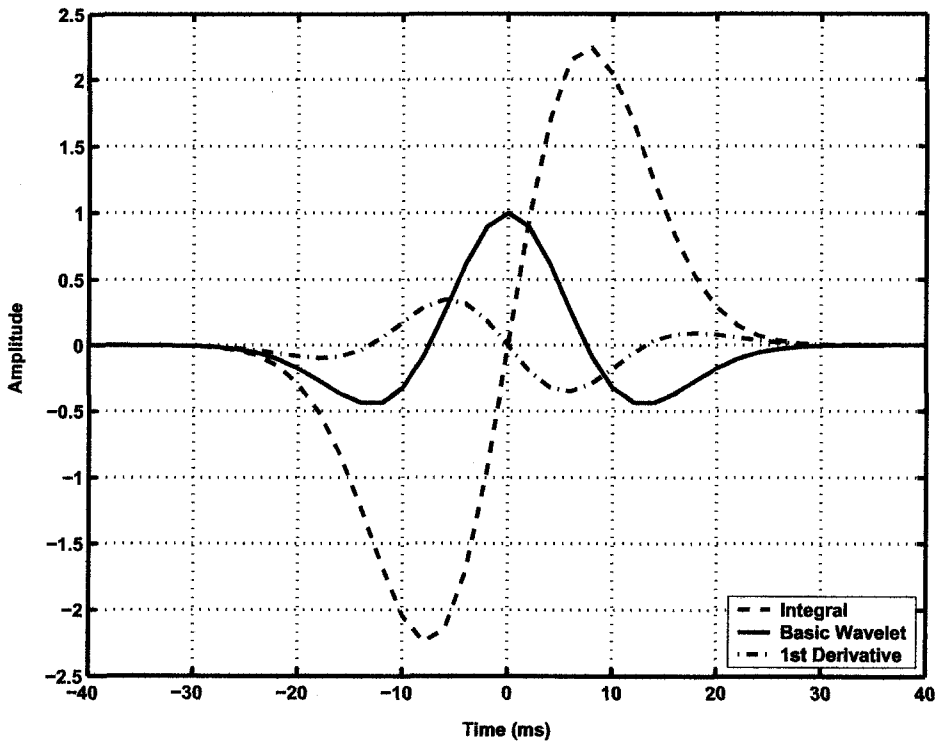

Figure 2.1: The basic Ricker wavelet, its derivative and its integral.

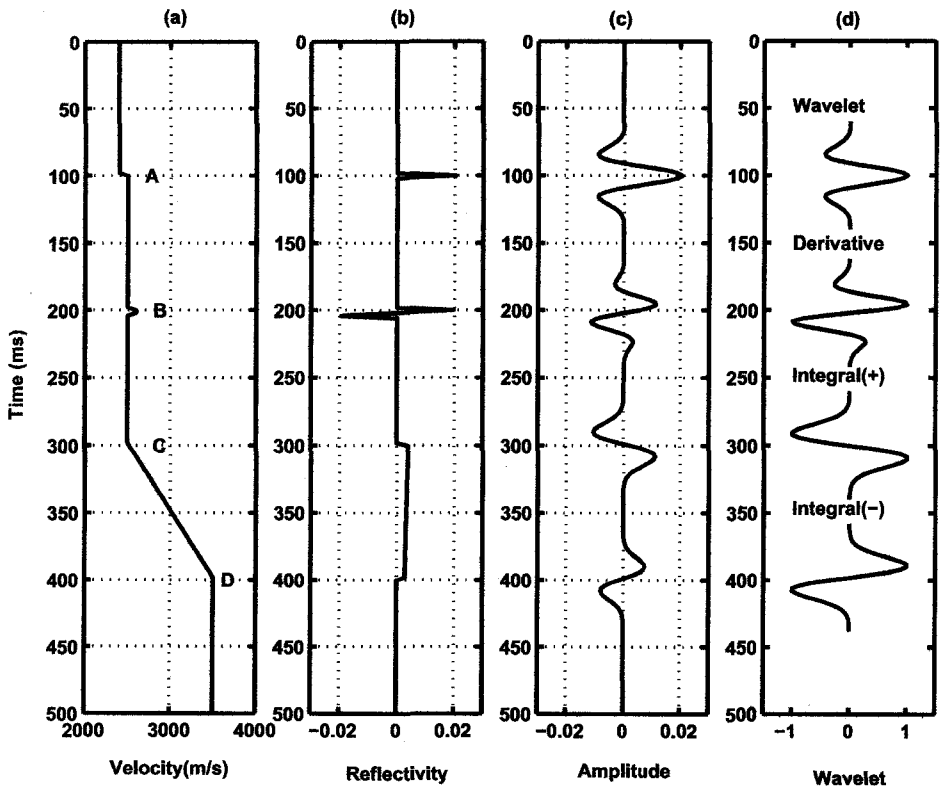

Figure 2.2: Comparison of the seismic response and the different wave shapes derived from the input Ricker wavelet. (a) Velocity model; (b) Reflectivity; (c) Synthetic seismic response; (d) Ricker wavelet and its derived wave shapes.

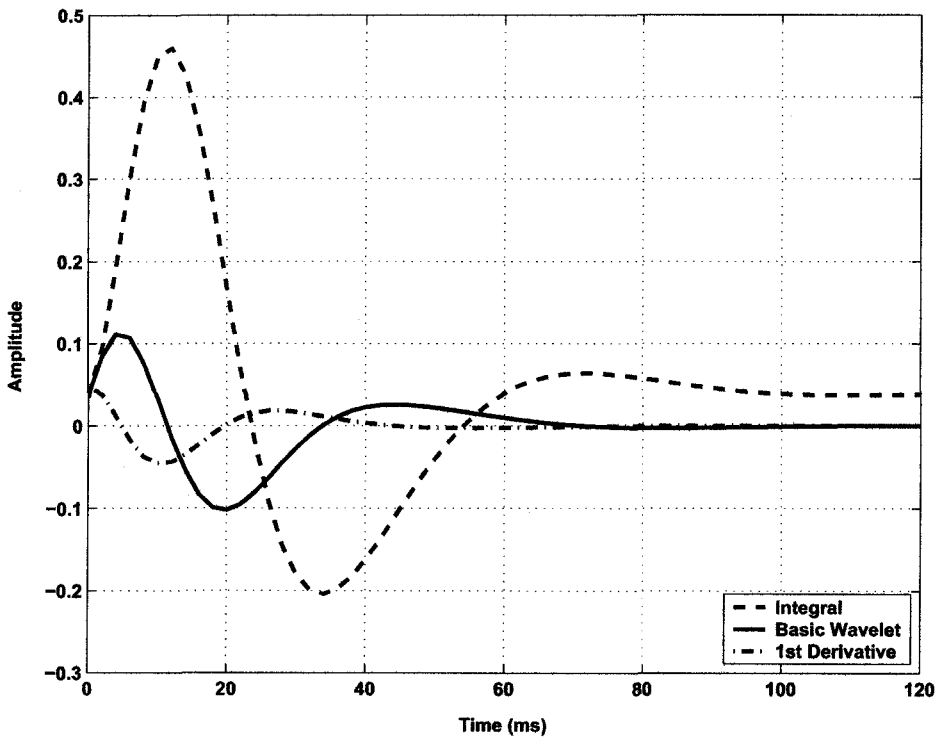

Figure 2.3: The basic minimum phase wavelet, its derivative and its integral.

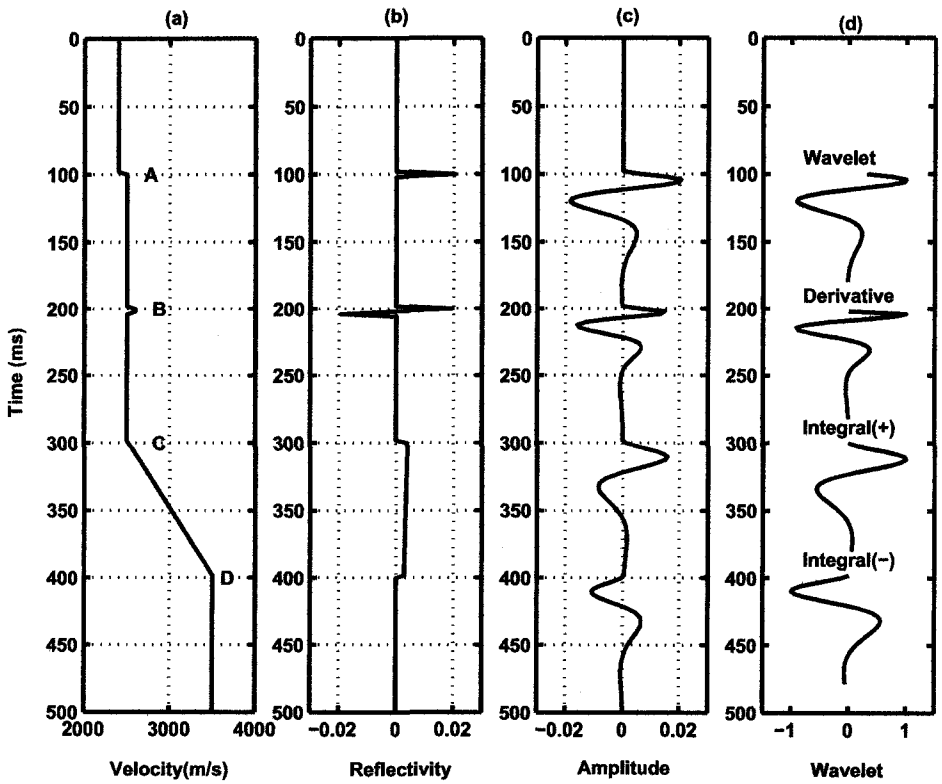

Figure 2.4: Comparison of seismic response and the different wave shapes derived from the input minimum phase wavelet. (a) Velocity model; (b) Reflectivity; (c) Synthetic seismic response; (d) Minimum phase wavelet and its derived wave shapes.

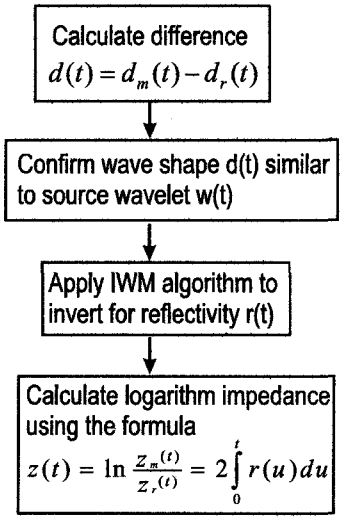

Figure 2.5: The "reflectivity" and "impedance" inversion flow for the thick block structure.

transformation, is proposed here to deal with these special structures. This process is not automatic; some priori knowledge of what changes anticipated in a given situation is required so that the correct inversion procedure is employed. For example, injection of steam to the reservoir could produce a "thin" low velocity layer that will change the overall seismic reflectivity. If one has some knowledge that this is the type of change to be introduced then one can adapt the inversion strategy appropriately. In this thesis, the technique could be considered more as an interpretive inversion by the anticipated change of the velocity and density structure.

Since the same features can be observed from the time-lapse seismic difference data, the new proposed inversion algorithm can be extended to the time-lapse mode seismic data. This is the main goal of this chapter. The time-lapse mode seismic inversion flow charts for the thick block, thin bed, and ramp structure are shown in Figure 2.5, 2.6 and 2.7 respectively. The details of derivation are shown in the following sections.

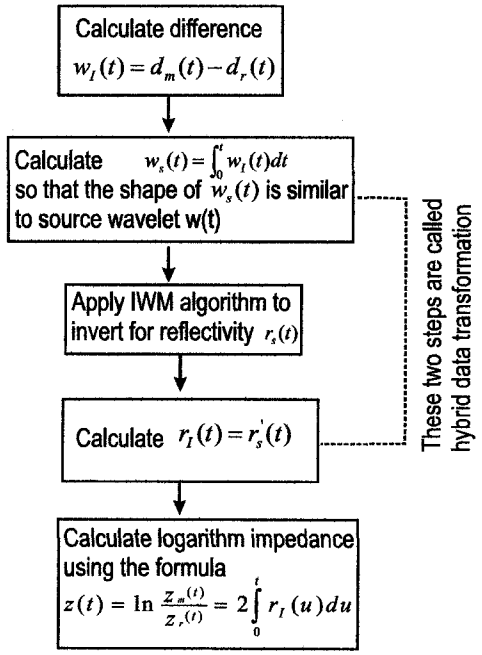

Figure 2.6: The "reflectivity" and "impedance" inversion flow for the thin bed structure.

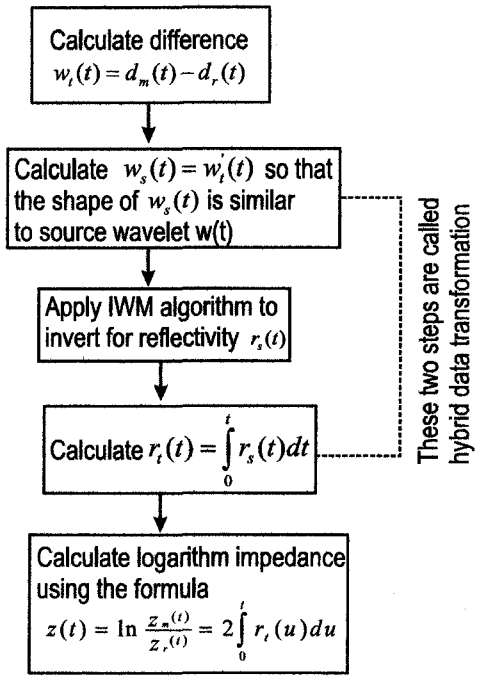

Figure 2.7: The "reflectivity" and "impedance" inversion flow for the ramp structure.

2.2.2 The relationship between "reflectivity" and "impedance" and the relevant properties of the Laplace transform

Here, the "reflectivity" is defined as the reflectivity difference between reference survey and monitor survey, and the "impedance" is defined as the impedance difference between reference survey and monitor survey in a logarithmic format. The relationship between "reflectivity" and "impedance" will be derived by using the Laplace transform.

Let $r_r(t)$ and $r_m(t)$ represent the zero-offset reflectivities for the reference and the later monitor traces, respectively. They are defined as (e.g. *Lay and Wallace*, 1995),

$$r_r(t) = \frac{z_r(t) - z_r(t-1)}{z_r(t) + z_r(t-1)} \tag{2.1}$$

$$r_m(t) = \frac{z_m(t) - z_m(t-1)}{z_m(t) + z_m(t-1)} \tag{2.2}$$

It must be remembered that "t" here represents the time within the seismic trace; this should not be confused with the calendar time. Here $z_r(t)$ and $z_m(t)$ represent impedance for the reference trace and monitor trace. Assume that variations in $z_r(t)$ and $z_m(t)$ are small, then the above two formulas can be approximated as,

$$r_r(t) \approx \frac{\triangle z_r(t)}{2z_r(t)} \approx \frac{1}{2}\frac{d(lnz_r(t))}{dt} \tag{2.3}$$

$$r_m(t) \approx \frac{\triangle z_m(t)}{2z_m(t)} \approx \frac{1}{2}\frac{d(lnz_m(t))}{dt} \tag{2.4}$$

The above formulas are valid when the absolute reflectivity is less than 0.3 (e.g. *Oldenburg et al.*, 1983).

Define the time-lapse mode "reflectivity" as,

$$r(t) = r_m(t) - r_r(t) = \frac{1}{2}\frac{d}{dt}(ln(z_m(t)/z_r(t))) \tag{2.5}$$

and the time-lapse mode impedance as $z(t) = \frac{1}{2}ln(z_m(t)/z_r(t))$. Then the above formula can be written as time derivative,

$$r(t) = z^{'}(t) \tag{2.6}$$

Since the convolution model can be written as,

$$d(t) = w(t) * r(t) \tag{2.7}$$

where $w(t)$ is the source wavelet, and $d(t)$ is the simple difference between the reference and monitor traces. Substituting the formula 2.6 into the formula 2.7, we obtain,

$$w(t) * z^{'}(t) = d(t) \tag{2.8}$$

Consequently, if reflectivity change can be correctly deconvolved using equation 2.7, then the time lapse impedance $z(t)$ can be estimated by:

$$z(t) = \int_0^t r(t)dt \tag{2.9}$$

Since $z(t)$ may be approximated as $z(t) = \frac{1}{2}ln(z_m(t)/z_r(t))$, then $z(t)$ estimated from formula 2.9 can be interpreted as the half impedance ratio between the monitor trace and the reference trace in a logarithmic format. Various cases may be considered.

a) If $z(t) > 0$, then the impedance increases from the reference trace to the monitor trace;

b) If $z(t) = 0$, then there is no change in impedance;

c) If $z(t) < 0$, the impedance decreases from the reference trace to the monitor trace.

Therefore, the estimated $z(t)$ can be used to indicate the variation in impedance from the reference trace to the monitor trace.

At this point, it is useful to introduce another velocity structure, here called the triangle structure, which consists of two gradients. This could be a reasonable approximation to the impedance within a reservoir in which fluids are removed from the centre leaving gradients in pore pressure and saturation, for example, from the centre to both the top and bottom. For the three time-lapse mode structures including the unit step structure, the unit impulse structure, and the triangle structure, the function *z(t)* can be expressed in a simple format as shown in Table 2.1 (e.g. *Sengbush et al.*, 1961). For the normalized function, the thick block structure is near the abrupt transition points equivalent to the unit step structure; the thin bed structure can be approximated by the unit impulse structure, and the ramp structure can be considered as a triangle structure.

Table 2.1: Functions for the time-lapse mode structures.

Unit step	$z(t) = u(t)$
Unit impulse	$z(t) = \delta(t)$
Triangle	$z(t) = c_0 tu(t) + c_1(t - \Delta t_1)u(t - \Delta t_1) + c_2(t - \Delta t_2)u(t - \Delta t_2)$

Table 2.2: Laplace transform properties.

	Time Domain	Complex Domain
(a)	Integration	division by s
	$\int f(t)dt$	$F(s)/s$
(b)	Differentiation	multiplication by s
	$df(t)/dt$	$sF(s)$
(c)	Time shift by a unit	multiplication by e^{-as}
	$f(t-a)$	$e^{-as}F(s)$
(d)	Convolution	multiplication of transforms
	$\int f_1(\tau)f_2(t-\tau)d\tau$	$F_1(s)F_2(s)$

Here $u(t)$ is a unit function which can be expressed as,

$$u(t) = \begin{cases} 1 & t \geq 0; \\ 0 & t < 0. \end{cases} \tag{2.10}$$

The $\delta(t)$ is a unit impulse function which can be written as,

$$\delta(t) = \begin{cases} \lim_{\epsilon \to 0} \frac{1}{\epsilon} & -\frac{\epsilon}{2} \leq t \leq \frac{\epsilon}{2}; \\ 0 & \text{otherwise.} \end{cases} \tag{2.11}$$

The relevant properties of Laplace transform which will be used in the subsequent derivation of "reflectivity" are listed in Table 2.2.

2.2.3 Unit step (thick layer) structure

The Laplace transform of the convolution model of 2.7 in the complex domain can be written as,

$$D(s) = W(s)R(s) \tag{2.12}$$

To differentiate, apply the property (b) listed in Table 2.2 to the equation 2.6 and transform it in the complex domain, it can be written as:

$$R(s) = sZ(s) \tag{2.13}$$

Substituting formula 2.13 into formula 2.12, we obtain,

$$D(s) = sW(s)Z(s) \tag{2.14}$$

Since for the unit step structure, the "impedance" function can be transformed to the complex domain by using Laplace transform,

$$Z(s) = \int_0^\infty u(t)e^{-st}dt = \frac{1}{s} \tag{2.15}$$

Substitute formula 2.15 into formula 2.14, the formula 2.14 becomes,

$$D(s) = W(s) \tag{2.16}$$

Transform the above formula into time domain, it becomes,

$$d(t) = w(t) \tag{2.17}$$

Therefore, the convolutional model 2.8 for the unit step structure becomes,

$$w(t) = w(t) * u^{'}(t) \tag{2.18}$$

Therefore, if the source wavelet $w(t)$ and the "reflectivity" $r(t)$ ($u^{'}(t)$) are known, the seismic response can be generated and it has the identical wave shape as the source wavelet. Conversely, if the source wavelet $w(t)$ is known, the "reflectivity" which has a single spike can be precisely inverted. This is the inverse problem. The procedure to invert "reflectivity" and "impedance" for the thick block structure is shown in Figure 2.5.

2.2.4 Unit impulse (thin bed) structure

It is known from Table 2.1 that the unit impulse "impedance" function is defined as,

$$z(t) = \delta(t) \tag{2.19}$$

The corresponding Laplace transform in complex domain is,

$$Z(s) = \int_0^\infty \delta(t) e^{-st} dt \tag{2.20}$$

Since an impulse function $\delta(t)$ has the property,

$$\int_{t_1}^{t_2} f(t)\delta(t - t_0)dt = f(t_0), \qquad t_1 \leq t_0 \leq t_2 \tag{2.21}$$

Therefore, the formula 2.20 becomes

$$Z(s) = \left[e^{-st}\right]_{t=0} = 1 \tag{2.22}$$

The convolution model 2.14 in complex domain can be written as,

$$D(s) = sW(s) \tag{2.23}$$

Apply differentiation property (b) listed in Table 2.2 to the above formula and transform it into time domain, we get,

$$d(t) = w^{'}(t) \tag{2.24}$$

Substitute the formula 2.24 and the formula 2.19 into the formula 2.8, the convolution model for the unit impulse structure can be written as,

$$w^{'}(t) = w(t) * \delta^{'}(t) \tag{2.25}$$

Since the unit function $u(t)$ and the impulse function $\delta(t)$ have the relationship $\delta(t) = u^{'}(t)$, conduct derivative on the both sides, we have $\delta^{'}(t) = u^{''}(t)$. Therefore, the above formula 2.25 can be rewritten as,

$$w(t) * u^{''}(t) = w^{'}(t) \tag{2.26}$$

Compare with the unit step convolution model which is $w(t) * u^{'}(t) = w(t)$. Based on the previous derivation, for the unit step structure, let $r_s(t)$ and $w_s(t)$ represent "reflectivity" and seismic difference response. They can be expressed as,

$$r_s(t) = u^{'}(t) \tag{2.27}$$

$$w_s(t) = w(t) \tag{2.28}$$

For the unit impulse structure, let $r_I(t)$ and $w_I(t)$ represent "reflectivity" and seismic difference response. Based on formula 2.26, they can be written as,

$$r_I(t) = u^{''}(t) \tag{2.29}$$

$$w_I(t) = w^{'}(t) \tag{2.30}$$

Obviously, the "reflectivity" and the seismic difference response have the established communication between the unit step structure and the unit impulse structure,

$$r_I(t) = r_s^{'}(t) \tag{2.31}$$

$$w_I(t) = w_s^{'}(t) \tag{2.32}$$

Therefore, for the impulse type structure, the "reflectivity" $r_I(t)$ can be indirectly inverted by firstly integrating the seismic difference to invert for $r_s(t)$ for the unit step structure, then perform derivative to $r_s(t)$ to obtain $r_I(t)$ for the impulse type structure. The process to invert "reflectivity" and "impedance" is shown in Figure 2.6. The procedure to modify the seismic difference response and "reflectivity" is called the hybrid data transformation.

2.2.5 Triangle structure

A ramp structure is usually defined as a linear increase or decrease in "impedance", a definition modified after *Sengbush et al.* (1961) who used the "velocity" instead of the "impedance" as a variable. The double ramps constitute a triangle structure.

For the triangle structure, the "impedance" function listed in Table 2.1 can be written as,

$$z(t) = c_0 t u(t) + c_1(t - \Delta t_1)u(t - \Delta t_1) + c_2(t - \Delta t_2)u(t - \Delta t_2), \quad 0 \le \Delta t_1 \le \Delta t_2 \le t \tag{2.33}$$

It can also be written as an integral format,

$$z(t) = c_0 \int_0^t u(t)dt + c_1 \int_0^t u(t - \Delta t_1)dt + c_2 \int_0^t u(t - \Delta t_2)dt \tag{2.34}$$

The above formula can also be written as,

$$z(t) = \sum_{i=0}^{i=2} c_i \int_0^t u(t - \Delta t_i)dt \tag{2.35}$$

where it is assumed $\Delta t_0 = 0$. Apply integral property (a) and time shift property (c) listed in Table 2.2 to the formula 2.35, the transformed "impedance" in the complex domain is,

$$Z(s) = \frac{1}{s}U(s)\sum_{i=0}^{i=2} c_i e^{-\Delta t_i s} \tag{2.36}$$

From the previous derivation, it is known that for the unit step structure, if the assumed "impedance" is $u(t)$, the corresponding Laplace transform in complex domain is $U(s) = \frac{1}{s}$. Substitute this formula into the above formula, we get,

$$Z(s) = \frac{1}{s^2}\sum_{i=0}^{i=2} c_i e^{-\Delta t_i s} \tag{2.37}$$

Therefore, for the triangle structure, substitute the above formula into the convolution model 2.14, we get,

$$D(s) = \frac{1}{s}W(s)\sum_{i=0}^{i=2} c_i e^{-\Delta t_i s} \tag{2.38}$$

Transform the above formula to the time domain, we get,

$$d(t) = \sum_{i=0}^{i=2} c_i \int_0^t w(t - \Delta t_i)dt \tag{2.39}$$

Now directly substitute $z(t)$ shown in 2.35 into the formula 2.8, we get,

$$d(t) = w(t) * (\sum_{i=0}^{i=2} c_i \int_0^t u(t - \Delta t_i)dt)' \tag{2.40}$$

The above formula can be simplified as,

$$d(t) = w(t) * \sum_{i=0}^{i=2} c_i u(t - \Delta t_i) \tag{2.41}$$

Compare the formula 2.39 with the formula 2.41, we get,

$$w(t) * \sum_{i=0}^{i=2} c_i u(t - \Delta t_i) = \sum_{i=0}^{i=2} c_i \int_0^t w(t - \Delta t_i)dt \tag{2.42}$$

If the transition discontinuities are within seismic resolution, for the i^{th} component, the following formula is valid,

$$w(t) * u(t - \Delta t_i) = \int_0^t w(t - \Delta t_i)dt \tag{2.43}$$

Let $r_t(t)$ and $w_t(t)$ represent the "reflectivity" and the seismic difference response for the triangle structure. They can be written as,

$$r_t(t) = u(t - \Delta t_i) \tag{2.44}$$

$$w_t(t) = \int_0^t w(t - \Delta t_i)dt \tag{2.45}$$

From the previous analysis, it is known that for the unit step structure, the "reflectivity" and the seismic difference response have the form, $r_s(t) = u^{'}(t)$ and $w_s(t) = w(t)$.

Obviously, the "reflectivity" and the seismic difference response between the unit step structure and the triangle structure is communicated via the following formula,

$$r_s(t) = r_t^{'}(t) \tag{2.46}$$

$$w_s(t) = w_t^{'}(t) \tag{2.47}$$

Therefore, for the triangle structure, "reflectivity" can be correctly inverted by choosing the appropriate data transformation procedure shown in Figure 2.7.

2.3 Numerical Examples

In this part, numerical examples will be given to illustrate the determination of the inverted time-lapse mode "impedance" by selecting the appropriate inversion procedure. In the first example, the structure is a thick block. For this type structure, "reflectivity" can be inverted by directly using the spike deconvolution algorithm. The "impedance" can be further estimated. In the second example, the model is a thin bed structure which can be approximated as an impulse structure. In the third example, the model is a triangle structure. It consists of double ramps. For these two latter structures, the seismic wave shapes should be modified first so that the spike deconvolution can be employed. In the

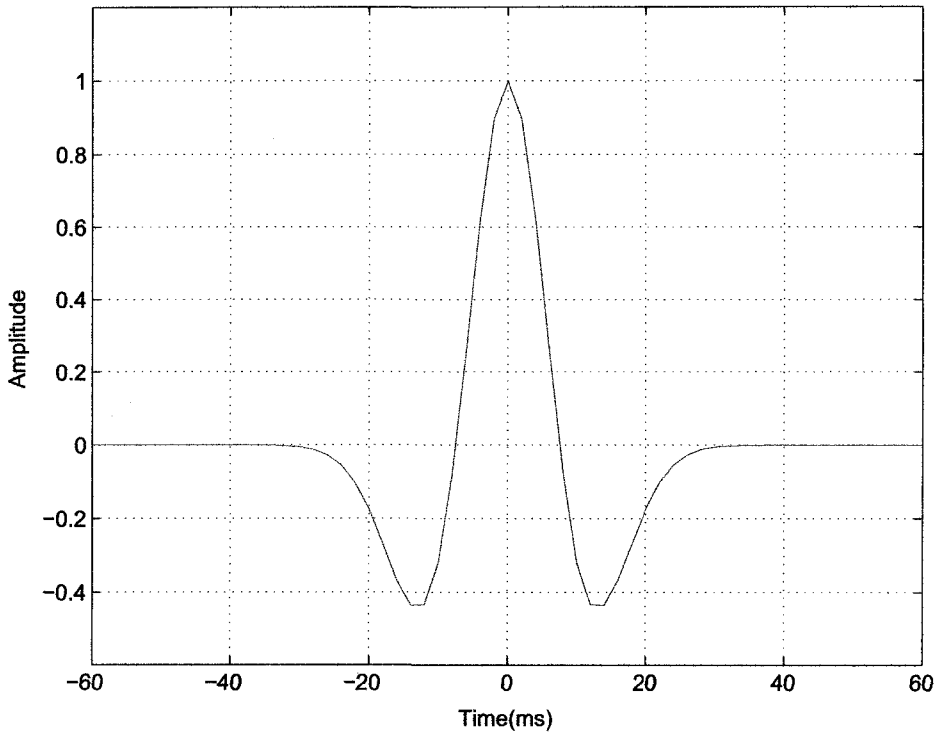

Figure 2.8: The Ricker source wavelet with main frequency 30 Hz.

simulation of time-lapse mode seismic scenario, the calendar impedance variations are assumed to take place only within the pseudo reservoir area. The selected Ricker source wavelet is shown in Figure 2.8. The main frequency is 30 Hz. The synthetic seismic sample rate is 2 ms and there are total 104 samples in the synthetic seismic response.

2.3.1 Thick block structure

The first synthetic example simulates a thick block reservoir within which acoustic impedance variations are assumed to occur. The reference trace is shown in Figure 2.9. The monitor trace is shown in Figure 2.10 with the +15% impedance disturbance added within the range of the two discontinuities. The resultant "reflectivity" values at these boundary discontinuities are 0.075 and -0.075.

The inverted "reflectivity" and "impedance" are shown in Figure 2.11. Since the thick-

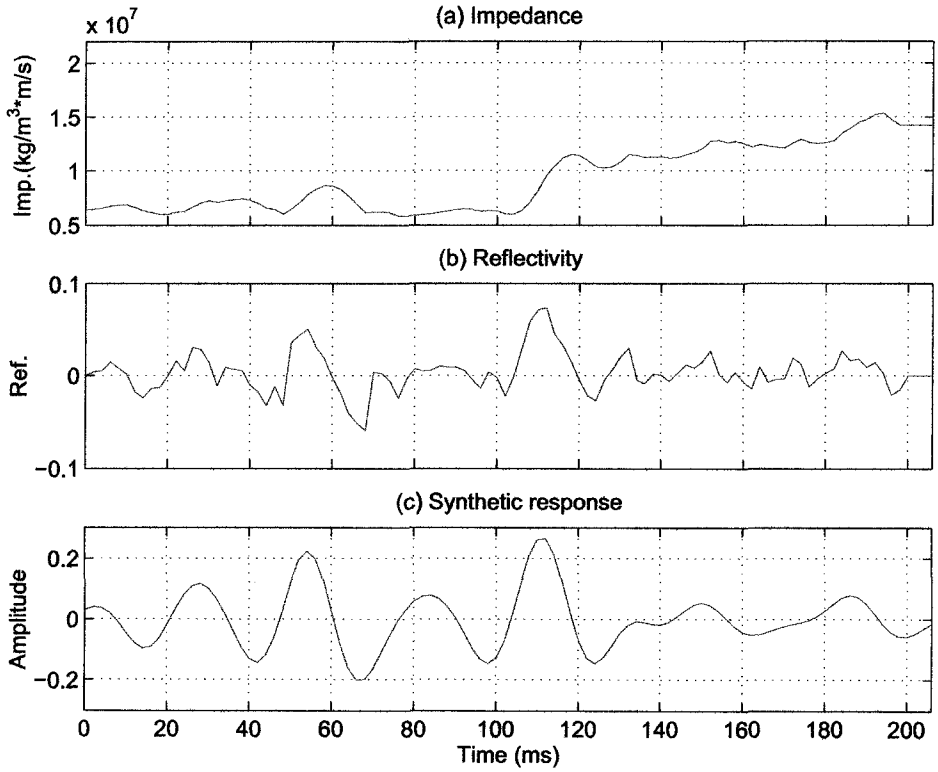

Figure 2.9: The synthetic reference trace.

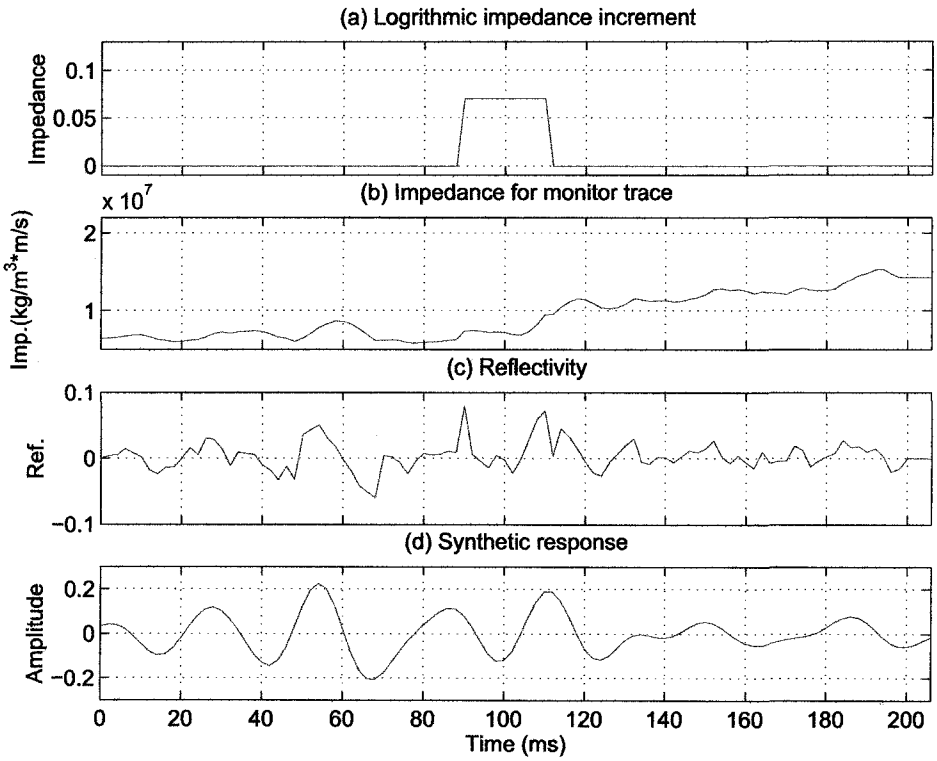

Figure 2.10: Impedance variation and the synthetic monitor trace.

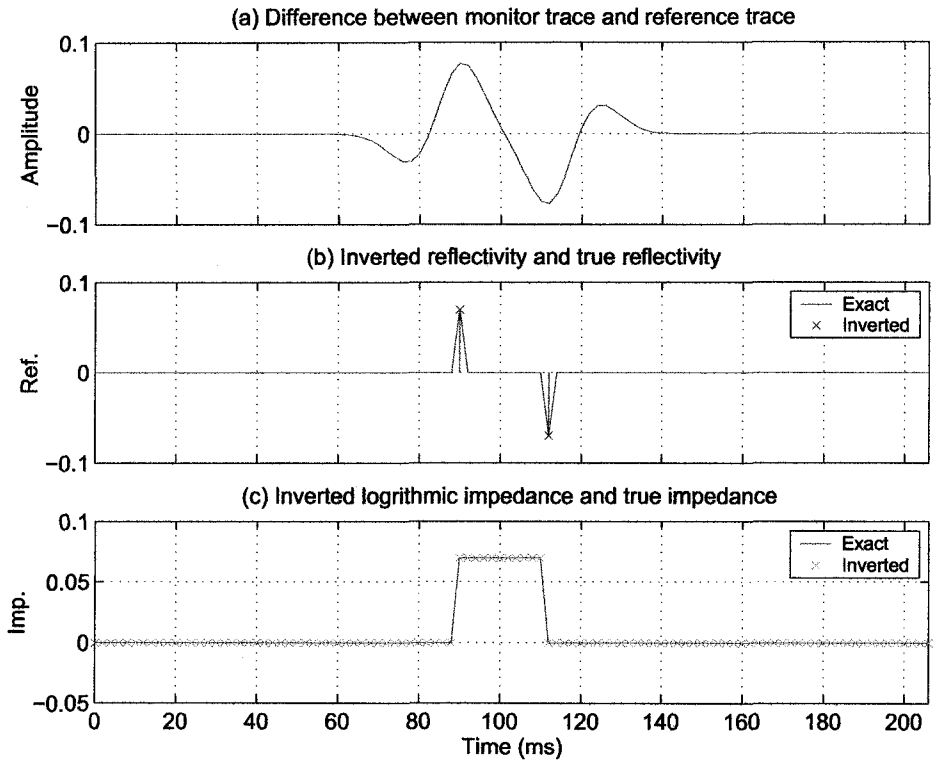

Figure 2.11: Inverted thick block "reflectivity" and "impedance" by the direct application of spike deconvolution algorithm.

ness of this structure is such that it can be well resolved, the "reflectivity" positions and their values can be correctly inverted by directly using the spike deconvolution algorithm. The details of the employed spike deconvolution method are described in Appendix B.

When 20% random Gaussian noise is added to the synthetic response, the inverted "reflectivity" and the inverted "impedance" shown in Figure 2.12 still possess very high quality. These results are expected as these are the conditions under which the sparse spike deconvolution method was designed.

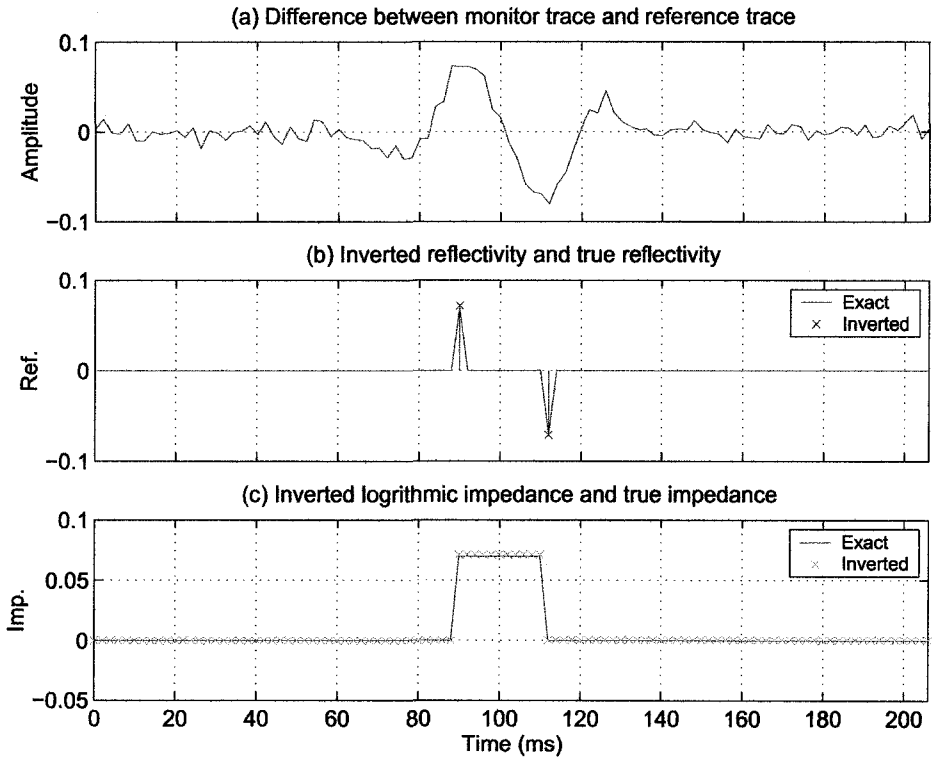

Figure 2.12: Inverted thick block "reflectivity" and "impedance" with 20% Gaussian noise added.

2.3.2 Thin bed structure

The thin bed structure can be approximated by the impulse function. Three synthetic examples will be shown here. The reference traces in all three examples are the same as used above and as shown in Figure 2.9. In the first 1-D example, the thin bed thickness is about 1/16 wavelength. In the second example, the thin bed thickness is about 1/8 wavelength. The third example is a 2-D thin bed structure which is based on the East Senlac SAGD model generated. The thickness for these three models are below seismic resolution limit, but the tuning effect will still produce a detectable response. We delay discussion of this aspect of seismic monitoring of thin beds till later.

For the first thin bed structure with about 1/16 wavelength thickness, the impedance variations and the generated synthetic response for the monitor trace are shown in Figure 2.13. For comparison, the "reflectivity" and "impedance" are firstly inverted by directly using the existing sparse spike deconvolution method. The results inverted from Figure 2.14(a) are shown in Figure 2.14(b) and (c). Obviously, the "reflectivity" and "impedance" are not correctly recovered. This is because these "reflectivity" positions are too close to be resolved individually. The distance between the inverted spikes is wider than the true distance. However, when using the recently proposed hybrid inversion procedure, the "reflectivity" and the "impedance" are precisely inverted. The inverted results are shown in Figure 2.15(b) and (c).

Similar results are obtained when the thin bed thickness increases to about 1/8 wavelength. The relevant monitor trace information is shown in Figure 2.16. The Figure 2.17 shows the inverted "reflectivity" and the inverted "impedance" by the direct application of spike deconvolution method. The Figure 2.18 shows the inverted results by the application of the hybrid data transformation procedure.

From these two synthetic examples, the hybrid inversion scheme has been proved effective for the thin bed structures.

The third example is a 2-D thin bed structure consisting of variations in the impedance within the thin layer. This thin bed could simulate the response expected out perpendicular from a central horizontal injection well. The forward seismic modelling is generated by using the 2-D finite difference method. The common mid point (CMP) stack fold is

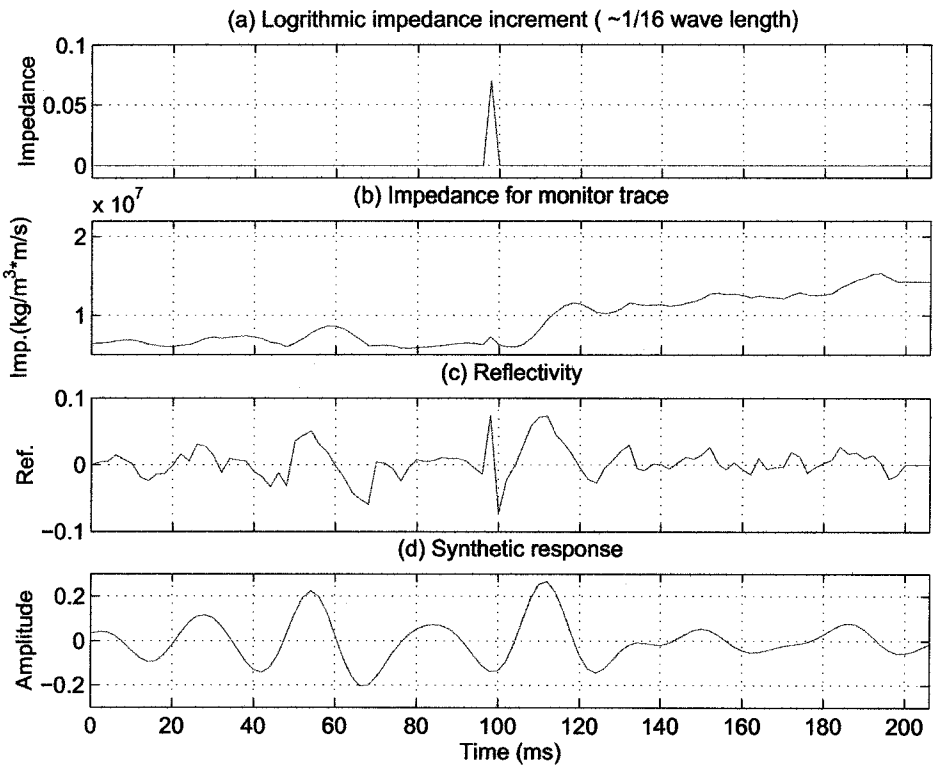

Figure 2.13: Synthetic monitor trace with 15% impedance increment. The thin bed thickness is about 1/16 wave length.

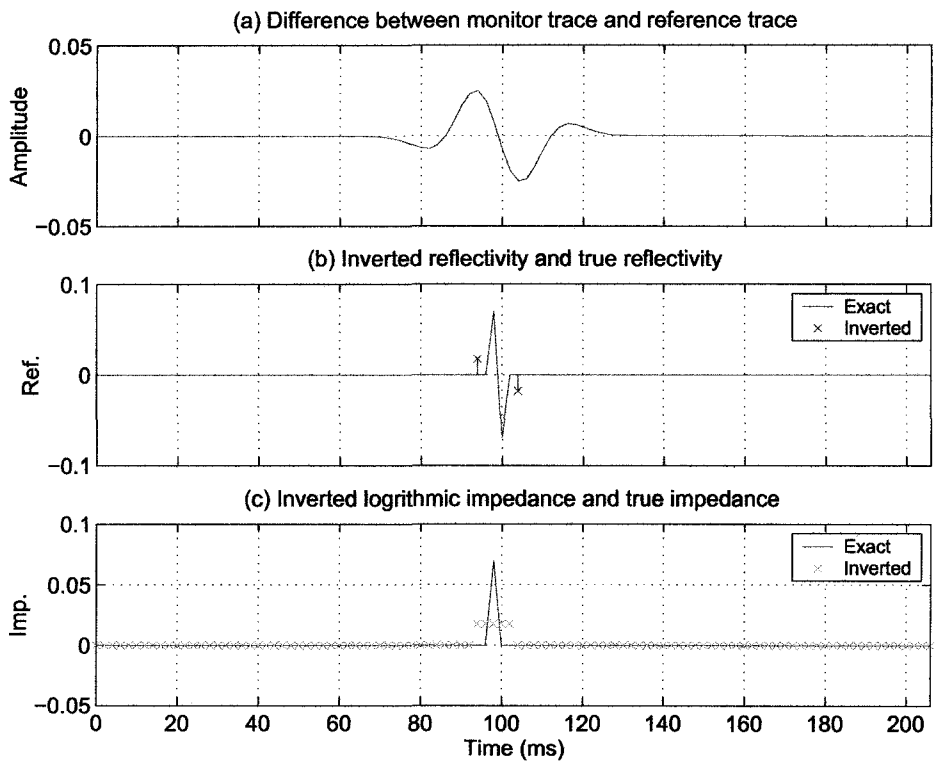

Figure 2.14: Inverted "reflectivity" and "impedance" by the direct application of spike deconvolution method.

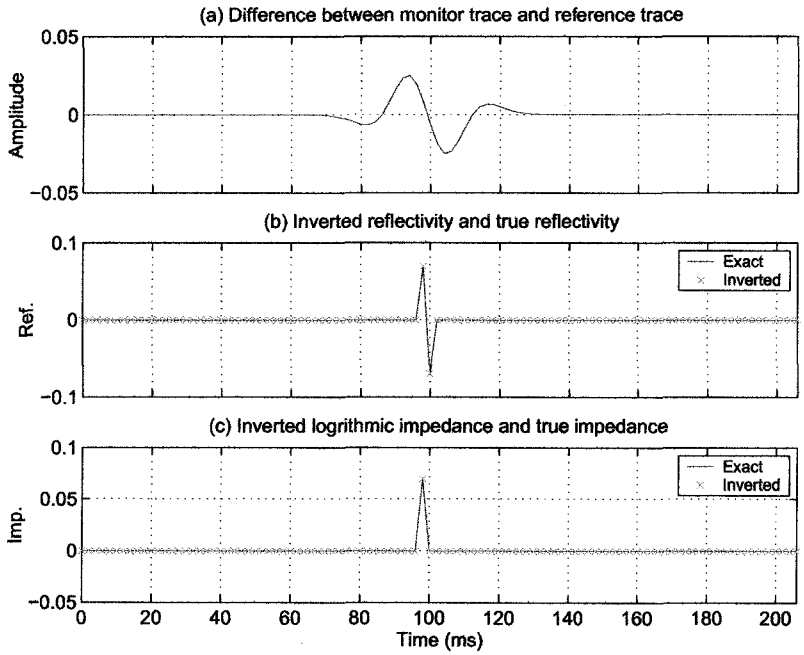

Figure 2.15: Inverted "reflectivity" and "impedance" by the application of the hybrid data transformation procedure.

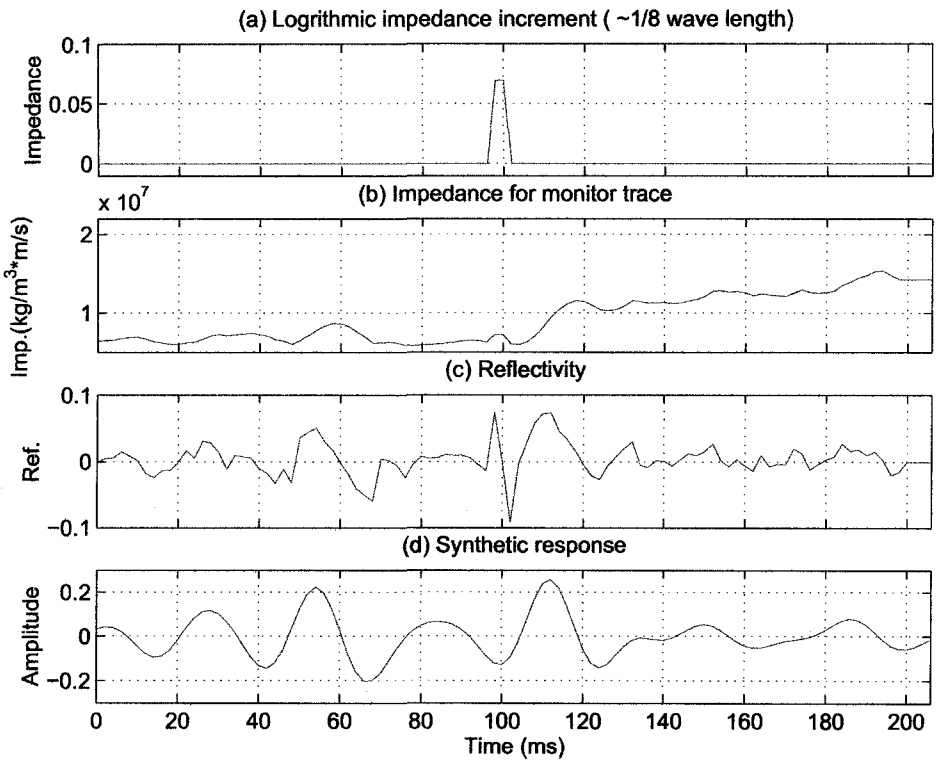

Figure 2.16: Monitor trace with 15% impedance increment. The thin bed thickness is about 1/8 wave length.

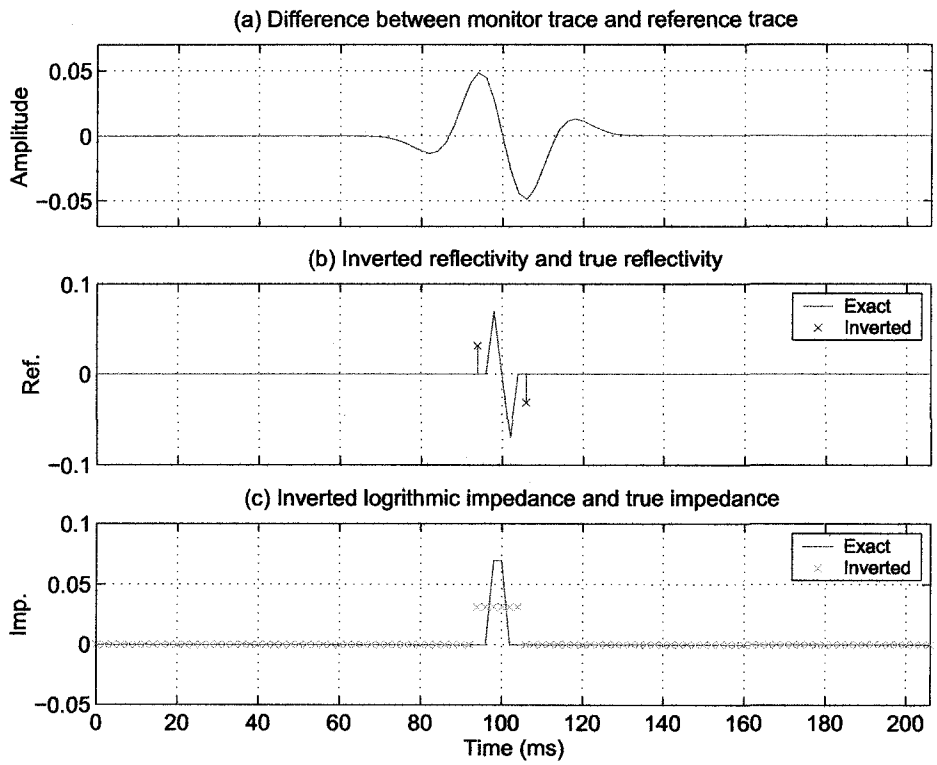

Figure 2.17: Inverted "reflectivity" and "impedance" by the direct application of spike deconvolution method.

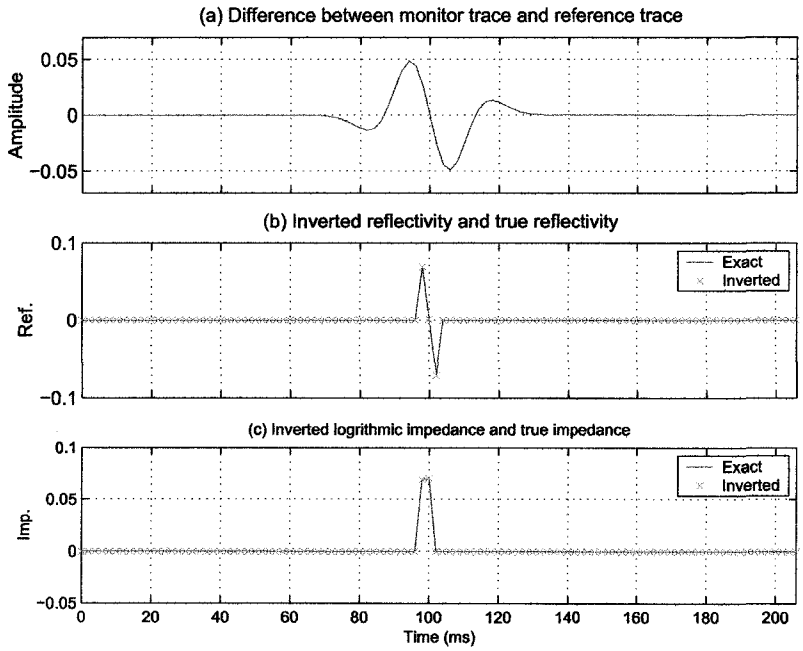

Figure 2.18: Inverted "reflectivity" and "impedance" by the application of the hybrid data transformation procedure.

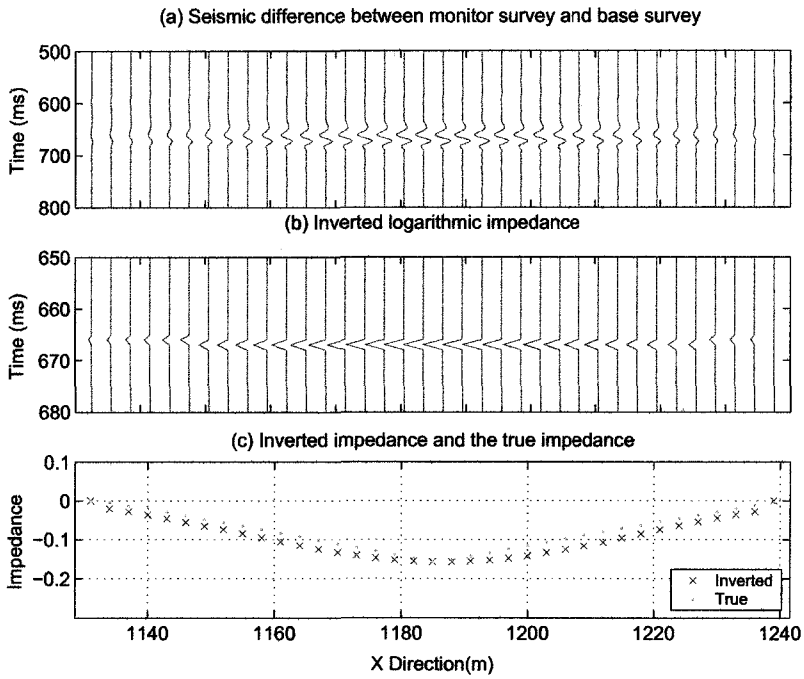

Figure 2.19: The 2-D thin bed seismic difference, inverted "impedance", and the comparison between the inverted and the true "impedance".

distributed in a triangle shape. The geometry design is the same as the field data design in East Senlac area. The specific structure consists of a 12m thick layer with a maximum 15% decrease in impedance at the centre (x=1185m) which vanishes at $x = 1135$m and $x = 1235$m. The generated seismic difference is shown in Figure 2.19(a). The inverted "impedance" is shown in Figure 2.19(b). The inverted and the true "impedance" are plotted together shown in Figure 2.19(c). The inverted "impedance" is very close to the true "impedance". The observed deviations are mainly due to the normal move out (NMO) stretch effect during the post-stack seismic data processing. This 2-D thin bed example has further demonstrated the effectiveness of this new inversion algorithm.

2.3.3 Triangle structure

This triangle structure consists of two intersecting ramps (Figure 2.20). The "impedance" on one side ramp increases linearly until it reaches 15%. Then it begins to decrease lin-

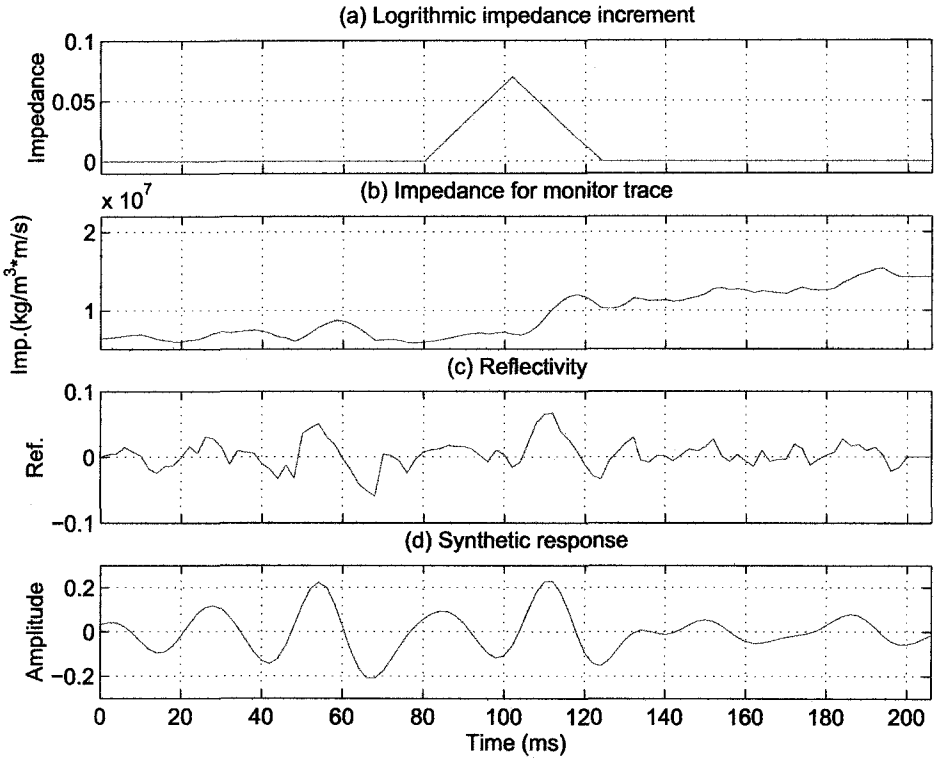

Figure 2.20: The monitor trace for the triangle structure.

early on the other side ramp until the increment is zero. The pseudo triangle time-lapse mode structure might be expected in a case where injected fluids gradually intrude the reservoir from a central point of injection - particularly along horizontal well bores. The hypothetical variations in impedance and in the generated synthetic monitor trace are shown in Figure 2.20. The reference trace is the same as in the thick block structure case.

First, the "reflectivity" and the "impedance" are inverted by the direct application of sparse spike deconvolution. The results inverted from Figure 2.21(a) are shown in Figure 2.21(b) and (c). Clearly, the inverted "reflectivity" positions and the values are incorrect. As in the other examples, the sparse spike method appears to average the impedances over the zone of interest.

As a comparison, the hybrid data transformation procedure is employed to invert "reflectivity" and "impedance". The inverted results are shown in Figure 2.22(b) and (c).

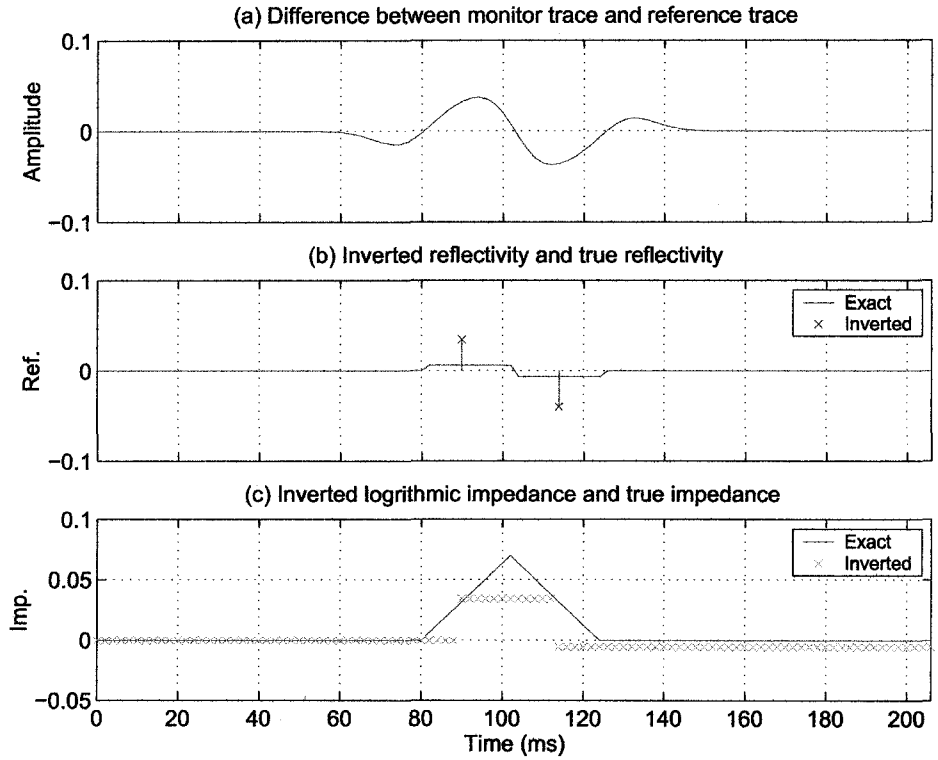

Figure 2.21: Inverted "reflectivity" and "impedance" by the direct application of the spike deconvolution method.

The "reflectivity" and "impedance" are all accurately recovered for this case.

2.4 Summary and conclusions

When the subsurface "reflectivity" is sparse and spiky, the spike deconvolution method can be directly employed to invert for the "reflectivity", from which to further estimate "impedance". However, for the thin bed and triangle time-lapse mode structures, the sparse spike deconvolution fails to correctly locate the "reflectivity" because these structures consist of subresolution gradient ramps or thin layers. Sparse spike deconvolution was not designed to handle such cases. Here, the new method called the hybrid data transformation should be employed. The process requires some interpretation or expectation of the changes in the structure since the first step requires that the seismic

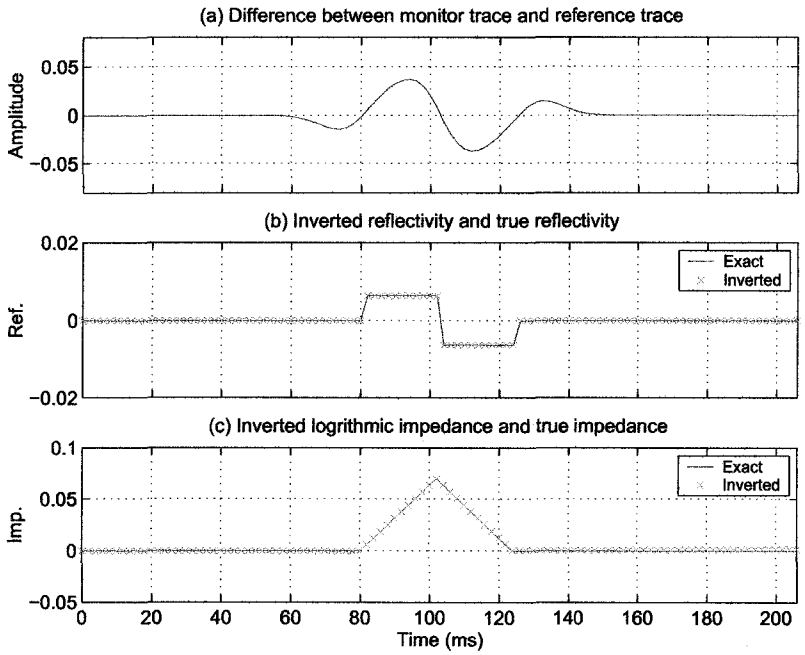

Figure 2.22: Inverted "reflectivity" and "impedance" by the application of the hybrid data transformation procedure.

difference be either differentiated (for ramp structures) or integrated (for thin beds) appropriately. Once an appropriate selection is made, this new method can be employed to invert "reflectivity" which is then converted to "impedance". This technique has been successfully tested on the synthetic seismic difference data with the typical thin bed and triangle structures. These structures might be encountered in the field time-lapse seismic monitoring.

This new method has several advantages. The first advantage is that it has high resistance to noise. The second advantage is that no external constraints are required in the inversion itself. The third advantage is that the non-uniqueness of the inverted "reflectivity" is significantly reduced. The fourth advantage is that the inverted "impedance" can be directly used to indicate the calendar impedance variations. This inversion procedure has provided a promising method to invert impedance variations from time-lapse seismic data acquired over a steam injection zone (e.g. *Zhang and Schmitt*, 2003a; *Schmitt*, 1999).

Chapter 3

Background to the Senlac case study: An assessment of the feasibility of time lapse seismic monitoring

3.1 Introduction

In the first part of this chapter, a brief introduction on the local geology and reservoir characters in the East Senlac area will be given. In the second part, a feasibility study on time-lapse seismic monitoring in the East Senlac area will be systematically investigated. It consists of four parts. In the first part, the SAGD scenario with two stages of fluid substitution included is simulated. The effective rock properties at these two stages will be estimated using Gassmann's equation. The second part is to assess the potential risk that might be involved in East Senlac case by using the technical spreadsheet published by *Lumley et al.* (1997). The third part is to predict rock property caused seismic anomalies through the generated synthetic seismic data sets by using the 2-D finite difference algorithm. The last part is to investigate how to design the optimal seismic acquisition system , especially in the East Senlac area.

3.2 Senlac geology history and reservoir characteristics

The Senlac local geology and reservoir features are investigated mainly based on *Rokosh and Schmitt* (2002)'s work. According to *Rokosh and Schmitt* (2002), production in East Senlac pool is from the Dina-Cummings members of the Mannville Group, Cretaceous

Aptian Age. It is the channels of Aptian Age that incised the Pre-Mannville unconformity and became part of the McMurray Formation of northern Alberta and the laterally equivalent Dina member of the Mannville Group in east-central Saskatchewan (Figure 3.1). There are two major Dina- Cummings deposits evident in the Senlac area (Figures 3.2 and 3.3), informally named West and East Senlac, respectively. The interval between the Cummings coal to the unconformity is much thicker in the West field than the East field suggesting a deeper incision of the West valley.

The east Senlac Dina-Cummings field lies in Twp 40-Range 25, 26W3M (Figure 3.2). According to the previous operator (*CSResourcesLimited*, 1995), the semi-consolidated sands of the Dina member form the primary reservoir and were deposited in a continental, fluvial environment. Estuarine and marine shale and siltstones of the Cummings member cap and laterally seal the Dina member (*Nambudiri*, 1984; *Groeneveld*, 1990; *Zaitlin and Schultz*, 1990). At the top of the Cummings interval is a 2-3 meter thick coal that forms a good regional stratigraphic marker (*Groeneveld and Stasiuk*, 1990). This coal was also termed the Lloydminster coal by *Groeneveld and Stasiuk* (1990). Cummings sandstones in the East Senlac area are also oil-bearing, however the upper Cummings sandstones are very argillaceous. No gas cap is visible on well logs. The vertical oil leg ceases below the overlying Lloydminster sandstone, located about 10 meters above the coal, where wet sandstones are evident (Figure 3.4). The oil pool is underlain by 2-5 meters of water, from north to south, respectively. The underlying Devonian Duperow Formation is wet. Table 3.1 lists some of the reservoir characteristics.

Figure 3.5 shows the location of the SHOC seismic lines relative to the three horizontal well pairs (from north to south B1, B2 and B3) drilled by Encana during 1998. The northern- most horizontal well pair cuts directly through the north-south seismic line. The middle and southern well pairs do not cross the north-south seismic line. The water disposal well CS 4-18-40-25W3 offsets the north-south seismic lines by about 50 meters to the east and is used to tie the geology of the area to the seismic lines.

Figure 3.6 is an isopach of the Dina-Cummings reservoir by the previous operator, CS Resources Limited in 1995. We have not updated this map and use it for general reference only. The isopach map (Figure 3.6) indicates that the reservoir is essentially divided into northern and southern lobes, with the southern lobe onlapping the unconformity. The

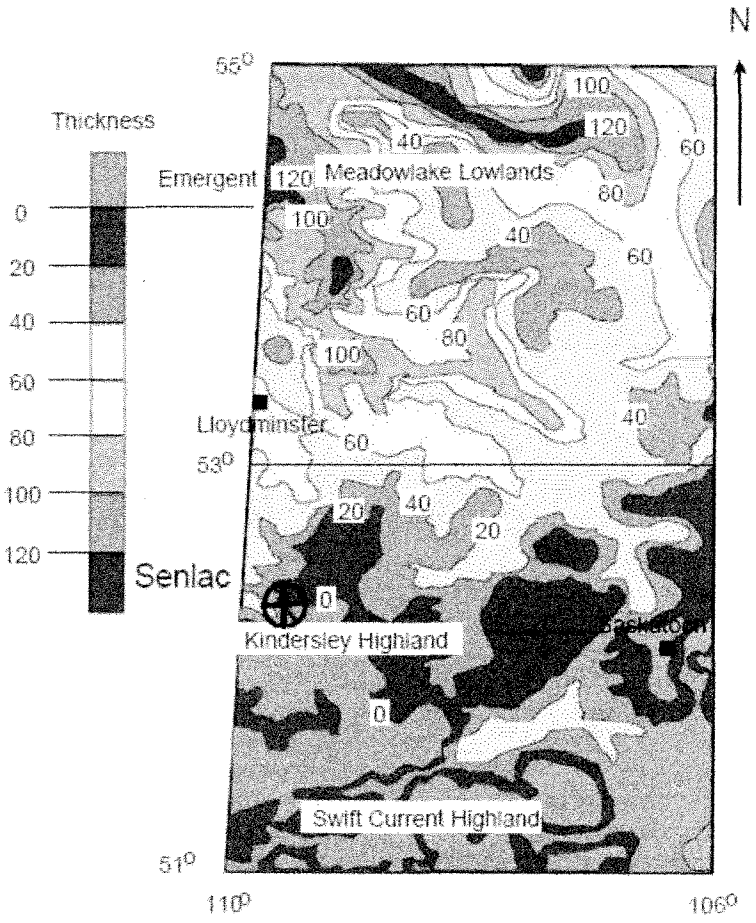

Figure 3.1: Isopatch of the Lower Mannville (Dina, Cummings) indicating a highly undulating topography at the beginning of Dina time. Modified after *Christopher* (1997) and *Rokosh and Schmitt* (2002). Contour interval is 20 meters.

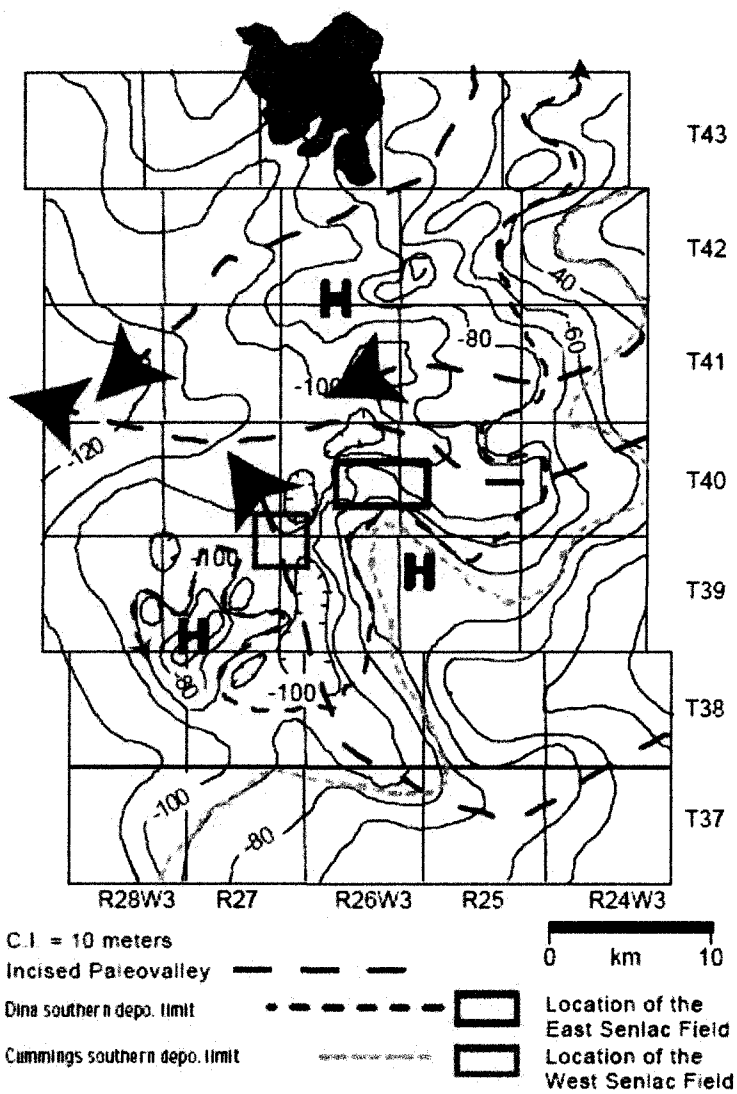

Figure 3.2: Structure on the PreMannville unconformity in east-central Saskatchewan. Modified after *Groeneveld and Stasiuk* (1990) and *Rokosh and Schmitt* (2002).

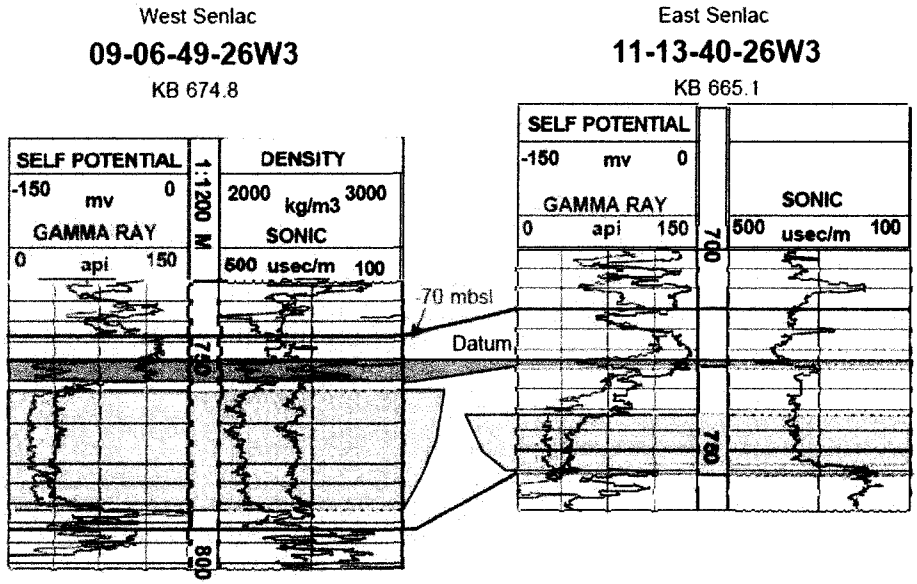

Figure 3.3: Stratigraphic cross-section comparing the channels at West and East Senlac. The datum is the top of the coal (*Rokosh and Schmitt*, 2002).

Table 3.1: Reservoir properties in East Senlac area (after *Chakrabarty et al.* (1998)).

Depth to the base of the reservoir	750 m
Initial reservoir temperature	28°C
Initial reservoir pore pressure	5 MPa
Overburden stress	16.5 MPa
Total oil pay thickness	8-12 m
Bottom water thickness	0-15 m
Permeability to air (from core analysis)	5-10 D
Porosity (from core analysis)	32.3%
Oil gravity	13°API($\approx$979 kg/m^3)
Density	980 kg/m^3
Oil viscosity (at reservoir condition)	5000 mPa·s
Oil saturation S_O	85%
Water saturation S_W	15%

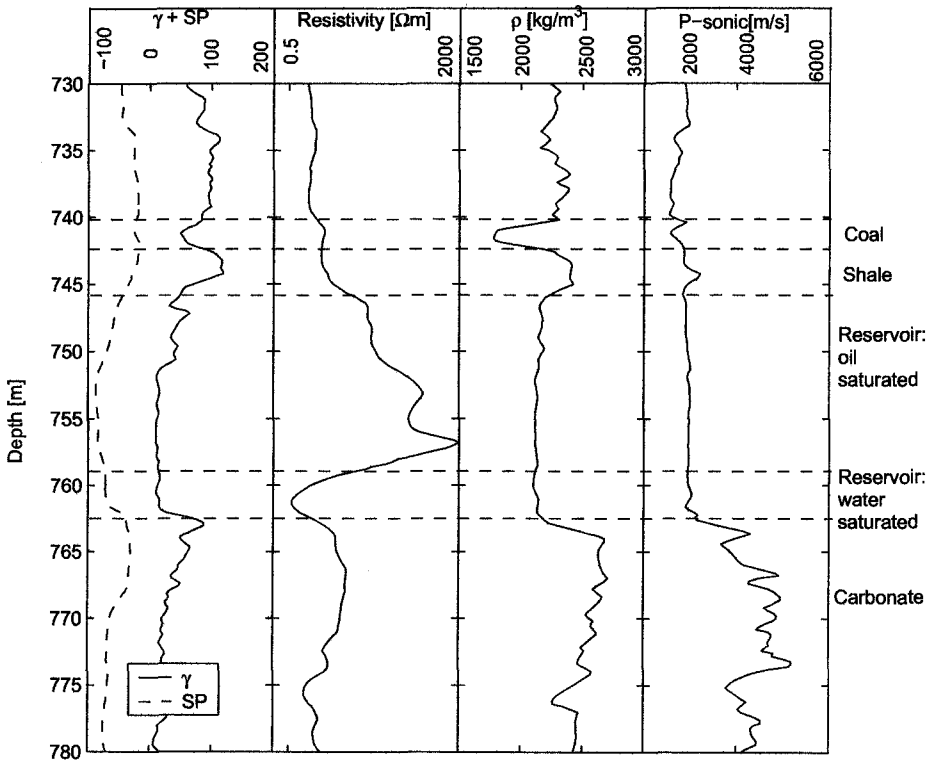

Figure 3.4: The East Senlac well log (CS Senlac SWD 04-18-040-25W3) including Gamma, spontaneous potential, resistivity, bulk density and sonic velocity logs.

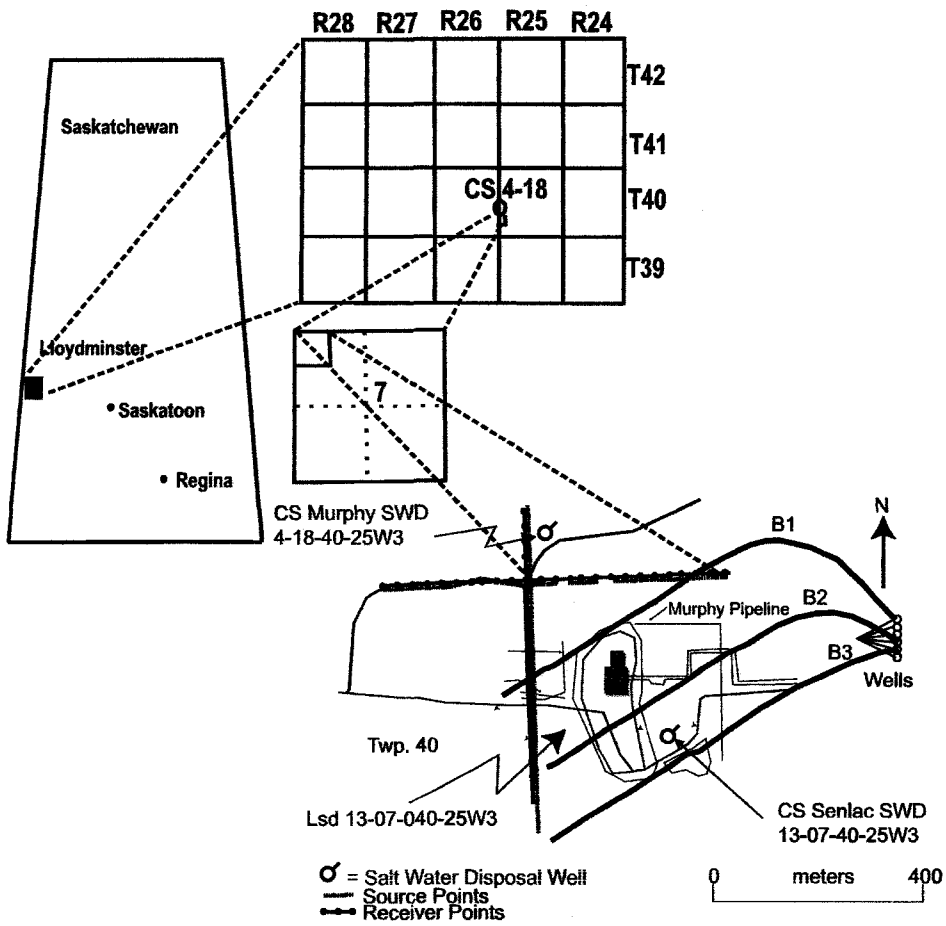

Figure 3.5: Location of the three horizontal well pairs relative to the seismic lines (after *Rokosh and Schmitt* (2002)).

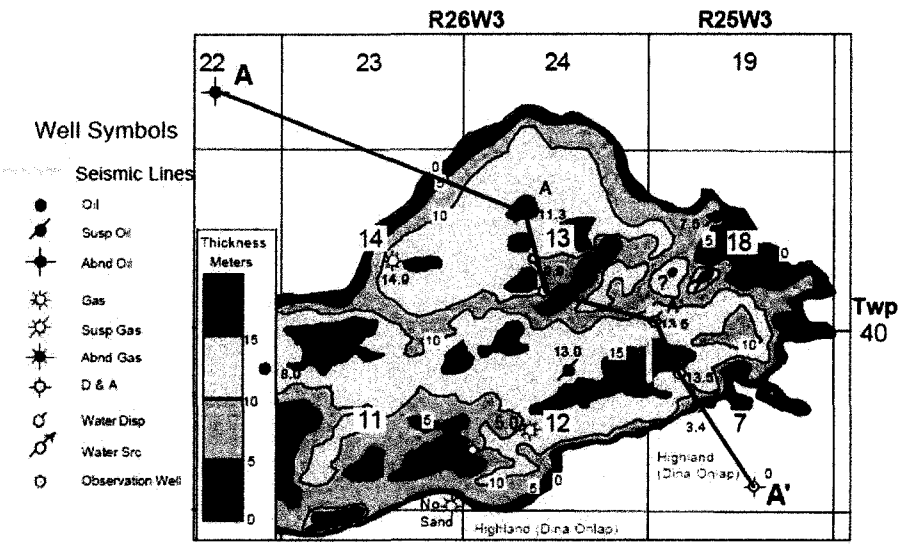

Figure 3.6: Total Dina-Cummings Net Pay Isopach (Isochron). Modified after *CSResourcesLimited* (1995) and *Rokosh and Schmitt* (2002).

seismic lines occur on the northeast flank of the southern linear feature where about 10-15 meters of net pay is expected.

3.3 Feasibility study

3.3.1 Elastic parameter estimation based on Gassmann's equation

An important aspect of time lapse surveys is to estimate in advance what the changes in the reservoir might be and how these will influence the *in situ* physical properties and the seismic response. Here we assume that the elastic parameters can be predicted on the basis of Gassmann's equation. The well log shown in Figure 3.4 is selected as the model to guide this prediction. The main purpose of this investigation is to estimate rock property variations. There are four major steps involved in this investigation.

Table 3.2: Brine parameters at the initial reservoir condition.

Pore pressure	5 MPa
Lithostatic pressure	16.5 MPa
Temperature	28°C
Salinity	40,000 ppm
Brine density	1025 kg/m^3
Brine sonic velocity	1521 m/s
Brine bulk modulus	2.37 GPa

Step 1: Estimation of frame modulus

From the well log shown in Figure 3.4, the sonic velocity and the bulk density are found roughly constant within sand reservoir in both the water and the oil saturated layers. The frame moduli within these two layers are therefore assumed to be uniform. As there is a great deal of information on the physical properties of water, it is relatively easier to estimate the frame modulus within the water saturated layer. The frame modulus within the oil saturated layer can be directly obtained from the value estimated within the water saturated layer.

The frame modulus within the water saturated layer will be first estimated. Under the initial reservoir condition and the given brine salinity and brine density (*Theune and Schmitt*, 2004), brine compressional velocity V_P can be calculated by using *Batzle and Wang* (1992)'s empirical formulas 27a, 27b, 28, 29. Please refer to the original reference from where these come from. Brine bulk modulus can then be further calculated by using the formula: $K_f = V_P^2 \rho_f$. The relevant brine parameters are listed in Table 3.2.

The greatest problem is estimation of the frame modulus K_d. In order to estimate frame modulus, *Gassmann* (1951)'s equation is first assumed valid. It must be noted, however, that while we employ this assumption in this case study we must question its validity in the context of heavy oil reservoirs. This is because the heavy oils may be able to support a viscosity dependent shear stress. Work is currently underway to better understand such processes, but our understanding is not yet sufficient to account for this problem, and as such this more conventional technique is employed. The frame modulus can be estimated by using the knowledge of the fluid and the mineral properties and from the observed sonic velocities. From the Gassmann's equation, 1.3, the frame bulk

modulus K_d can be can be written in the form,

$$K_d = \frac{1 + K_{eff}((\phi - 1)/K_s - \phi/K_f)}{(1 - K_{eff}/K_s + \phi)/K_s - \phi/K_f} \tag{3.1}$$

The effective bulk modulus K_{eff} can be calculated by using the following formula,

$$K_{eff} = \rho_{eff}(V_P^2 - \frac{4}{3}V_S^2) \tag{3.2}$$

The parameters such as the density ρ_{eff}, the compressional velocity V_P, and the shear velocity V_S can be directly measured from well logs. The solid material is assumed to consist of quartz, and the fluid is assumed to consist of brine. The porosity ϕ is directly obtained from the core sample measurement or estimated from other means. Therefore, the frame bulk modulus K_d can be calculated from equation 3.1.

The frame shear modulus μ_d usually can be assumed independent of fluid composition and can be calculated from the effective medium by using the following formula,

$$\mu_d = \mu_{eff} = \rho_{eff}V_S^2 \tag{3.3}$$

Within the water saturated layer, the calculated bulk frame modulus K_d and shear frame modulus μ_d are respectively 8.93 GPa and 4.58 GPa. The relevant input parameters and the estimated frame moduli are listed in Table 3.3. These frame moduli within the water saturated layer are assumed to be equal to those frame moduli within the oil saturated layer on the basis of the relative homogeneity in the reservoir zone. It is recognized that there may be many difficulties to this assumption, but in the absence of additional information more accurate prediction cannot be made.

Step 2: Oil substitution with steam

During SAGD related activities, as the high-temperature steam is continuously injected into the reservoir area and the steam chamber will expand until most of the pore space is filled with high temperature steam, with the residual oil remaining within the depleted reservoir. In this East Senlac SAGD reservoir model, the oil is assumed to be replaced by high-temperature steam at the first stage of fluid substitution. During this process, pore pressure remains constant at 5 MPa.

At the initial reservoir conditions with temperature at 28°C provided by the operators of the reservoir, the oil saturation S_O is assumed to be 85%, and water saturation S_W

Table 3.3: Input parameters and the estimated frame moduli within the water saturated layer at the initial reservoir conditions.

Porosity	ϕ	0.323
Bulk modulus	K_s	36 GPa
	K_f	2.37 GPa
Effective medium	V_P	2980 m/s
	V_S	1470 m/s
	ρ_{eff}	2130 kg/m^3
	K_{eff}	12.6 GPa
	μ_{eff}	4.58 GPa
Frame modulus	K_d	8.93 GPa
	μ_d	4.58 GPa

Table 3.4: Rock properties within oil saturated layer at the initial reservoir condition.

Temperature		28°
Pore pressure		5 MPa
Saturation	S_O	0.85
	S_W	0.15
Velocity	V_P	2960 m/s
	V_S	1460 m/s
Density	ρ_{eff}	2130 kg/m^3
Bulk modulus	K_O	2.5 GPa
	K_W	2.37 GPa
	K_f	2.48 GPa
	K_{eff}	10.9 GPa

15%. Once the oil is substituted by steam, the reservoir temperature rises to 263.94°C. Oil saturation S_O decreases to 20%, and water saturation S_W remains constant at 15%. The new component steam occupies 65% of the pore space.

Within the oil saturated layer, the relevant parameters at the initial reservoir condition are listed in Table 3.4. After oil substituted by steam, the relevant parameters are listed in Table 3.5.

Step 3: Steam substitution with gas (methane) under the constant temperature at 263.94°C and pore pressure at 5 MPa

As mentioned before, at the initial SAGD stage, steam is continuously injected into a horizontal well so that the communication between the production and injection wells

Table 3.5: Rock properties estimated during the process of oil substitution by steam.

Temperature		263.94°C
Pore pressure		5 MPa
Oil parameters	ρ_O	810 kg/m^3
	K_O	0.38 GPa
	S_O	0.20
Steam parameters	ρ_{St}	25.35 kg/m^3
	V_P	498.04 m/s
	K_{St}	0.0063 GPa
	S_{St}	0.65
Water parameters	ρ_W	777.37 kg/m^3
	V_P	1087.8 m/s
	K_W	0.92 GPa
	S_W	0.15
Fluid property	ρ_f	295 kg/m^3
	K_f	0.0096 GPa
Effective medium	ρ_{eff}	1891 kg/m^3
	K_{eff}	8.95 GPa
	V_P	2820 m/s
	V_S	1556 m/s

can be established in a short time. Once the economic limit has been reached, steam injection ceases and non-condensable gas is injected (*Yee and Stroich*, 2004). The main purpose to inject gas is to reduce production cost, maintain pore pressure and prevent heat loss.

At the second stage of fluid substitution, steam is assumed to be completely replaced by methane. During this process, reservoir temperature remains at 263.94°C; this consequently locks the temperature to the thermodynamically 263.94°C as there is mixed steam-liquid water based on the thermophysical properties of fluid systems from NIST Chemistry WebBook at webpage: *http : //webbook.nist.gov/chemistry/fluid/*. The pore pressure is assumed to remain exactly at 5.000 MPa. Of course, in a realistic situation there will be much more variance in these values, but we retain the exact value of 5.000 MPa of pressure for illustrative purposes. We have retained reporting the temperature to 5 significant digits only because these are obtained from the well known steam relationships for water. The calculated parameters are listed in Table 3.6.

Table 3.6: Relevant parameters used during the process of steam substitution with methane.

Temperature		263.94°C
Pore pressure		5 MPa
Oil parameters	ρ_O	810 kg/m^3
	K_O	0.38 GPa
	S_O	0.20
Methane parameters	ρ_{Me}	17.87 kg/m^3
	V_P	588.18 m/s
	K_{Me}	0.0062 GPa
	S_{Me}	0.65
Water parameters	ρ_W	777.37 kg/m^3
	V_P	1087.8 m/s
	K_W	0.92 GPa
	S_W	0.15
Fluid property	ρ_f	290.22 kg/m^3
	K_f	0.0094 GPa
Effective medium	ρ_{eff}	1890 kg/m^3
	K_{eff}	8.95 GPa
	V_P	2820 m/s
	V_S	1560 m/s

Step 4: generation of a summary table

In the previous sections, there are two different stages of fluid substitution included. At the first stage, oil is substituted by high temperature steam. At the second stage, steam is replaced by methane gas. These relevant parameters are summarized in Table 3.7. These parameters include fluid bulk modulus K_f, frame bulk modulus K_d, effective bulk modulus K_{eff}, density ρ_{eff}, compressional velocity V_P, and shear velocity V_S.

To reiterate, two differing conditions that are expected at different time points in the life cycle of a SAGD steam zone have been implemented. The first scenario is to simulate the steam chamber at a mature stage. During this process, 65% of the oil is replaced by steam, and the steam chamber temperature rises from the initial temperature of 28°C to the 263.94°C. Meanwhile, the pore pressure remains constant at 5 MPa. The second scenario is to simulate methane injection into steam chamber. At this second stage simulation, steam is completely replaced by gas, and the temperature remains at 263.94°C and the pore pressure at 5 MPa.

Table 3.7: Summarized rock properties within the oil saturated layer.

Parameters	Reservoir condition	Oil replaced by steam	Steam replaced by gas
$K_f[GPa]$	2.48	0.0096	0.0094
K_d [GPa]	8.93	8.93	8.93
K_{eff} [GPa]	10.9	8.95	8.95
$\rho_{eff}[kg/m^3]$	2130	1890	1890
V_P [m/s]	2960	2820	2820
V_S [m/s]	1460	1560	1560

The rock property variations are summarized in Table 3.8. During the process of oil substitution by steam, the effective fluid bulk modulus K_f is found to decrease significantly from the initial 2.48 GPa to the 0.0096 GPa. The relative variation is -99.6%. This variation indicates that fluids can be compressed significantly during this thermal process. The high temperature steam has directly made this contribution. This can be seen from tables 3.4 and 3.5. Heating also causes the oil bulk modulus K_O to decrease from the initial 2.5 GPa to 0.38 GPa and the water bulk modulus K_W from 2.37 GPa to 0.92 GPa. The new component, steam bulk modulus K_{St}, is 0.0063 GPa. The steam bulk modulus is the smallest among the three fluid components, but it occupies 65% of the whole fluid volume. It is the existence of this gaseous steam that results in the dramatic decrease in fluid bulk modulus K_f. However, the greater contribution to the overall effective bulk modulus K_{eff} is from frame bulk modulus K_d which accounts for 82.1% at the initial reservoir condition and 99.8% after oil is substituted by steam.

In addition to the significant decrease in the fluid bulk modulus, there is also significant decrease in the density of -11.1%. The main reason is the existence of the very small density in steam which occupies a greater volume of fluid pore space. The variation in compressional velocity V_P is relatively small (-4.6%) while the shear wave velocity increases by +6.9%.

During the process of steam substituted by gas (methane) under the constant pressure at 5 MPa and the constant temperature at 263.94°C, only the fluid bulk modulus K_f has changed with minor variations of 2.08% which is too small to be detected from seismic signals. Therefore, seismic variations due to gas injection will not be further investigated in the subsequent feasibility study.

Table 3.8: Summarized rock property variations within the oil saturated layer.

Parameters	Reservoir condition to oil replaced by steam	Steam replaced by gas
Variation in K_f [%]	-99.6	2.08
Variation in ρ_{eff} [%]	-11.1	0.0
Variation in K_d [%]	0.0	0.0
Variation in K_{eff} [%]	-17.8	0.0
Variation in V_P [%]	-4.6	0.0
Variation in V_S [%]	+6.9	0.0
Variation in P-impedance [%]	-15.4	0.0
Variation in S-impedance [%]	-5.2	0.0

It should be mentioned here that in the above simplified fluid substitution, the factors, such as heat absorption, fracture, subsidence, etc., are not considered. In the field time-lapse seismic monitoring, these factors may complicate seismic signals and should be considered in both future numerical simulation, *in situ* measurements, and laboratory validations. Further, for purposes of this analysis, we ignored any possible effect of temperature on the rock frame moduli. We recognize that this may be problematic as there is evidence to show that the shear moduli of such materials likely decrease with temperature (*Winkler*, 1985; *Wang and Nur*, 1988; *Zou and Bentley*, 2003, e.g.). A more involved analysis should include a proper reservoir simulation so that one could determine the expected values of the saturation, pore (reservoir) pressure, and temperature.

3.3.2 Technical risk assessment

As the second part of the feasibility study, a technical risk assessment on time-lapse seismic monitoring will be evaluated based on the spreadsheet published by *Lumley et al.* (1997). It consists of evaluations of the reservoir features and seismic properties. Each aspect can be calculated and evaluated by the given scorecard. When the estimated score is equal to or more than 60% of the total score, generally it is considered feasible to conduct time-lapse seismic monitoring experiment.

The parameters in the reservoir scorecard consists of the frame bulk modulus K_d, the fluid compressibility contrast K_{cp}, the oil saturation change ΔS_O, the porosity ϕ, and

Table 3.9: Standard reservoir scorecard and the assigned marks for East Senlac case. Data sources: L - values set by *Lumley et al.* (1997); ES - values estimated for East Senlac case.

	Score	5^L	4^L	3^L	2^L	1^L	0^L	Score^{ES}	Value^{ES}
K_d	GPa	< 3	$3 \sim 5$	$5 \sim 10$	$10 \sim 20$	$20 \sim 30$	30+	3	8.93
K_{cp}	%	250+	$150 \sim 250$	$100 \sim 150$	$50 \sim 100$	$25 \sim 50$	$0 \sim 25$	2	−99.6
ΔS_O	%	50+	$40 \sim 50$	$30 \sim 40$	$20 \sim 30$	$10 \sim 20$	$0 \sim 10$	5	65
ϕ	%	35+	$25 \sim 35$	$15 \sim 25$	$10 \sim 15$	$5 \sim 10$	$0 \sim 5$	4	32.3
ΔI_P	%	12+	$8 \sim 12$	$4 \sim 8$	$2 \sim 4$	$1 \sim 2$	0	5	−15.2

the predicted impedance change ΔI_P. The fluid compressibility contrast is defined as fluid bulk modulus percentage change, and the predicted impedance change is defined as the relative variation in the product of compressional velocity and density (*Lumley et al.*, 1997). The standard reservoir scores and the assigned marks for the East Senlac case are listed in Table 3.9.

In the second part, the seismic scorecard considers the seismic image quality, the vertical seismic resolution, fluid contacts, and repeatability. To some degree, these factors are subjective and require some experience to properly assess. The standard scores and the assigned marks for East Senlac case are listed in Table 3.10.

The reservoir scorecard and the seismic scorecard for the typical published cases and East Senlac case are summarized in Table 3.11. The full score for the ideal time-lapse seismic monitoring is 45. The passing benchmark should be at least equal to or more than 60% of the total mark. Therefore, the base benchmark should be at least 27. For the East Senlac case, the total reservoir and seismic score is 30 which barely passes the required minimum score. For further reference, the features of the published case studies and the East Senlac case are summarized in Table 3.12.

The total reservoir score in East Senlac area is 19, higher than the base benchmark 15 out of total mark 25 (*Lumley et al.*, 1997). It is slightly higher than that of West Africa. As is found from Table 3.12, the reservoirs at these two locations consist of consolidated rocks with stiff frame matrix. Refer to Table 3.11, the East Senlac reservoir is expected

Table 3.10: Standard seismic scorecard and the assigned marks for East Senlac case. Data sources: L - set by *Lumley et al.* (1997); ES - values estimated for East Senlac case.

Seismic parameters	Description	Score^L	Score^{ES}
Image quality	Good S/N in the stack or migration;	1	1
	A clear image of reservoir reflection;	1	1
	Reliable and meaningful amplitudes in the reservoir image;	1	1
	No multiples or coherent noise etc. contaminating the reservoir zone;	1	0
	No shallow gas, statics, or velocity anomalies, etc. blurring the reservoir image;	1	1
Seismic resolution	Reservoir thickness $>$ average resolution	1	0
	Reservoir thickness $>$ 1 average resolution;	1	0
	Reservoir thickness $>$ 2 average resolution;	1	0
	Reservoir thickness $>$ 3 average resolution;	1	0
	Reservoir thickness $>$ 4 average resolution;	1	0
Fluid contacts	At least one seismic fluid contact is visible in cross section;	1	1
	Several seismic fluid contacts are visible in cross section;	1	0
	One seismic fluid contact can be mapped locally;	1	1
	Several seismic fluid contacts can be mapped locally;	1	0
	All seismic fluid contacts can be mapped locally;	1	0
Repeatability	The same acquisition method was used for each survey;	1	1
	Permanent source/receiver array installation was used;	1	1
	The accuracy of the source/receiver repositioning was verified with time-lapse specs for each survey;	1	1
	Same shooting direction was used for each survey;	1	1
	The same bin spacing and offset/azimuth distribution was used for each survey.	1	1

Table 3.11: Reservoir and seismic scorecard summary. Data sources: L - values set by *Lumley et al.* (1997); PCS - published case study; ES - East Senlac.

	Ideal^{L}	Indonesia^{PCS}	Gulf of Mexico^{PCS}	West Africa^{PCS}	North Sea^{PCS}	East Senlac^{ES}
Reservoir						
Frame bulk modulus	5	5	4	3	2	3
Fluid compress contrast	5	5	4	3	4	2
Fluid saturation change	5	5	5	4	3	5
Porosity	5	5	4	4	3	4
Predicted impedance change	5	5	4	3	3	5
Reservoir total	25	25	21	17	15	19
Seismic						
Image quality	5	4	5	4	3	4
Resolution	5	5	4	3	1	0
Fluid contact	5	4	4	4	2	2
Repeatability	5	5	4	4	2	5
Seismic total	20	18	17	15	8	11
Total score	45	43	38	32	23	30

Table 3.12: Fundamental features of published case studies and the East Senlac case. Data sources: PCS - published case study; ES - East Senlac case.

Case Study	Main Characters
Indonesia^{PCS}	• High porosity, highly unconsolidated rock, thick reservoir; • Permanent source/receiver installation, frequency at 250Hz using dynamite.
Gulf of Mexico^{PCS}	• High porosity, fairly unconsolidated, good contrast between oil and brine; • Repeatable hydrophone, frequency up to 100Hz, multiple local reservoir fluid contacts.
West Africa^{PCS}	• More consolidated rock; • Strong non-repeatable acquisition.
North Sea^{PCS}	• More consolidated rock; • Strong non-repeatable acquisition.
East Senlac^{ES}	• High porosity, consolidated rock, thin reservoir; • Repeatable acquisition, low frequency about 25Hz.

matchable to these two areas, West Africa and North Sea which are feasible to implement time-lapse seismic monitoring project. But great challenges have been encountered (*Lumley et al.*, 1997). For the East Senlac case, a similar scenario might be predicted to occur.

Referring to Tables 3.10 and 3.11, the seismic score in East Senlac case is 11, lower than the required benchmark 12 out of 20. The highest mark is assigned in repeatability aspect since the shot and geophone positions are well maintained in each survey by using differential GPS equipment. Although pumps caused noise, the seismic image which has higher CMP stack fold numbers shows high image quality, and therefore, the score is set 4. The mark in vertical seismic resolution aspect is set to zero. This is based on the approximated calculations. Within the target reservoir area, the seismic main frequency is about 25Hz, and the average compressional velocity measured from the nearby well log is about 2900m/s. Based on the 1/4 wavelength resolution definition, the resolvable thickness is 29m. The actual measured reservoir thickness is known about $10 \sim 12$ m which is smaller than the calculated half vertical resolution. However, the problem should be looked at not so much in terms of being able to 'resolve' the time lapse anomalies, but more to 'detect' them as any variations observed are likely to be more subtle amplitude changes as was seen in the previous section.

The total score for East Senlac case is 30, slightly lower than that of West Africa and a little higher than that of the North Sea. The reservoir formations in these three areas all consist of consolidated rocks. However, there exist seismic differences in data repeatability and seismic resolution. The East Senlac seismic surveys possess excellent repeatability, but relatively lower resolution. In contrast, both West Africa and North Sea seismic surveys have relatively higher resolution, but poor repeatability. It is reported that the West Africa offshore 4-D projects have shown very encouraging results; the North Sea case study has demonstrated subtle, less confident variations (*Lumley et al.*, 1997). In those two case studies, there is no obvious time shift between the seismic calendar surveys. The only observed variations are in the seismic amplitude. Similar scenario is predicted to occur for East Senlac case. The magnitude of amplitude variations and the confidence in these variations should be equivalent to the West Africa case and the North Sea case. As for Indonesia case and Gulf of Mexico case, they have excellent reservoir and

Table 3.13: Seismic parameters used in forward seismic modelling.

Frequency	Peak frequency	32 Hz
	Maximum frequency	60 Hz
Geometry	Grid size	3x3 m
	Shot interval	9 m
	Geophone interval	3 m
	Sample rate	1 ms
	Total Shot Number	67
	Total Geophone Number	216
Base survey	Density	2130 kg/m^3
	Compressional velocity	2960 m/s
Monitor survey	Density	1890 kg/m^3
	Compressional velocity	2820 m/s

seismic conditions, and they have demonstrated great success in field time-lapse seismic monitoring experiments.

3.3.3 Forward seismic modelling

Forward seismic modelling is another part of this feasibility study. The main goal of this investigation is to predict the possible seismic variations that may occur in the time-lapse seismic monitoring. A 2-D finite difference algorithm developed by Seismic Unix (Colorado Mines School) is employed in this process. The previously estimated densities and compressional velocities are adopted to build the impedance model. The same geometry designed for the East Senlac field experiment described in chapter 5 are used in this forward modelling. Based on the geological structure and the designed geometry configuration, two seismic calendar surveys are generated. They individually represent the base survey and the monitor survey. The source wavelet frequency is estimated from East Senlac seismic reflection data. The relevant parameters used to generate forward seismic model are listed in Table 3.13.

The shot and geophone geometry is shown in Figure 3.7. In order to suppress numerical noise, the 67 shots are located at a depth of 3 meters and the 216 geophones at a depth of 30 meters. In addition, extra grids are appended on the left, right, and bottom sides of the finite difference mesh in order to avoid the numerical complications due to the model boundaries (i.e artificial side reflection) at the time windows of interest.

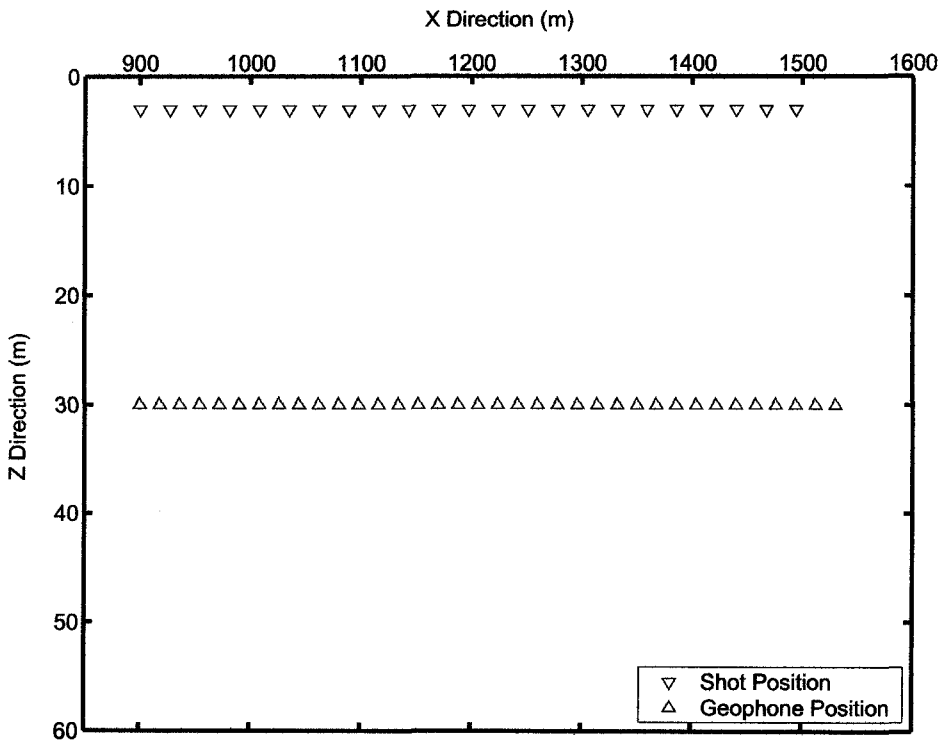

Figure 3.7: Shot and geophone geometry configuration.

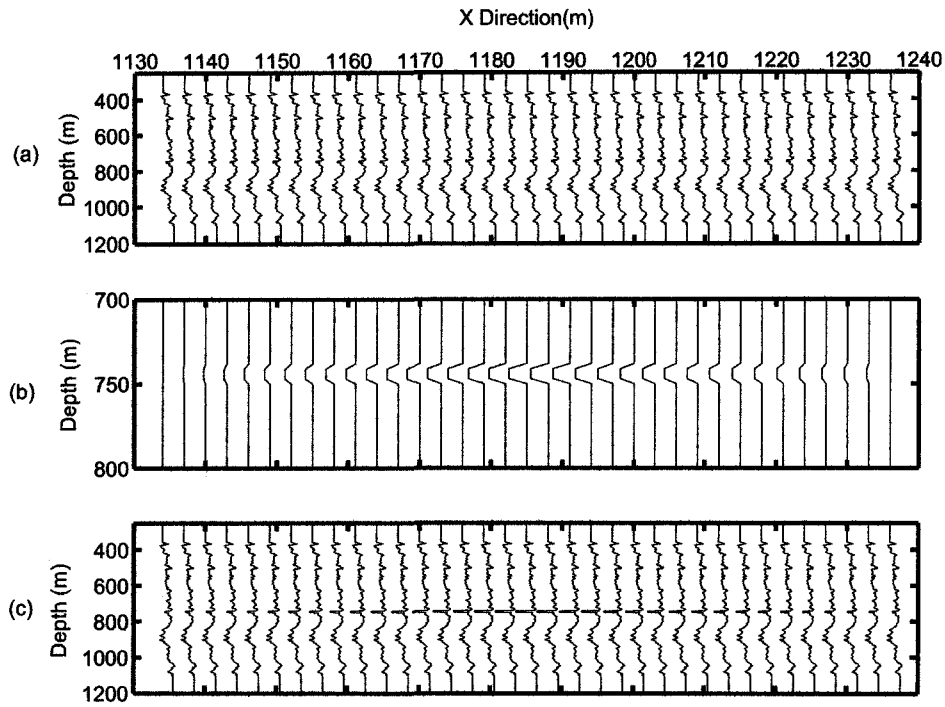

Figure 3.8: Density distribution as a function of depth and horizontal positions. (a) Base density survey;(b) Density variations. (c) Monitor density survey.

The base 2-D density and velocity models are shown in Figure 3.8(a) and 3.9(a). With the added small variations shown in Figure 3.8(b) and 3.9(b), the generated monitor density and velocity models are shown in Figure 3.8(c) and 3.9(c). The added density and velocity variations are based on the established SAGD model published by *Butler and Yee* (2002). Based on this SAGD model, as high temperature steam is injected into reservoir area, the steam chamber usually can expand laterally as far as 50 meters away from the steam injection point. Therefore, for East Senlac SAGD model, if the steam injection point is assumed to locate at x=1185 m with the maximum density variation -11.1% and the maximum velocity variation -4.6%, the steam chamber will expand laterally until to reach x=1134 m and x=1236 m. The density and velocity are assumed to change linearly from the centre to the edge of the anomaly.

Based on the density and velocity model generated, the two post-stack seismic pro-

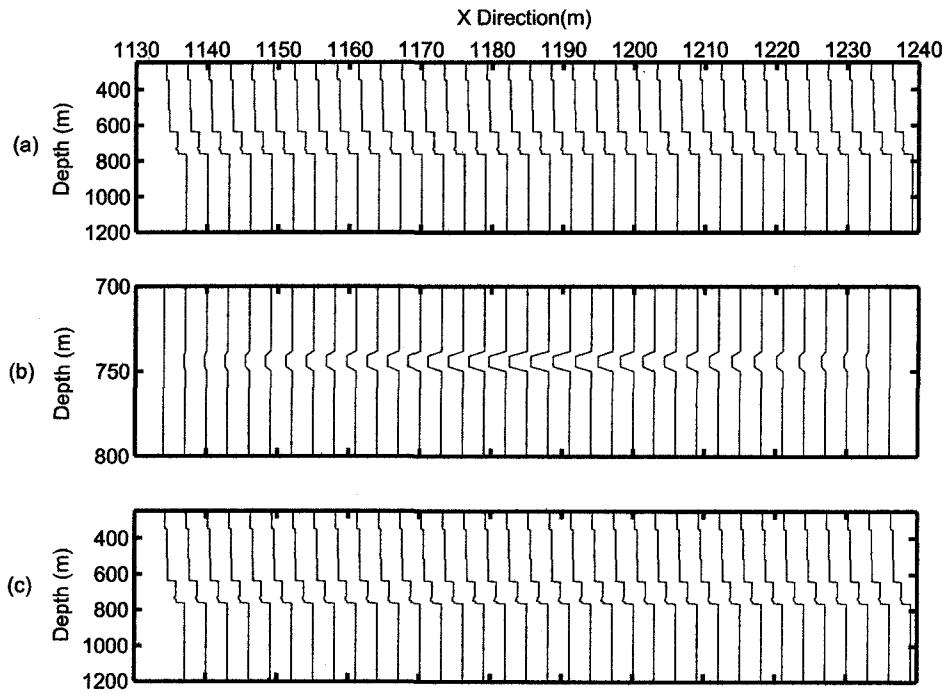

Figure 3.9: Velocity distribution as a function of depth and horizontal positions. (a) Base velocity survey; (b) Velocity variations; (c) Monitor velocity survey.

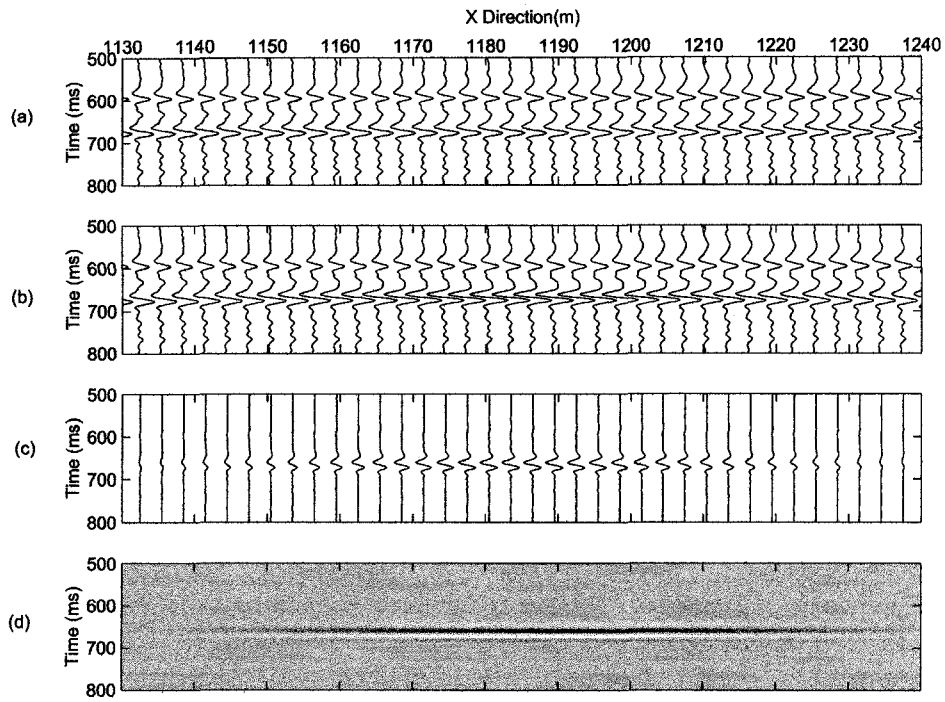

Figure 3.10: The post-stack seismic profiles. (a) Base seismic profile; (b) Monitor seismic profile; (c) Seismic difference between base survey and monitor survey; (d) The same as (c) except shown in grey scale format.

files are shown in Figure 3.10(a) and 3.10(b). The difference between these profiles is shown in Figure 3.10(c) from which only seismic amplitude variations can be observed with the biggest variation at the steam injection point. This observation is consistent with the previous prediction in the technical risk assessment. This modelling highlights an important fact that the seismic monitoring of thin reservoirs is possible but that one will have to employ variations in amplitude to detect changes. Interpretation of such amplitude variations will rely on forward modelling.

In order to illustrate how the pseudo steam chamber grows, a series of forward seismic models are generated. The initial velocity and density distributions are shown in Figures 3.11 and 3.12. Suppose within the assumed reservoir zone that there is a maximum 9% velocity decrease at the mid CMP position. From this point, velocity variation increases steadily until at 50m, 100m, 150m, 200m, 250m and 300m away from the injec-

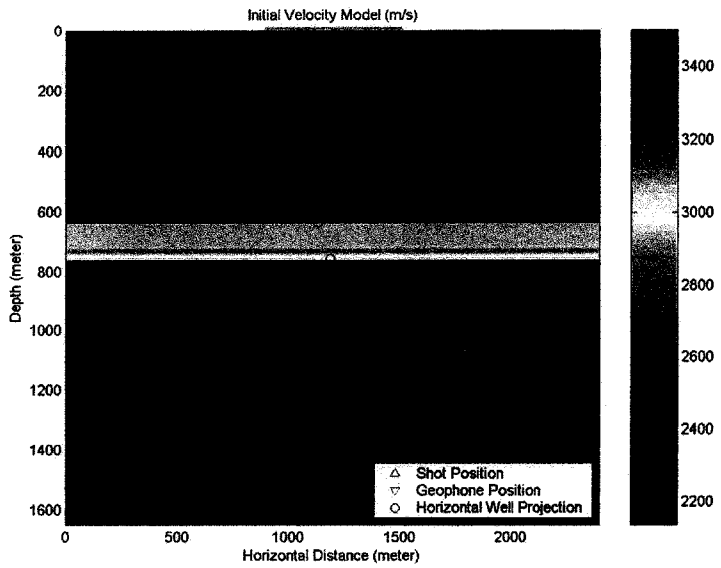

Figure 3.11: Initial velocity model.

tion point, there is no velocity change any more. Here, density is assumed not to change from the reference survey to the monitor survey. The generated initial velocity distribution and the velocity distributions with disturbances added are shown in Figure 3.13. The generated synthetic post stack seismic profiles are shown in Figure 3.14. To compare the first profile with the remaining profiles, brighter seismic amplitudes can be observed, especially at the pseudo injection point. More salient features can be further observed from the calculated seismic difference profiles as shown in Figure 3.15.

3.3.4 Time-lapse seismic survey design

The design of the acquisition geometry is an important component of the feasibility study in the time-lapse seismic monitoring. The amplitude variations and time shifts are the commonly observed characteristics. A variety of factors, such as the reservoir thickness, the seismic wave velocity, and the density, to name a few, directly affect these variations. The main goal of this section is to investigate how these factors will affect seismic variations. Meanwhile, how to design the optimal acquisition geometry for the East Senlac

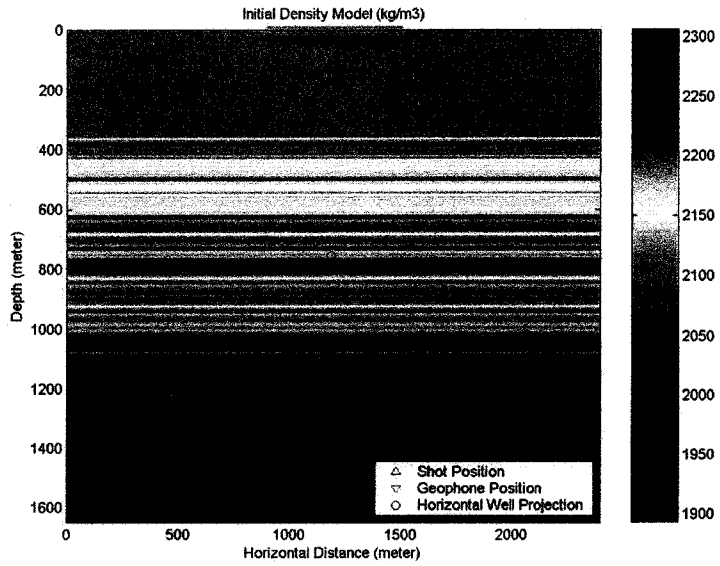

Figure 3.12: Initial density model.

case will also be described.

Factors to affect the time-shift

When the shot and geophone are simultaneously located at the reservoir surface, the quantified time difference can be directly estimated by using the following formula (*Li et al.*, 2004),

$$dt = \frac{t_{01}(1+k)dt_{01}}{t_1} \tag{3.4}$$

where t_{01} represents the two-way vertical travel time through the reservoir, dt_{01} is the corresponding vertical time variation, t_1 is the travel time through reservoir starting from shot to geophone, and dt is the corresponding time difference. The parameter k represents:

$$k = x^2/(4h^2) \tag{3.5}$$

where x is the offset between the shot and the geophone, and h is reservoir thickness. The derivation of formula 3.4 is summarized in Appendix A. Within the reservoir area, if the reservoir thickness, the initial velocity, and velocity variation are assumed constant, the

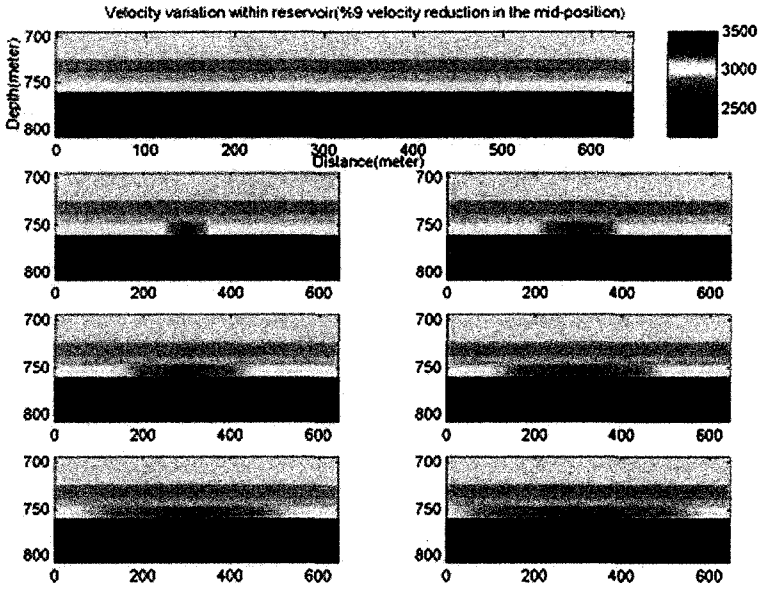

Figure 3.13: The generated series of velocity distributions (m/s).

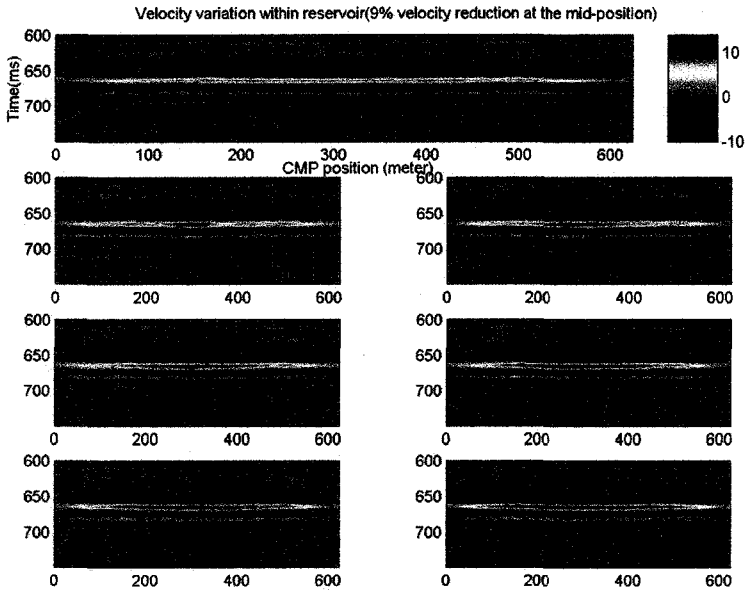

Figure 3.14: Post stack synthetic seismic profiles.

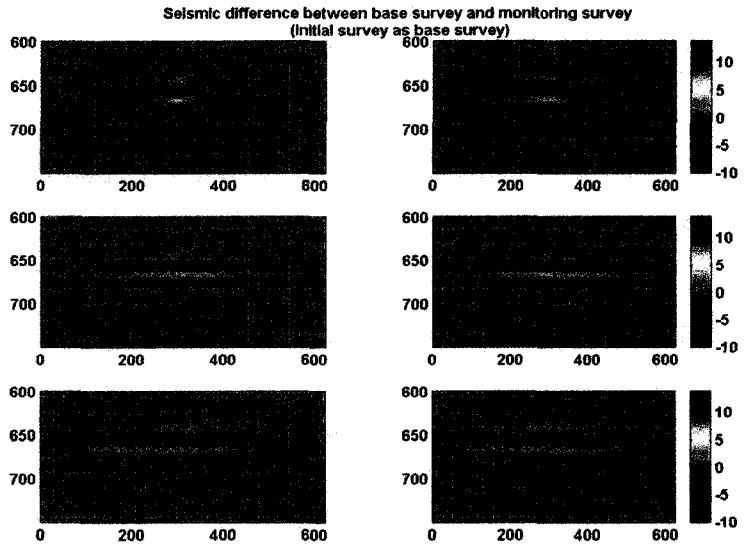

Figure 3.15: Seismic difference profiles with the initial seismic as the reference. Horizontal axis represents CMP position (m); vertical axis represents time (ms).

parameters t_{01}, dt_{01}, and h in the formula 3.4 are also constant. Substituting the formula $t_1 = \sqrt{4h^2 + x^2}/v_1$ and the formula 3.5 into the equation 3.4, we obtain,

$$dt = \frac{\sqrt{4h^2 + x^2}}{2h} dt_{01} \tag{3.6}$$

The offset x and time difference dt are the only variables, and the time difference dt increases with the offset x. Theoretically, if the offset is large enough, a significant time difference can always be obtained, even if the velocity variation within the reservoir area is very small. However, in practice this is impossible.

Here, equation 3.6 is used to investigate how the time difference dt changes with offset x for East Senlac case. Based on the previous estimation, the initial velocity is 2957 m/s and the velocity after fluid substitution is 2820 m/s. The selected reservoir thickness h is 12 m. Offset is set within the range [5, 700] m with 18 m offset intervals. The calculated time difference which changes with offset is shown in Figure 3.16. The time difference is found to increase quasi-linearly with offset. The calculated vertical travel time is individually 8.1163ms and 8.5046ms. The calculated time difference is 0.3883ms,

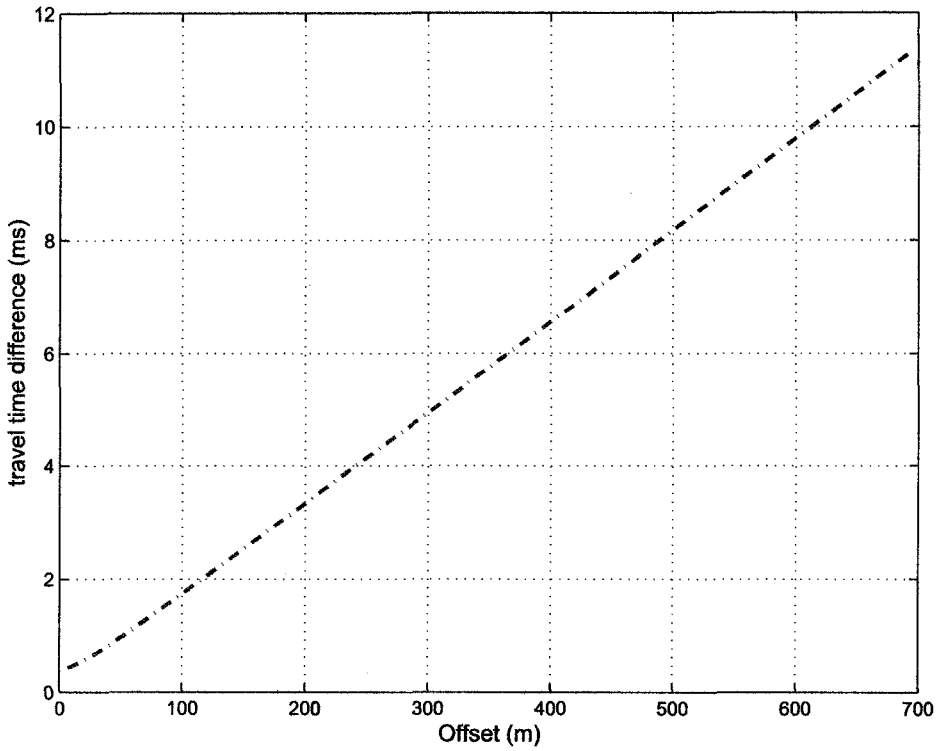

Figure 3.16: The time difference as a function of offset.

smaller than the 1 ms sample rate. Obviously, the time difference is impossible to be directly detected from post-stack seismic difference profile. However, when the offset increases to 351 m, the calculated time difference is 5.8 ms; when offset increases to 666 m, the calculated time difference is 10.9 ms, ten times of seismic sample rate. Therefore, a significant time difference can always be obtained by setting a larger offset.

The formula 3.6 is only valid when both the shot and the geophone are set at the reservoir surface, a case that is not realistic. For the surface seismic case, the geophone and the shots are usually located at the soil surface or buried at very shallow subsurface. In order to use the formula 3.6 to calculate the time difference, the shot and geophone should be manually extrapolated downward to the reservoir surface. Offsets for these two cases are different. For the shallow reservoir, offset deviation is relatively small. Therefore, a significant time difference can always be obtained by using a reasonable

offset. However, for the shallow reservoir case, seismic signals are heavily contaminated with noise. On the other hand, for deep buried reservoir, offset deviation calculated at the soil surface and at the reservoir surface is relatively bigger. Although obvious time differences can be obtained by setting a very large offset value at the soil surface, wide-angle reflection distortion (e.g. *Knapp and Steeples*, 1986; *Pullan and Hunter*, 1983) will be manifested on the seismic profile. These distortions are mainly caused by the non-nominal common-depth-point (CDP) fold and NMO stretching. Usually, data with 30 to 40 percent NMO stretch should be muted (*Denham*, 1979). The NMO stretch can be approximated by the following formula (*Knapp and Steeples*, 1986),

$$NMO_{stretch} \cong \frac{x^2}{2v_{NMO}^2 t_0^2} \tag{3.7}$$

where x represents offset, v_{NMO} represents stacking velocity, and t_0 is zero-offset one-way travel time. For example, if the maximum offset is assumed equal to the reflector depth ($x = d$), and t_0 equals d divided by average velocity which is slightly less than the stacking velocity v_{NMO}, the calculated NMO stretch sample is 50%.

Therefore, in the application of formula 3.6 to calculate time difference, some trade off has to be made for the shallow reservoir and for the deep buried reservoir. For the East Senlac case, the reservoir depth is about 750 meters, and the reservoir thickness is about 12 meters. The seismic sample rate is set 1 ms. If the offset at the reservoir surface is 96 meters with the calculated 1.6 ms time difference, then the extrapolated offset at the soil surface should be 6000 meters. Although this magnitude time difference might be detected from prestack time-lapse seismic data, the required large offset, as mentioned before, will produce wide angle reflection distortions. As a rule of thumb, the maximum offset should be set no more than the reflector depth (*Knapp and Steeples*, 1986). Therefore, for the East Senlac case, the maximum offset should not exceed 750 meters. As such, the calculated maximum time difference is less than 1 ms sample rate which is impossible to detect from time-lapse seismic difference profiles.

Factors to affect amplitude variations

As analyzed before, the East Senlac reservoir is thin relative to the wavelengths. This again emphasize the inferences of the previous modelling that it is amplitude variations

that are needed in the analysis of thin reservoir. Only amplitude variations are possibly observed in time-lapse seismic surveys. For a thin layer of thickness b, much of its amplitude behavior can be captured by the following formula (*Widess*, 1973),

$$A_d \cong 4\pi Ab/\lambda_b \tag{3.8}$$

where A is the average value between the amplitude of the predominate peak and trough amplitude when the wavelet crosses the first interface. The λ_b is the wavelength of the seismic waves passing through the thin bed.

Examination of this formula suggests that the seismic amplitude increases with interface contrast and reservoir thickness, and decreases with seismic wave length. Therefore, large seismic amplitude can be obtained by using high frequency seismic wave for the reservoir with significant interface contrast.

Since East Senlac reservoir can be considered as a thin-bed structure, the seismic amplitude variations for time-lapse scenario can be written as,

$$\Delta A_d = 4\pi(A_2 b_2/\lambda_{b2} - A_1 b_1/\lambda_{b1}) \tag{3.9}$$

If we assume the reservoir thickness $b_1 = b_2 = b$ and the seismic wave length $\lambda_{b1} = \lambda_{b2} = \lambda_b$, the formula 3.9 can be simplified as,

$$\Delta A_d = 4\pi(A_2 - A_1)b/\lambda_b \tag{3.10}$$

It is obvious that amplitude variation is directly related to the reservoir thickness b, the seismic wavelength λ_b, and the subsurface dynamic variation $(A_2 - A_1)$. Since the reservoir thickness and the dynamic variations are beyond control, efforts should be made toward improving seismic frequency so that significant seismic variations can be observed.

3.4 Summary

In this chapter, feasibility study has been systematically investigated. It consists of four aspects including elastic parameter estimation, technical risk assessment, forward seismic modelling and seismic data acquisition design. For the East Senlac case, based on Gassmann's equation, the estimated compressional velocity after fluid substitution decreases 4.6%, and density decreases 11.1%. The generated forward seismic modelling has

shown that only seismic amplitude variations can be detected from seismic difference profile. In the design of seismic data acquisition, the offset is suggested not to exceed the target reservoir depth which is about 750 m. Meanwhile, the high frequency and high energy source wavelet are recommended to be used during the process of seismic data acquisition. Once the steam chamber is mature, continuous injection of gas can only produce very small seismic variations, and these seismic variations will be difficult to be detected from field seismic experiments. Finally, technical risk assessment has shown that it is feasible to conduct time-lapse seismic field experiments in East Senlac area, but significant challenges will be encountered.

Chapter 4

The art of time-lapse seismic data processing

4.1 Introduction

Since the discovery made in the laboratory that rock properties change with temperature and pressure, *Nur* (1989) predicted that similar features might be observed from the field time-lapse seismic data. This discovery has led to the revolutionary development in the subsequent time-lapse seismic monitoring. To compare with regular seismic processing which has been developed for more than four decades, time-lapse seismic processing is relatively young, and very few public documents have discussed this issue. The main goal of this chapter is to investigate the relevant time-lapse seismic processing issues with the East Senlac seismic data as input sample data. Since our calendar data sets were highly repeatable in the aspect of source signatures, geophone and receiver positions, etc., we attempt to examine ways to make the processed seismic data as reasonable as possible so that the subsequently estimated seismic difference may be reliably highlighted.

In the time-lapse seismic data processing, choosing consistent parameters is very important. For example, if different stacking velocity functions were selected to process time-lapse seismic data, the subsurface reflectors would be imaged to different positions and artifacts would appear in the difference profiles (e.g. *Ross and Altan*, 1997). Although this problem can be partially solved by applying static time corrections, it will be difficult to apply the same static functions to correct the lateral mispositions and the dynamic

time shift which changes with depth. The selected time shift, even if less than one sample interval, will cause false time-lapse events in the difference profiles. Usually, such processing procedures or algorithms are called data dependent processing or noise sensitive processing. Other algorithms, such as deconvolution, refraction statics, surface consistent statics, and migration, to name a few, all belong to this processing category. These processing algorithms should be used carefully. Otherwise, unexpected noise or artifacts will be produced within the supposedly static geology zone of the difference seismic profile (*Ross and Altan*, 1997).

In time-lapse seismic data processing, selecting the appropriate processing strategy is also very important. Based on the different features of the acquired time-lapse seismic surveys, it can be roughly divided into three categories, including post-stack XEQ, prestack parallel processing (PPP), and prestack simultaneous processing (PSP) (*Lumley et al.*, 2003).

- XEQ is usually applied to legacy data sets which are or were acquired without time-lapse data design in mind;
- PPP emphasizes to apply similar or identical processing flows to two sets of time lapse data acquired at different times;
- PSP is to apply the jointly derived processing operators to the multi-vintage data sets.

Usually, time-lapse seismic surveys which are acquired with identical geometry design and similar source wavelet and processed with consistent parameters, are always superior to legacy data which are collected and processed without seismic repeatability in mind (*Lumley et al.*, 2003). In other words, better results can always be obtained by using PPP and PSP than by using post-stack XEQ processing.

The XEQ is another important component in the time-lapse seismic processing. The purpose of XEQ is to calibrate and reduce non-repeatability caused variations. The matched filtering method in time domain (MFM) and bandwidth and phase equalization method in frequency domain (BPEM) are the commonly employed XEQ methods (e.g. *Rickett*, 1997).

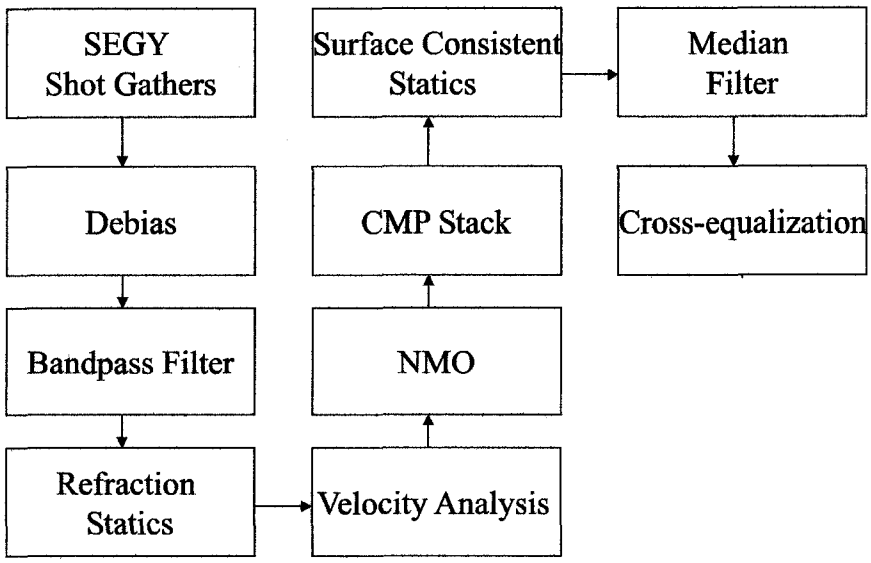

Figure 4.1: Time-lapse seismic processing flow.

In the first part of this chapter, the two processing strategies PPP and PSP will be described. Some pitfalls in the PPP will be addressed through the illustrated examples in which inconsistent parameters and separately extracted statistical operators will be selected. In the second part, the basic principles of the two XEQ methods, the MFM and BPEM will be described, and comparison between them will be further attempted. The final part is the summary to conclude this chapter. For the convenience of the subsequent discussion on time-lapse seismic data processing, the processing procedures adopted in this thesis and the final calendar images are shown in Figures 4.1, 4.2 and 4.3.

4.2 The art of time-lapse seismic data processing: part 1 - processing strategies

4.2.1 Prestack simultaneous processing (PSP)

To reiterate, the main idea of PSP is to use the identical processing parameters and to use the jointly derived operators to process the multi-vintage data sets. Although the idea is simple, optimal results can always be obtained by using this processing strategy when the time-lapse seismic surveys are designed for the purpose of time-lapse seismic

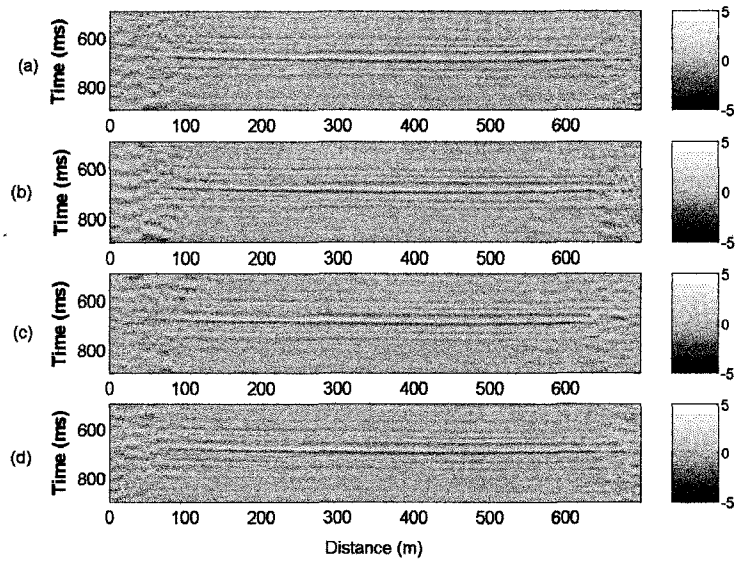

Figure 4.2: Time-lapse seismic profiles along the W-E direction. (a) July 2001; (b) October 2001; (c) June 2002; (d) October 2002.

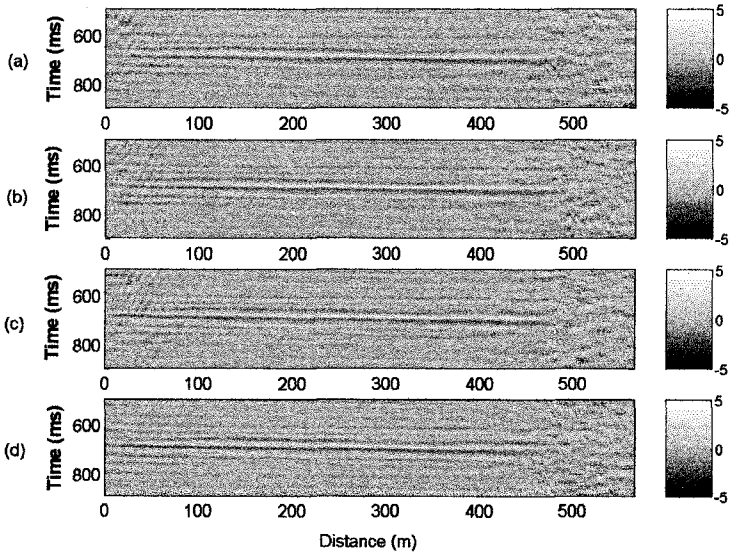

Figure 4.3: Time-lapse seismic profiles along the N-S direction. (a) July 2001; (b) October 2001; (c) June 2002; (d) October 2002.

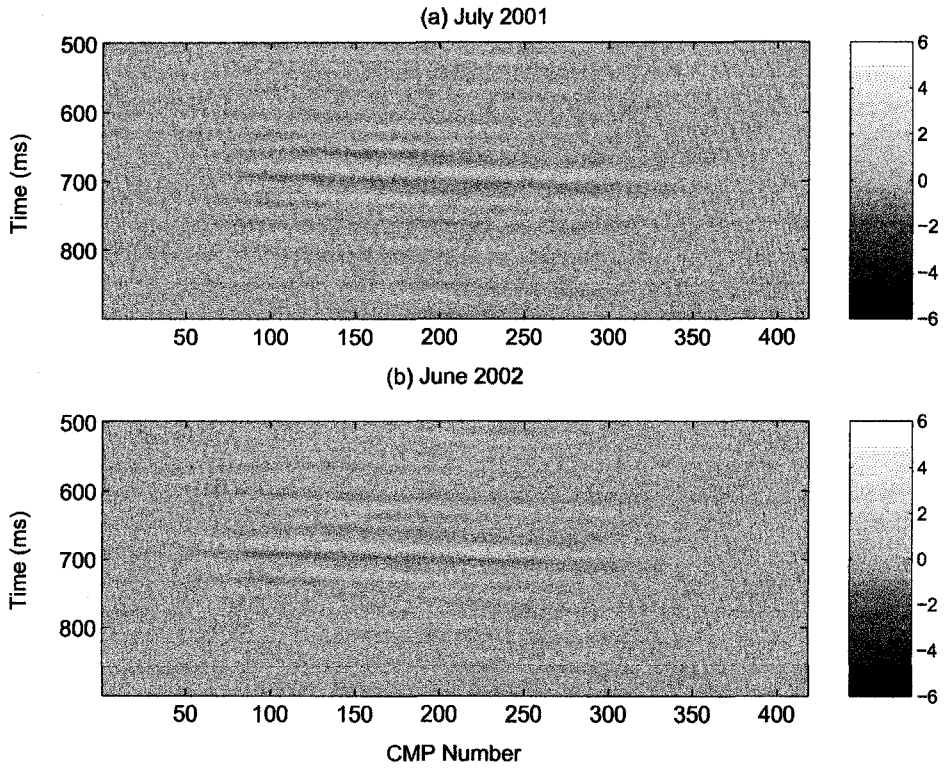

Figure 4.4: Time-lapse seismic profiles by using the PSP processing strategy.

monitoring. Examples of two such processed seismic sample profiles from the East Senlac site are shown in Figure 4.4.

4.2.2 Prestack parallel processing (PPP)

To reiterate, the central idea of PPP is that similar or identical processing flows are used in the time-lapse seismic processing. If slightly different parameters were used in the same processing flow or statistical operators were extracted separately, false images would be produced and manifested in the time-lapse seismic difference profile. Such a situation has occurred to the authors in their initial processing of these data; the reader is referred to *Zhang and Schmitt* (2003b) to see such an example of an incorrect interpretation of such data. This issue will be illustrated by the given two examples. In the first example, the

Table 4.1: Parameters used to estimate refraction statics.

Parameters	the 1^{st} set	the 2^{nd} set
Weathering velocity	800 m/s	
Replacement velocity	1750 m/s	
Datum	700 m	
Offset range	[110, 600] m	[140, 400] m
Time range	[120, 350] ms	[100, 300] ms

same seismic survey will be used as the hypothetical time-lapse seismic surveys with the zero calendar time interval. Identical processing parameters and identical processing flows will be used in the processing except that the two set of slightly different parameters will be used in the refraction static corrections. In the second example, refraction static operators will be extracted separately from the two different time-lapse seismic surveys. The details of these two examples will be described in the following sections.

Example 1: Inconsistent parameters used to estimate refraction statics

In this example, two different set of parameters, offset range and time range, are selected in the estimation of refraction statics. The selected parameters are listed in Table 4.1. Now apply these two set of parameters to process the same seismic survey. The estimated refraction statics at the shot positions and at the geophone positions are shown in Figure 4.5(a) and (b). The solid line represents the refraction statics by using the first set of parameters and the dashed line represents the refraction statics by using the second set of parameters. It is found that up to 4 ms deviation exists between these two refraction statics.

Apply these two set of static corrections to the same seismic survey, the processed post-stack seismic profiles are shown in Figure 4.6(a) and (b). The *only* difference between these two seismic profiles is that two different set of refraction statics are used in the time-lapse seismic data processing. The calculated difference profile is shown in Figure 4.6(c), from which significant residual variations can be found. The observed residual variations are in the same level as the post-stack seismic signals. Since these two seismic profiles shown in 4.6(a) and 4.6(b) are processed from the same seismic survey, theoretically, there should be no physical variations that can be observed between these two seismic profiles. The only source to produce these residual variations shown in Figure

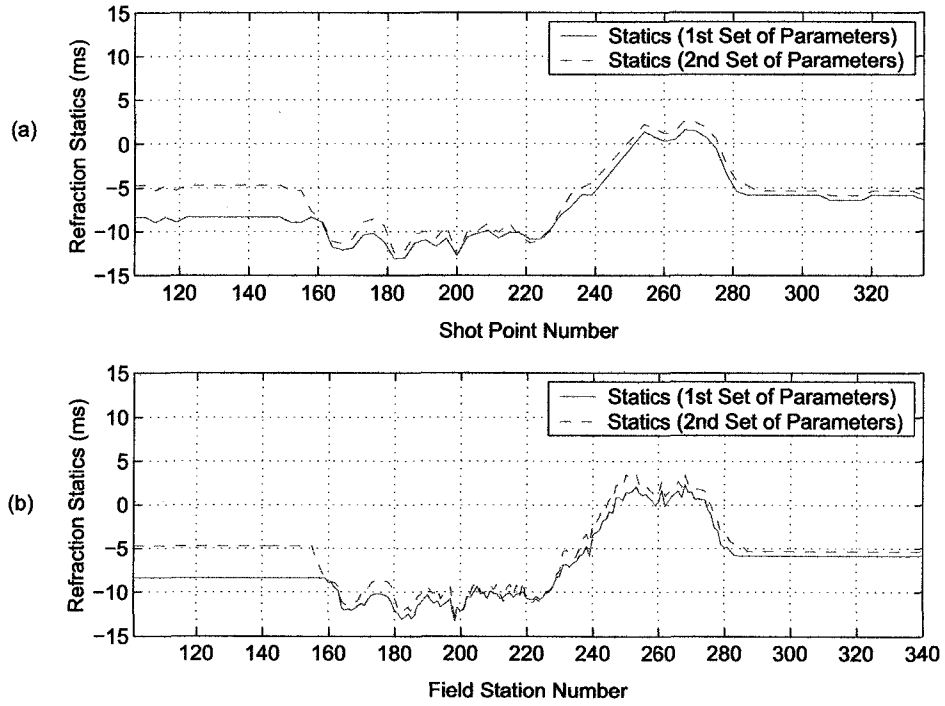

Figure 4.5: Refraction statics by using two different set of parameters. (a) Statics at the shot positions; (b) Statics at the geophone positions.

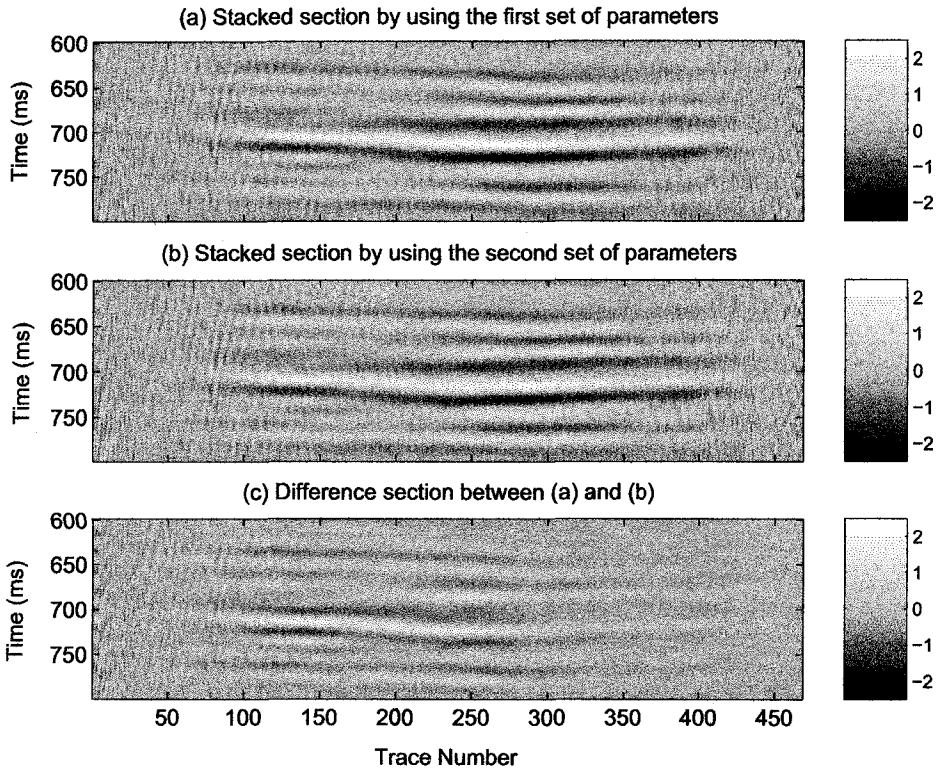

Figure 4.6: Post-stack seismic profiles and their difference producing an artificial time lapse anomaly.

4.6(c) is the use of two different set of refraction statics. In practice, such noise sensitive processing procedure must be avoided.

Example 2: Separately extracted refraction static operators

In the time-lapse seismic processing, some operators can only be determined statistically and they are usually data dependent. The extracted refraction static operator is one of them. It will be selected to illustrate this data dependent issue. First, two set of first-breaks are picked separately from the two selected time-lapse shot gathers. The two selected time-lapse shot gathers together with the picked first-breaks are shown in Figure 4.7(a) and (b). The selected shot gathers are located at the same position and with one year time interval. These two set of first-breaks are plotted in the same frame shown in Figure 4.8(a). They are found to overlay each other. The deviations between these

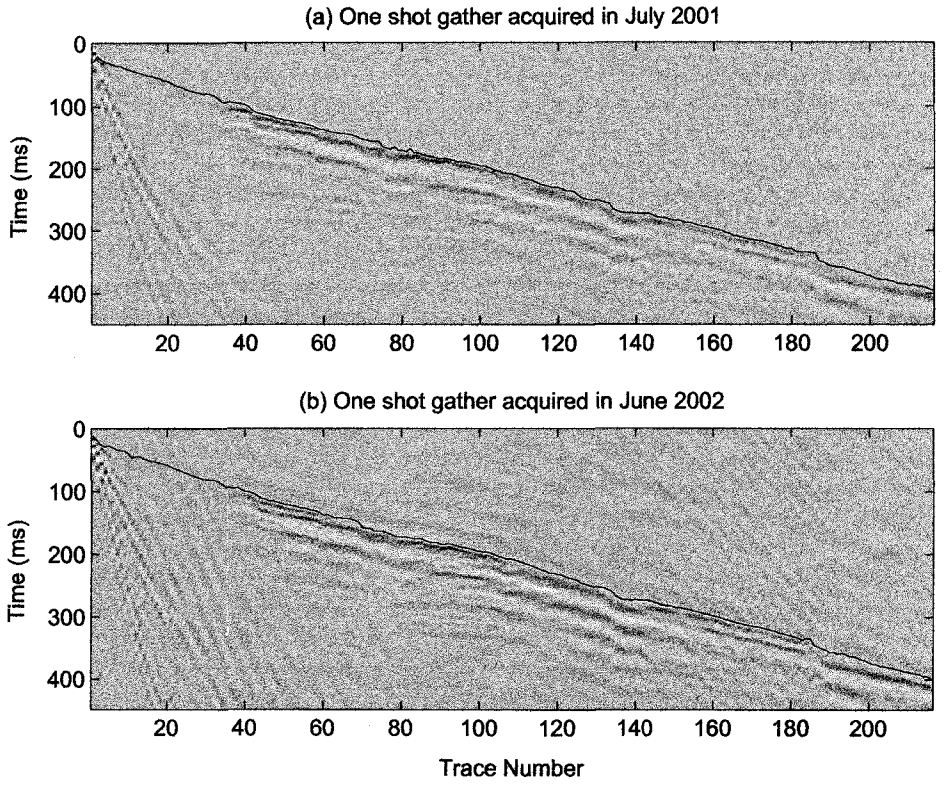

Figure 4.7: Two time-lapse shot gathers and the picked first-breaks (black line).

two curves can barely be observed. However, when the difference between these two set of first-breaks is plotted as shown in Figure 4.8(b), a significant up to -18ms first-break deviation is found at the initial offset and as high as +10 ms deviation is observed at the far offset. Since the picked first-breaks change with time-lapse seismic shot gathers, the picked first-breaks are therefore data dependent. Two factors, non-repeatability and human errors, are the direct reasons. Since non-repeatability is inherent in the acquired seismic data, it can not be completely removed at the seismic data acquisition stage. Therefore, efforts should be made to reduce human induced errors as much as possible.

The question is when these separately picked first-breaks are applied to process time-lapse seismic data, how big an effect they will have on the estimated refraction statics

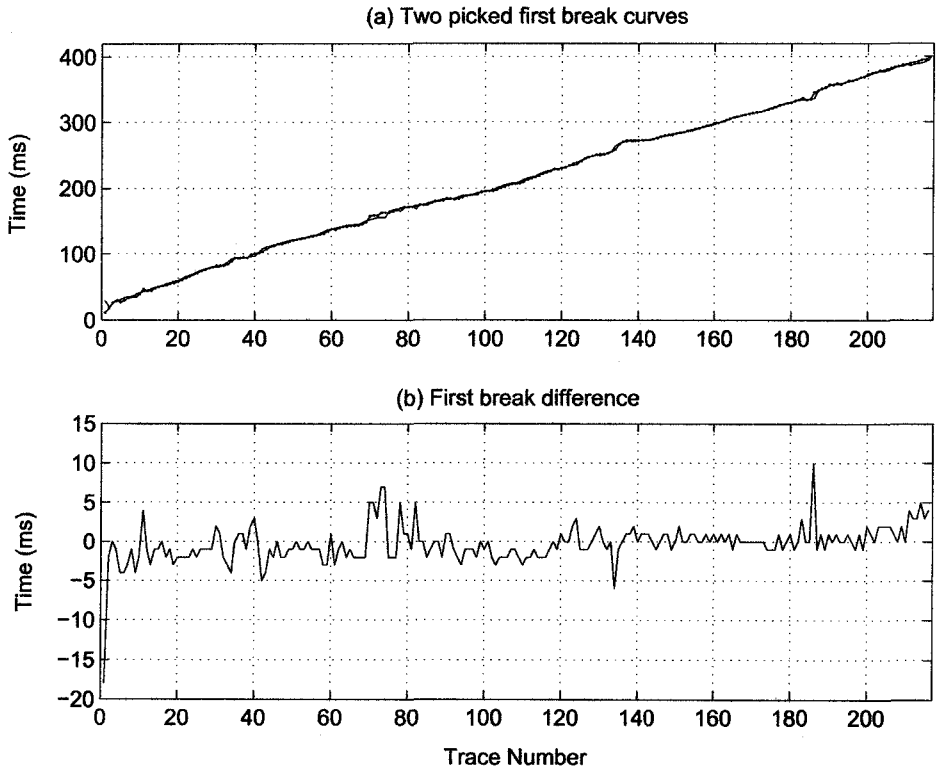

Figure 4.8: The two sets of first-breaks (upper panel) and their difference (lower panel).

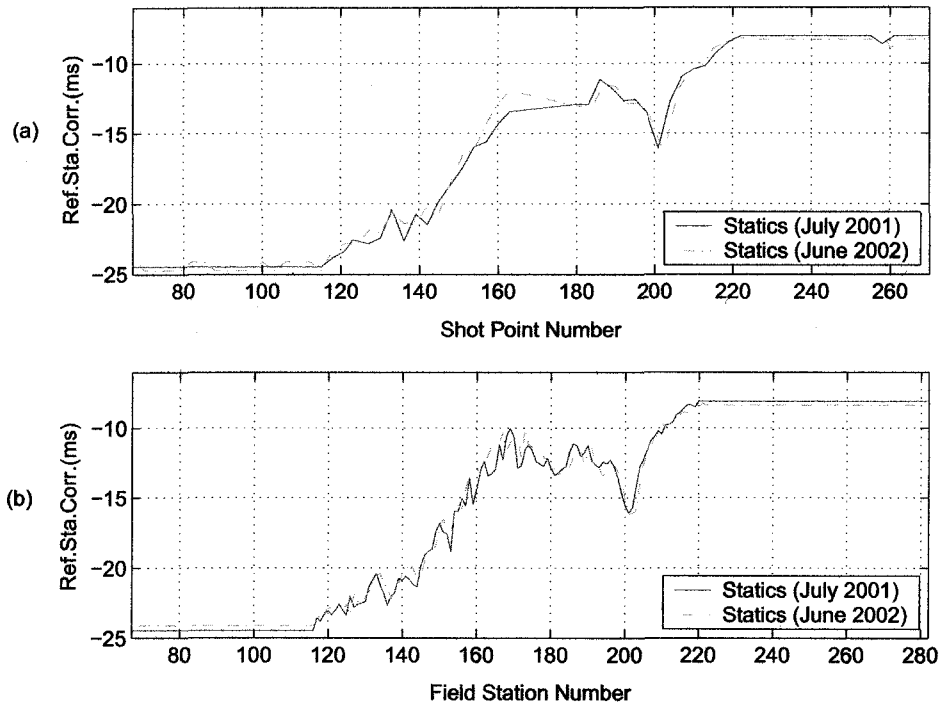

Figure 4.9: The two set of time-lapse refraction statics. (a) At the shot positions; (b) At the geophone positions.

and how large the artifacts will be produced on the post-stack seismic profiles. In order to examine these issues, two set of first-breaks are separately picked from the two time-lapse seismic surveys. The estimated refraction statics at the shot positions and at the geophone positions are shown in Figure 4.9(a) and (b). There are small and unsystematic deviations between these two set of refraction statics that are found at both shot and geophone positions. The processed post-stack seismic profiles by using these two set of refraction static operators are shown in Figure 4.10(a) and (b).

4.2.3 Comparison of the PPP and the PSP

The two processing strategies, PPP and PSP, are usually employed to process the seismic surveys which are designed for the purpose of time-lapse seismic monitoring. In the above illustrated PPP processing examples, it was found that strong artifacts are pro-

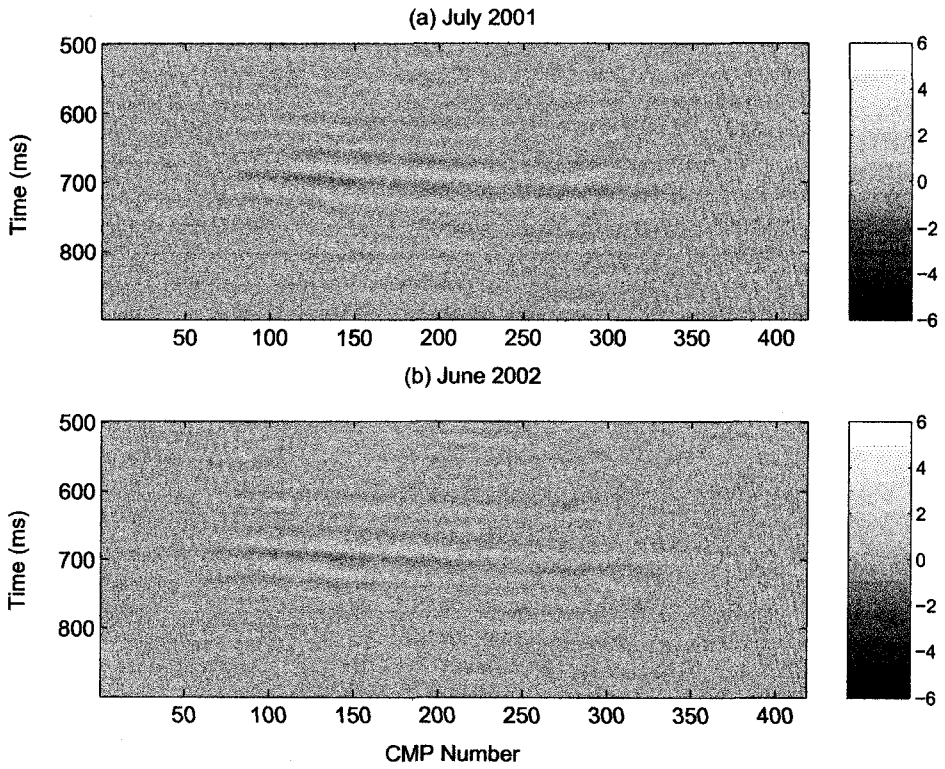

Figure 4.10: The time-lapse post-stack seismic profiles by using the PPP processing strategy.

duced when two different set of parameters are selected to process the two hypothetical time-lapse seismic surveys with the zero calendar time interval. Therefore, choosing consistent parameters is important in PPP processing.

Meanwhile, there are some differences between the post-stack seismic profiles by using the jointly extracted operators in the PSP and by using the separately extracted operators in the PPP. However, it must be noted that the changes seen are extremely small in this case. The quality of processed seismic profiles by using these two processing strategies can be compared as shown in Figure 4.11(a) and (b). Slight difference between these two frames, for example, within the illustrated arrow positions, can be observed. In frame 4.11(a), the seismic event is discontinuous while seismic event in frame 4.11(b) is laterally coherent. Obviously, this seismic difference may result in different interpretation on how rock properties change within the reservoir area. Generally, optimal results can be obtained by employing the PSP processing strategy.

4.3 The art of time-lapse seismic data processing: part 2 - XEQ

4.3.1 Introduction

Cross-equalization is applied in time lapse surveys to eliminate the non-repeatability and unappropriate processing caused variations. Generally, four optional operations can be included in the cross-equalization (XEQ) (*Ross et al.*, 1996),

- Spatial and temporal realignment;
- Energy balancing;
- Bandwidth equalization;
- Phase correction.

The first operation is usually required to regrid or to resample the time-lapse seismic surveys to the common grid size or to the common sample rate when the acquisition geometry or the sample rate between the seismic surveys are different. This resampling is often called the "registration" problem. The second operation is usually required when the energy distributed within the static geology area is different between the seismic

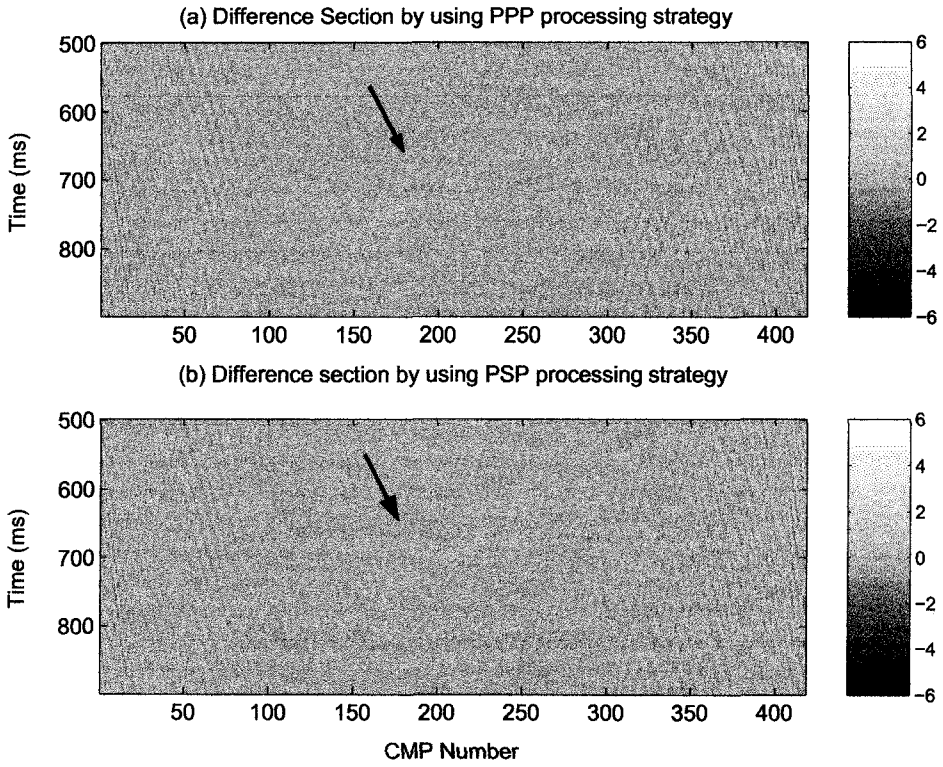

Figure 4.11: The two seismic difference profiles by using PPP using data from Figure 4.10 and PSP (using data from Figure 4.4) processing strategies. The arrow in the upper panel indicates discontinuous event; the arrow in the lower panel demonstrate continuous event.

surveys. The third and the fourth elements are used to calibrate the phase and frequency differences existing between the seismic surveys.

Two major steps can be included in the XEQ. The first step is to extract representative operators within the designed training window area. The second step is to apply the extracted operators to the zone of interest. Two inherent assumptions are usually involved in XEQ. The first assumption is that within the selected training time window, there should be no physical variations. The second assumption is that the non-repeatability caused variations within training window area should be the same as those within the zone of interest area. Theoretically, the operators extracted from the training window area should contain the same non-repeatability caused variations which should be eliminated when such extracted operators are applied to the interest area. Ideally, only physical variations can be detected. However, in the field time-lapse seismic monitoring, the non-repeatability caused seismic variations change with time. Therefore, even after XEQ, artifacts still and will always exist between the seismic surveys, especially when the time-lapse seismic surveys are acquired with different geometry, different source signals, or different acquisition equipment.

The previously mentioned Matched Filtering Method (MFM) and Bandwidth-Phase Equalization Method (BPEM) are methods commonly employed in XEQ (*Rickett*, 1997). The basic principles of these two methods will be described in the following sections.

4.3.2 The first XEQ method - matched filtering method in time domain (MFM)

The MFM (*Claerbout*, 1991) can simultaneously correct bandwidth differences and phase disparities between the seismic surveys in time domain and is intended to minimize the differences in the subsequent seismic traces. The time window in which the shaping filter A is developed needs to coincide with the times of reflections above the reservoir, i.e. with time that should not be influenced by variations in the reservoir itself. The residual between two seismic traces can be written in a matrix form:

$$D = AD_1 - D_2 \tag{4.1}$$

where A is the shaping filter to be found, D_1 is the monitor survey, and D_2 is the reference survey. The shaping filter A can be estimated by minimizing the above residual by using

the least-squares within the static geology zone. The derived shaping filter A can be written as,

$$A = (D_1^T D_1)^{-1} D_1^T D_2 \tag{4.2}$$

Once the shaping filter A is estimated, it can be applied to the monitor trace within the interest area. Theoretically, after this XEQ, the monitor survey is comparable to the reference survey.

4.3.3 The second XEQ method - bandwidth and phase equalization method in frequency domain (BPEM)

BPEM is carried out in the frequency domain. Usually, the survey with higher resolution is used to match the other survey with lower resolution. Otherwise, noise will be amplified when bandwidth of the lower resolution survey is raised to match the higher resolution survey (*Rickett*, 1997). The basic principle of BPEM is based on the method proposed by *Rickett* (1997) with minor modifications. In the modified version developed here, the operators are estimated trace by trace rather than from the whole seismic survey.

Referring to Figure 4.12, let $s_1(x,t)$ and $\tilde{S}_1(x,\omega)$ represent the reference seismic trace in the time domain and its transformed spectrum in the frequency domain. The monitor seismic trace consists of two parts. The first part is the portion of the seismic data from the static geology represented by $s_{2-1}(x,t)$. The second part is the seismic data within the interest area before and after cross-equalization represented by $s_{2-2}(x,t)$ and $s'_{2-2}(x,t)$. The $\tilde{S}_{2-1}(x,\omega)$, $\tilde{S}_{2-2}(x,\omega)$, and $\tilde{S}'_{2-2}(x,\omega)$ are the corresponding transformed spectra in frequency domain of these windows. Within the static geology window area, the amplitude spectrum ratio between the reference trace and the monitor trace can be written as,

$$B(x,\omega) = |\tilde{S}_1(x,\omega)|/(|\tilde{S}_{2-1}(x,\omega)| + \varepsilon) \tag{4.3}$$

where the parameter ε in the denominator is used to prevent instability in the case that $\tilde{S}_{2-1}(x,\omega)$ is equal to zero. In practice, it can be set to a small value.

Within the same static geology window area, the phase spectrum difference can be written as,

$$\Phi(x,\omega) = \arg(\tilde{S}_1(x,\omega)) - \arg(\tilde{S}_{2-1}(x,\omega)) \tag{4.4}$$

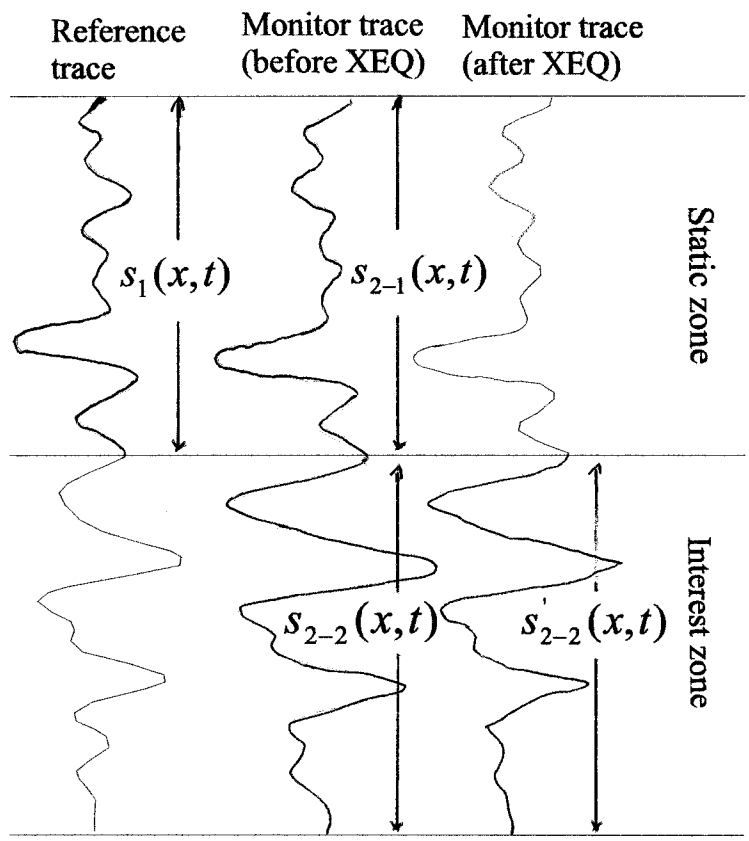

Figure 4.12: Illustration of basic principle of Bandwidth Phase Equalization Method (BPEM).

Apply the above extracted amplitude scaling factor $B(x,\omega)$ and phase difference $\Phi(x,\omega)$ to the zone of interest and the corrected monitor trace spectrum becomes,

$$\tilde{S}'_{2-2}(x,\omega) = B(x,\omega)\tilde{S}_{2-2}e^{-i\Phi(x,\omega)} \tag{4.5}$$

After this correction, the $\tilde{S}'_{2-2}(x,\omega)$ can be transformed back into time domain to obtain the cross-equalized monitor seismic trace.

4.3.4 Discussion on the application of MFM and BPEM

In XEQ, two issues will be addressed in this section by the application of MFM and BPEM. The first issue is whether the non-repeatability caused variations can be com-

pletely removed within the static geology window area. The second issue is whether the non-repeatability caused variations are the same within different window areas.

Let's look at the first issue. It will be investigated through illustrated examples. The central idea is that within the selected static window area, an operator which should contain information about the non-repeatability caused variations is extracted from the reference trace and the monitor trace. Then within the same window area, the extracted operator is applied to cross-equalize the monitor trace. The result by the application of MFM is shown in Figure 4.13. Residual variations are found to exist between the reference trace and the cross-equalized monitor trace. The result by the application of BPEM is shown in Figure 4.14. The cross-equalized monitor trace is found to be perfectly matched to the reference trace. Therefore, the non-repeatability variations within the training window area can be eliminated by employing the BPEM.

Next, the second issue will be examined. It will be investigated through the application of of the BPEM by extracting operators within different time window, since the extracted operator contains the non-repeatability caused variations within the designed window area. The reference trace and the monitor trace within the window [1, 64] ms and [65, 128] ms shown in Figure 4.14 will be used as input data to develop the cross-equalization filter. Within these two windows within which physical variations are not expected, two operators are estimated. The extracted set of spectrum operators are shown in Figure 4.15(a), 4.15(b), and the transformed operators in time domain are shown in Figure 4.15(c). Clearly, there are significant difference between these two extracted operators. This difference has reflected the existence of different non-repeatability caused variations within the two static geology zones.

It is known from the above demonstrated example that physical variations are not expected. The estimated operators essentially represent the inherent information about the difference between the reference trace and monitor trace. If the estimated operators from different window area are not the same, the existing differences between the reference trace and monitor trace are also different for these two different windows. In other words, time lapse variation changes with the selected windows and are functions of the window area. Therefore, we can say that these variations are caused by the non-repeatability which is inherent in the different stages of seismic data acquisition. This

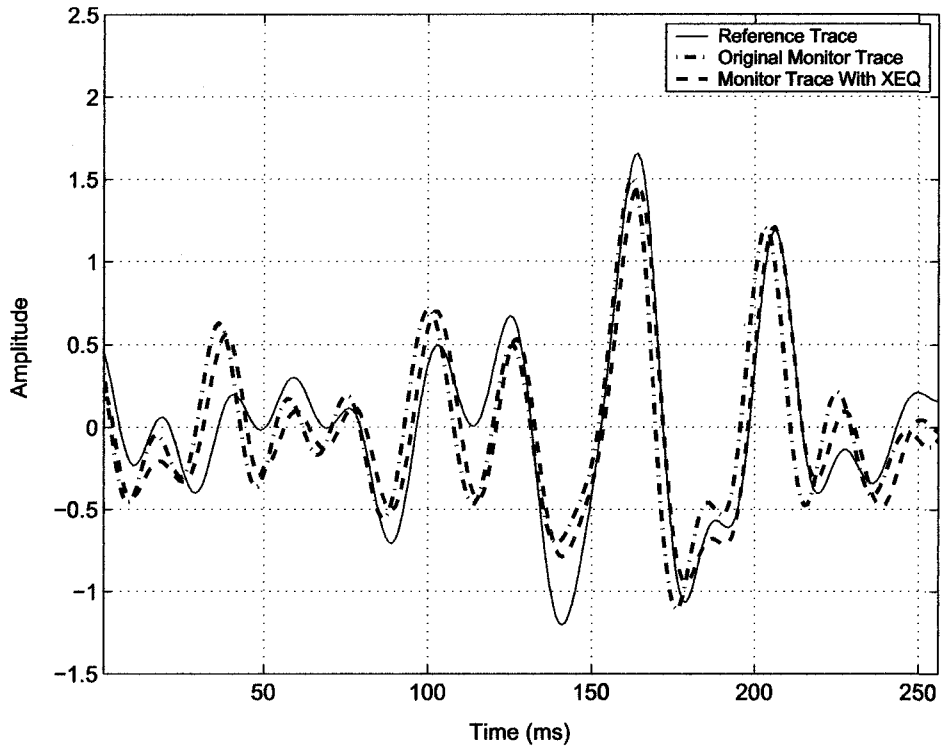

Figure 4.13: The XEQ test by using the MFM. The selected training window is [0, 256]ms; the same window is used to carry out XEQ.

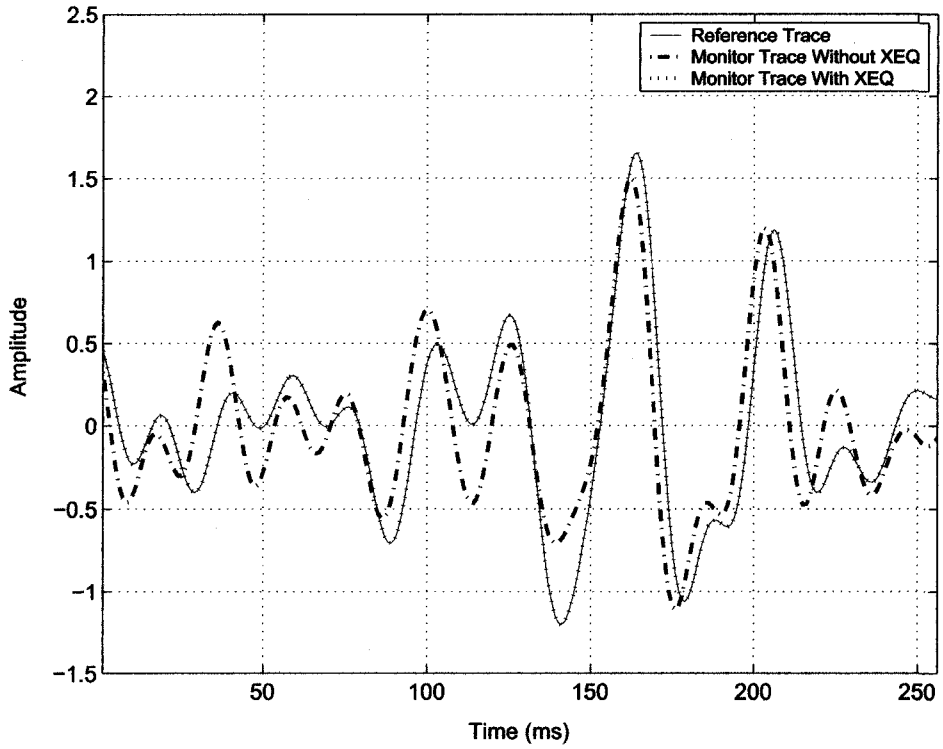

Figure 4.14: The XEQ test by using the BPEM. The reference trace and monitor trace follow the same curve.

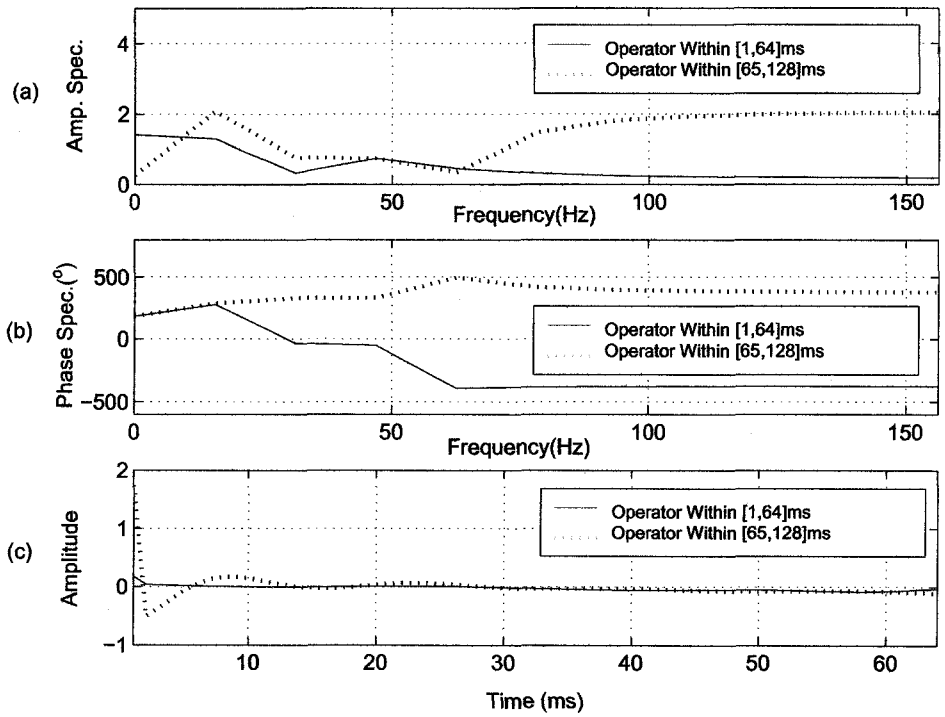

Figure 4.15: Operators estimated within the window $1 \sim 64$ ms and $65 \sim 128$ ms. (a) The estimated amplitude spectrum operators; (b) The estimated phase spectrum operators; (c) The transformed operators in the time domain.

will significantly limit the BPEM application to cross-equalize the calendar seismic data.

4.3.5 The strategies to cross-equalize East Senlac seismic surveys

The time-lapse seismic surveys acquired in the East Senlac area were designed with data repeatability in mind as will be discussed in detail in the next chapter. Therefore, the elements involved in XEQ, such as spatial and temporal resampling, bandwidth and phase corrections, can be omitted and the XEQ becomes relatively simple. Only the two elements, energy balancing and time shifting, are required. As an illustration, a set of normalized time-lapse seismic traces are selected. The selected traces are located at the same CMP position. The trace acquired in July 2001 is selected as the reference trace and all the other traces are used as the monitor traces. The selected original traces and the cross-equalized traces are shown in Figure 4.16(a) and (b). Clearly, the wave shapes of the cross-equalized traces shown in Figure 4.16(b) have been improved and they are now more consistent.

4.4 Summary

When the seismic surveys are acquired for the purpose of time-lapse seismic monitoring, the PPP and PSP are usually employed in the processing. The PPP emphasizes the use of similar or identical processing flows. The PSP, in addition to the features inherent in PPP, emphasizes the use of the extracted operators jointly or simultaneously to the multi-vintage surveys. Usually, optimal results can be obtained by using the PSP.

In XEQ, the MFM and BPEM are commonly used to calibrate the non-repeatability caused variations. There are two inherent assumptions. The first assumption is that the same non-repeatability caused variations should exist between the time-lapse seismic surveys within the static geology area. The second assumption is that the non-repeatability caused variations should be the same within the static geology zone and the zone of interest area. However, these two assumptions are impossible to satisfy in the field time-lapse seismic monitoring. Therefore, in the application of the MFM and BPEM, artifacts will be produced within the zone of interest area.

For the East Senlac case, the PSP strategy is employed in the time-lapse seismic process-

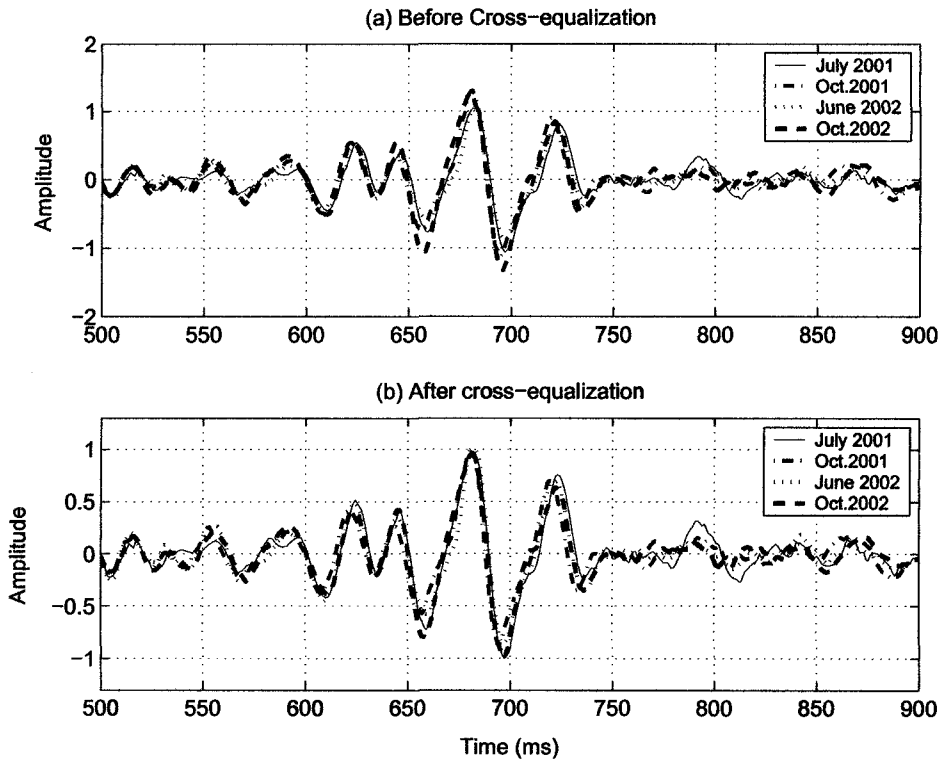

Figure 4.16: The time-lapse seismic traces before and after XEQ.

ing. Since the seismic surveys acquired in this area possess very high repeatability, only the two components, energy balancing and time shifting, are implemented in the XEQ.

Chapter 5

Seismic repeatability study

5.1 Introduction

Seismic repeatability is important in time-lapse seismic monitoring. A variety of factors are involved in the seismic repeatability study, such as the depth of buried detectors (e.g. *Moldoveanu et al.*, 1996), small variations in water table, tides, currents and temperature (e.g. *Bertrand and MacBeth*, 2003; *Vesnaver et al.*, 2003), ambient noise, transition zone, subsidence (e.g. *Lumley*, 2001), source and geophone positions (e.g. *Ebrom et al.*, 1997; *Curtis et al.*, 2002; *Kragh and Christie*, 2001; *Archer et al.*, 1999; *Morice et al.*, 2000; *Landro*, 1999a), source signatures (e.g. *Eiken et al.*, 2002; *Laws and Kragh*, 2000), geometry design (e.g. *Hughes*, 2000; *Whitcombe et al.*, 2001; *Thompson and Najjar*, 2002), and CMP stack fold distribution (e.g. *Rennie et al.*, 1997; *Porter-Hirsche and Hirsche*, 1998). Some of the non-repeatability problems can be overcome by the careful deployment of source and receiver positions while other problems, such as those caused by annual near surface variations, are difficult to solve at the acquisition stage and usually can only be ameliorated in the subsequent processing stage. A good deal of literature on time-lapse surveying deals with the issues of registration between older and more modern vintage data. This registration process itself can add substantial uncertainty.

In the first part of this chapter, the repeatability of source and geophone positions will be examined. In the second part, repeatability on the recorded source signals will be investigated in detail. In the third part, three metrics including Pearson correlation (PEAR), normalized root-mean-square (NRMS), and predictability (PRED) will be described, compared, and applied to quantify the repeatability of post-stack seismic data.

Meanwhile, the factors which directly affect seismic repeatability will be investigated. Eight 2-D time-lapse seismic surveys along the W-E and the N-S directions in East Senlac area will be used in this repeatability study.

5.2 The calendar seismic data acquisition

Two seismic profile lines are set up along different directions shown in Figure 5.1. The seismic sample rate was 1ms. One of the receiver lines ran west to east (W-E) direction with 240 channels, and the other receiver line runs north to south (N-S) direction with 216 channels. Together with these two setups, the shot lines were shot parallel to the geophone lines for the reflection surveys. During the process of seismic data acquisition, the geophones were covered with soil to attenuate noise. The buried receiver positions can be easily located for the subsequent shooting. All receivers and shot locations continue to be surveyed with a differential GPS instrument. The same base crew and equipment (Figure 5.2(a), 5.2(b), 5.2(c)) have allowed for a high degree of repeatability in both the source and receiver positions. The details of the acquisition parameters are listed in Table 5.1.

5.3 Repeatability study in source and receiver positions

The relative shot and receiver positions along the W-E and N-S directions are shown in Figure 5.3(a) and 5.3(b). Along the N-S direction (5.3(a)), the observed deviations in geophone positions are small, and the actual errors are in the order of centimeters. Similar observations can be made on shot positions. The maximum deviation is less than 3 meters. The repeatability in geophone positions is better than in source positions because the geophone positions are more easily located once they are setup. Along the W-E direction seismic line, similar features on shot and geophone positions shown in Figure 5.3(b) can be observed. The illustrated high repeatability in source and geophone positions is important in the improvement of seismic repeatability and in the reduction of non-repeatability caused variations.

Table 5.1: The East Senlac seismic data acquisition parameters.

Date	Source	Number of Channels	Recorder	Source Spacing (m)	Receiver Spacing (m)	Lines
July, 2001	minivibe (12-150Hz) 15 sec sweep	240	GEODE	9	3	East West Reflection Line
July, 2001	- - -	216	-	-	-	North South Reflection Line
October, 2001	- - -	240	-	-	-	East West Reflection Line
October, 2001	- - -	216	-	-	-	North South Reflection Line
June, 2002	- - -	240	-	-	-	East West Reflection Line
June, 2002	- (12-120Hz) -	216	-	-	-	North South Reflection Line
October, 2002	- - -	240	-	-	-	East West Reflection Line
October, 2002	- - -	216	-	-	-	North South Reflection Line

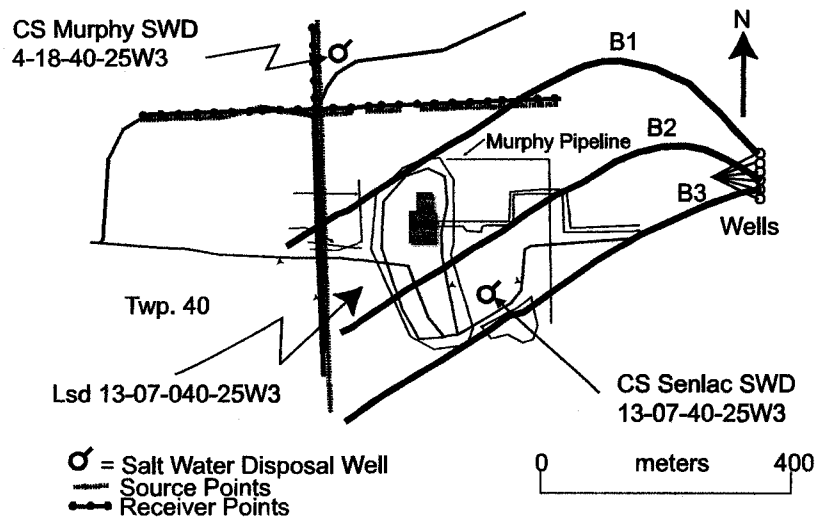

Figure 5.1: Map of the Senlac plant showing the relative location of the horizontal wells (thick solid lines), the two seismic profiles (blue and red lines), and the three wells (courtesy of *Theune* (2004)).

5.4 Repeatability in source signatures

During the process of data acquisition in East Senlac area, the source signals emitted are simultaneously recorded together with the reflection seismic data. Obtaining a deterministic source wavelet is very difficult. The source wavelet provided here is a measure of the average of two accelerometer sensors that are mounted at different locations on the vibrator mass and coupling plate. It comes from the autocorrelation of the response of the accelerometers during the process of sweeping and in the "Klauder" wavelet for each sweep. The University of Alberta IVI minivibe, a type of mechanical source, is used in this recording process. Repeatability on the recorded source signals will be investigated in the subsequent sections.

5.4.1 Repeatability of the recorded source signals along the N-S direction

There are four sets of time-lapse source signals recorded along the N-S direction. They are individually recorded in July 2001, October 2001, June 2002, and October 2002. These normalized source signals are plotted in a 3-D coordinate shown in Figure 5.4.

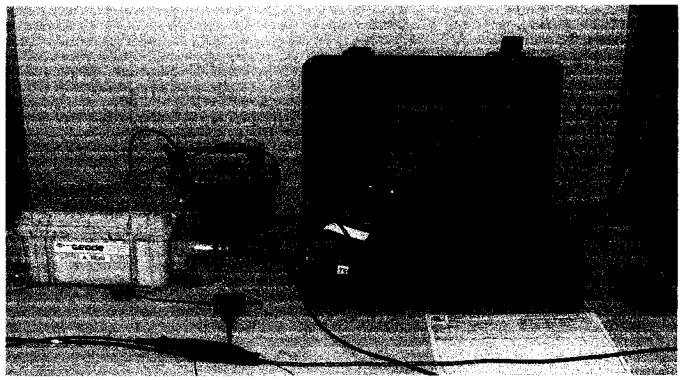

(a)

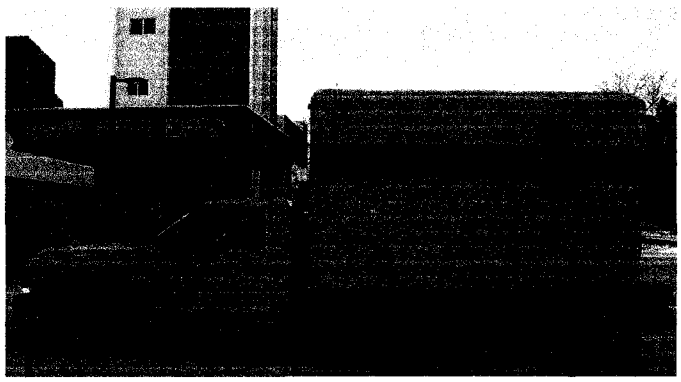

(b)

(c)

Figure 5.2: Acquisition equipment of geophone and minivibe. (a) Geophone and laptop which are used to record data; (b) Minivibe recording room; (c) Vibrator.

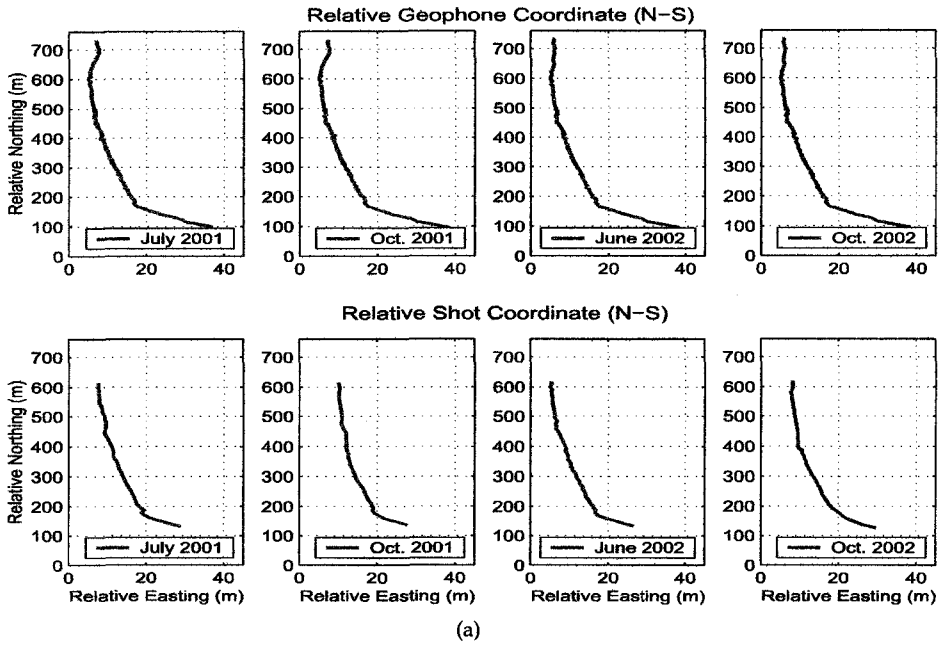

(a)

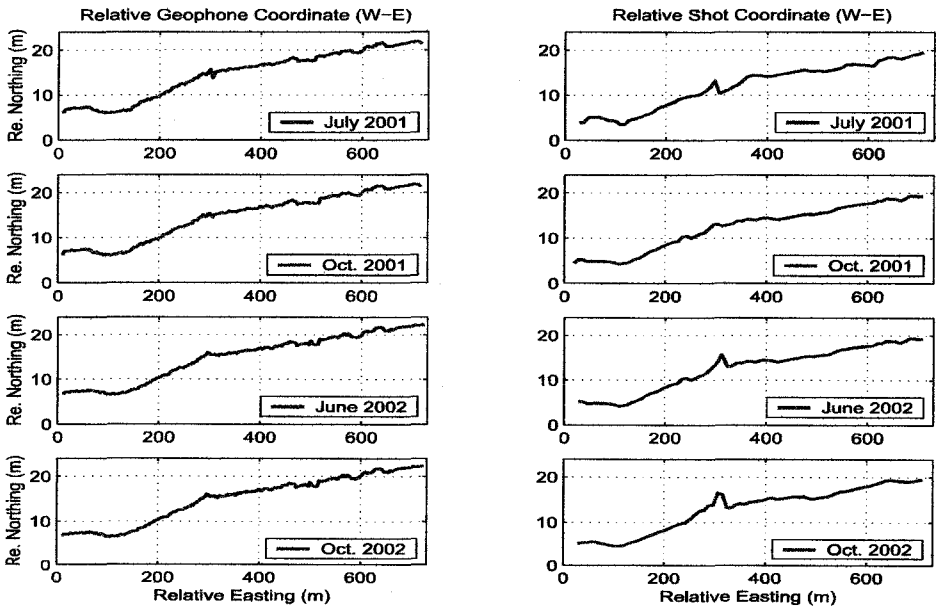

(b)

Figure 5.3: The relative shot and receiver coordinates. (a) Along the N-S direction seismic line; (b) Along the W-E direction seismic line.

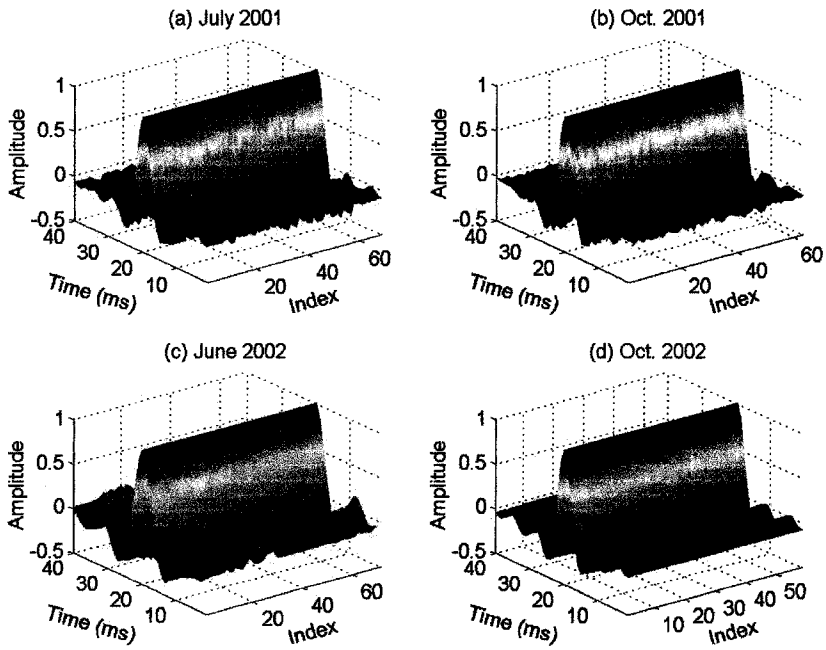

Figure 5.4: The recorded source signals along the N-S direction. Each panel displays all the source wavelets obtained during each of the monitor surveys with each shot location indicated along the index axis.

Because of the varying surface coupling conditions between the base plate of the vibrator and the soil surface, these recorded source signals change with time. They are unique and non-repeatable. The source signals, which here are derived from the averaged acceleration of the plate as detected by two accelerometer, recorded in October 2002 are found to have excellent repeatability. This is because the muddy surface has provided better coupling conditions and was indicated also by monitoring the four levels with time during the vibrator sweep. These staged flat for Oct. 2002 survey indicate good coupling throughout the entire sweep.

More interesting features can be observed by projecting these source signals into the polar coordinate system shown in Figure 5.5. Each angle represents one source signal. The radius represents the amplitude. Starting from the center, the amplitude increases outward until it reaches the maximum value of 1. If all the amplitudes having the same sample index have the same values and all the amplitudes are located on the round circles, the source signals would be considered completely repeatable. Therefore, it can be observed from figure 5.5 that except the amplitudes with the normalized maximum values, the remaining amplitudes with the same sample index are no longer located on the round circles, and deviations begin to exist. Similarly to the previous observations, the source signals recorded in October 2002 are found to have the best repeatability.

The repeatability of the seismic source may also be analyzed in the frequency domain. The transformed amplitude and phase spectra are shown in Figures 5.6 and 5.7 respectively. The color index shown in Figure 5.6 represents amplitude; the horizontal axis represents frequency, and the vertical axis represents the index number of source signals. The recorded source signals in July 2001, October 2001, and October 2002 are found to be distributed within the same frequency range 12~150 Hz while the remaining source signals recorded in June 2002 are distributed within the relatively narrower frequency range 12~110 Hz due to human recording error that was not immediately detected in the field. Similarly to the previous observations, the amplitude spectra from October 2002 are found to have the best repeatability. Repeatability for the remaining source signals decreases in the order from October 2001, July 2001, to June 2002. Similar features can also be found from the transformed phase spectra shown in Figure 5.7. More details can be observed from the selected calendar source signals and their transformed amplitude

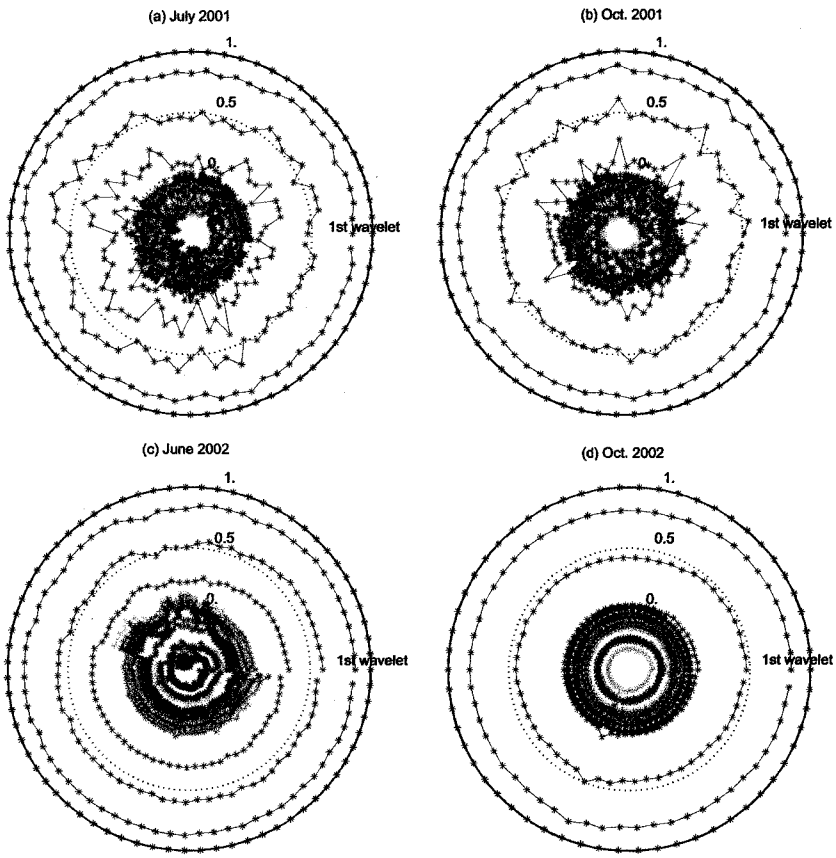

Figure 5.5: The source signals along the N-S direction are projected into the polar coordinate system.

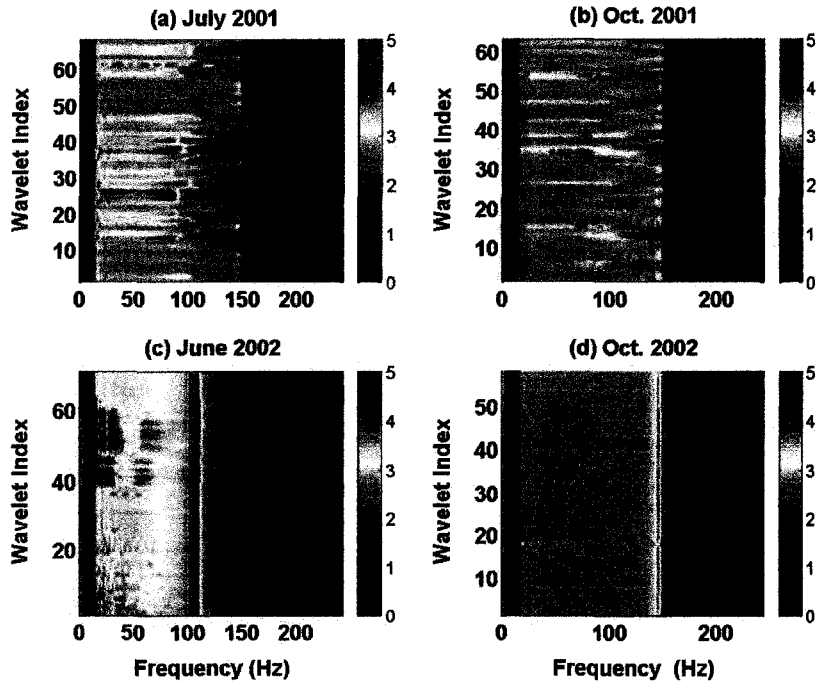

Figure 5.6: The transformed source amplitude spectra along the N-S direction.

and phase spectra. They are shown in Figure 5.8.

5.4.2 Repeatability of the recorded source signals along the W-E direction

Similarly to the previous signal analysis along the N-S direction, the recorded source signals along the W-E direction are presented in the 3-D coordinate system shown in Figure 5.9, projected in the polar coordinate system shown in Figure 5.10, and transformed in the frequency domain shown in Figure 5.11 and 5.12. The source signals recorded along the W-E direction are distributed within the same frequency range 12~150 Hz. The source signals recorded in October 2002 are found to have the best repeatability. This is mostly because of the conditions at the immediate surface with good coupling observed during wet conditions.

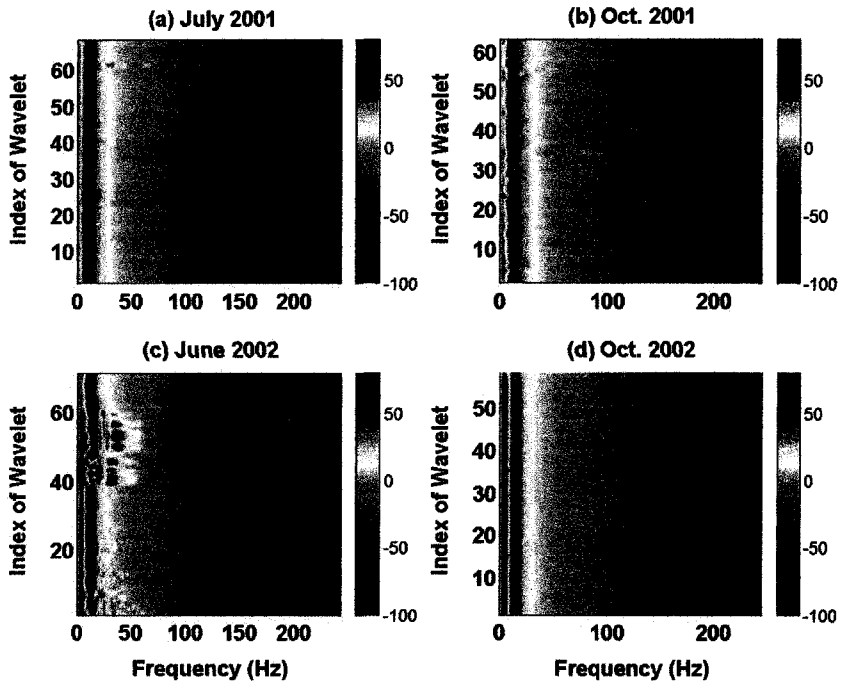

Figure 5.7: The transformed source phase spectra along the N-S direction in the unit of degree.

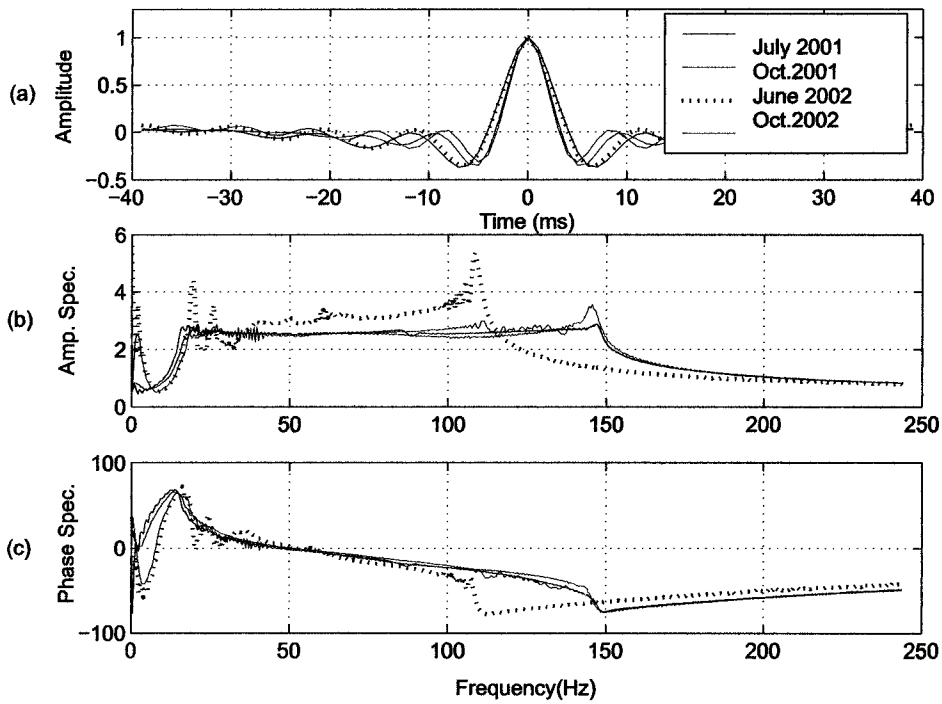

Figure 5.8: The time-lapse N-S source signals and the transformed spectra at receiver index number 106. (a) Source signals; (b) Amplitude spectra; (c) Phase spectra.

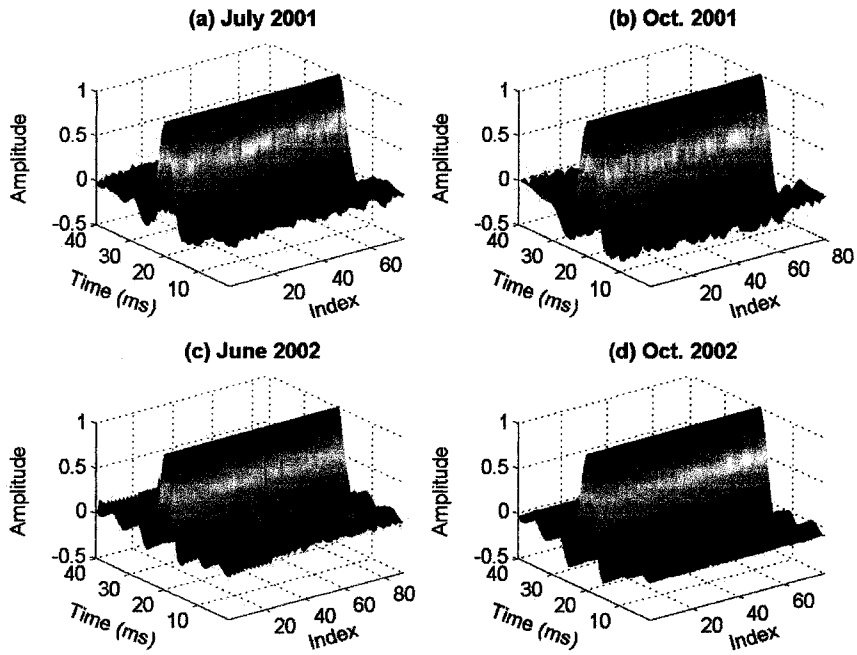

Figure 5.9: The source signals recorded along the W-E direction.

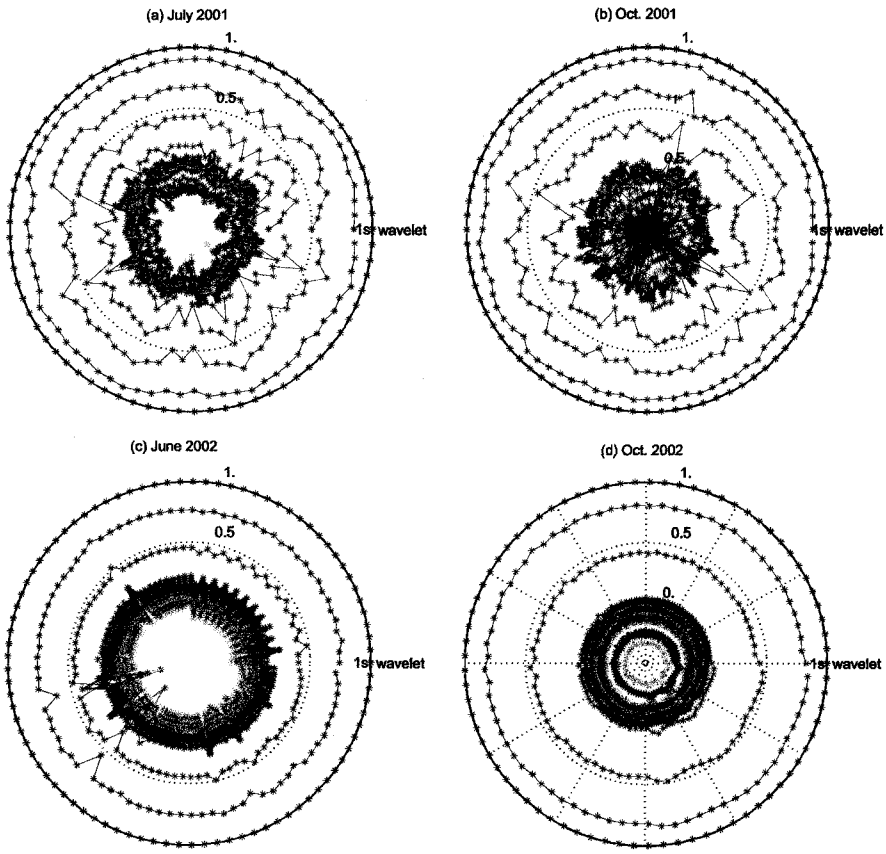

Figure 5.10: The source signals along the W-E direction are projected into the polar coordinate system.

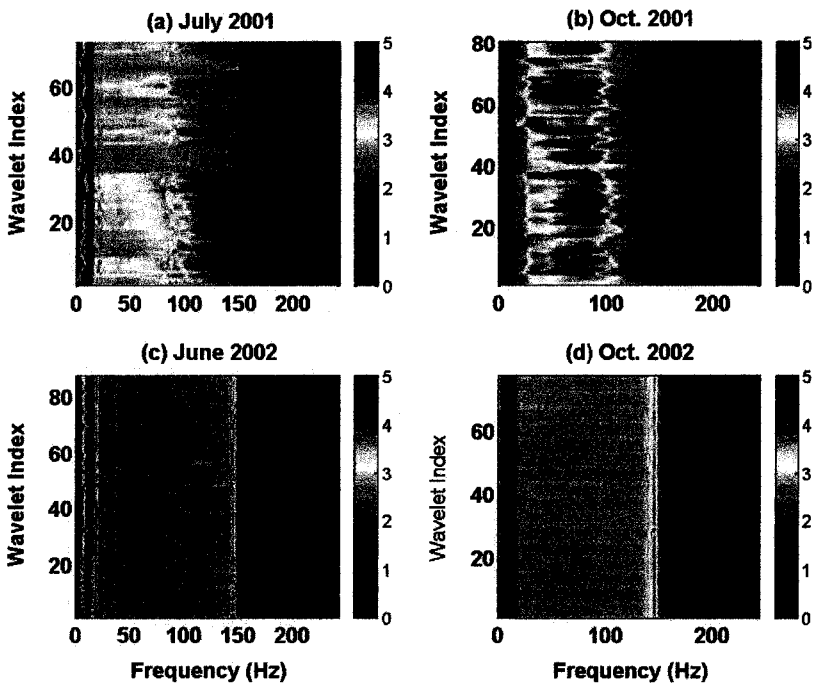

Figure 5.11: The transformed source amplitude spectra along the W-E direction.

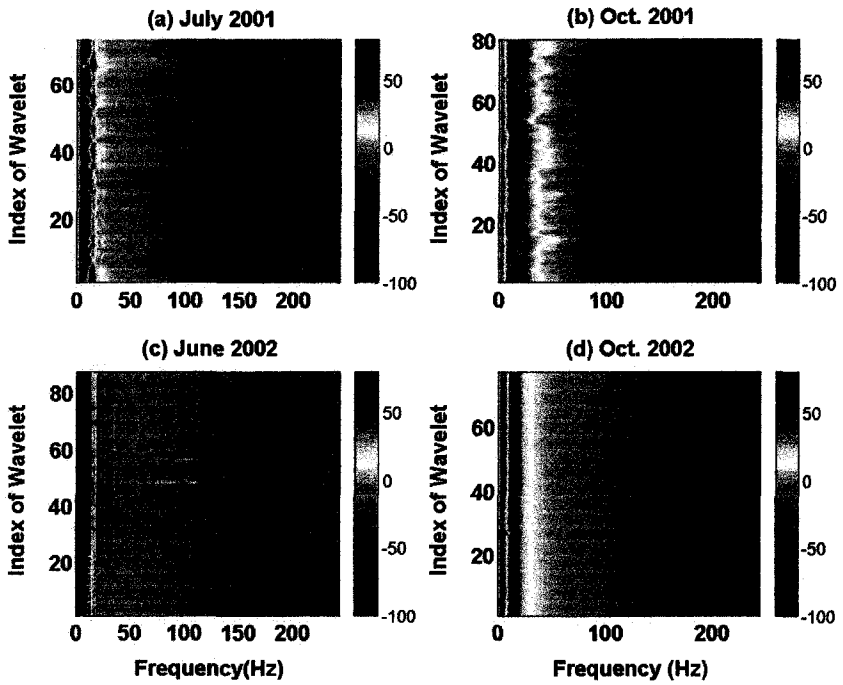

Figure 5.12: The transformed source phase spectra along the W-E direction in the unit of degree.

5.4.3 Discussion

As shown in the previous section, some recorded source signals have relatively narrower frequency range than the other source signals due to improper vibrator setup. In order to examine how this frequency difference will affect the reflection seismic signals, two calendar seismic shot gathers located at the same position are selected. The shot sequence number is 106. One shot gather is recorded in June 2002 with the source signal distributed within 12~110 Hz, and the other shot gather is recorded in October 2002 with the source signal distributed within 12~150 Hz. The average amplitude spectra are calculated within the reflection area with time window [640, 850] ms and trace range [145, 216]. The original shot gathers and the calculated amplitude spectra are shown in Figure 5.13. The amplitude spectra are found to be mainly distributed below 50 Hz. Within the 0~50 Hz, these two amplitude spectra have very similar shapes. Within the higher frequency range 60~120 Hz, the amplitude spectra show only small differences. This example demonstrates that the differences between these two source signals have small effect on the reflection seismic data within the low frequency range within which the main seismic energy is distributed.

5.5 Quantitative post-stack seismic repeatability study

"There does not appear to be a standard measure of repeatability, defined as a metric, to quantify the likeness of two traces" (*Kragh and Christie*, 2002). In order to appropriately quantify the post-stack seismic repeatability acquired in East Senlac area, three metrics including PEAR, NRMS, and PRED are selected in this investigation. First, the basic principles of these three metrics will be described. Then these metrics will be applied to quantify the East Senlac seismic repeatability along the W-E direction and the N-S direction.

5.5.1 Trace semblance metrics

PEAR

The PEAR is named after a famous statistician, Pearson. The PEAR is a well known statistical procedure that allows to assess the strength and direction of the relationship

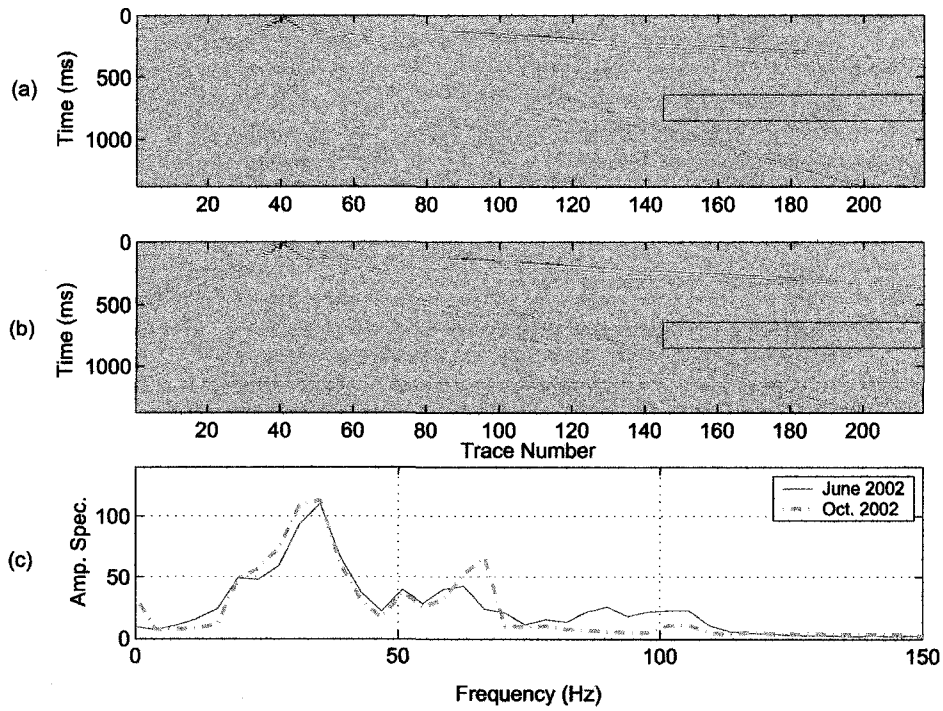

Figure 5.13: Two time-lapse seismic shot gathers and the calculated average amplitude spectra within the defined window area. (a) Shot 106 acquired in June 2002; (b) Shot 106 acquired in October 2002; (c) Average amplitude spectra.

between two phenomena. The reader is likely most familiar with this measure under another name of correlation coefficient judging the quality of a correlation between two phenomena. Here, it is used as a measure of the similarity between the value of a measurement and the corresponding true value. Let $\mathbf{a} = [a_1, a_2, ..., a_N]$ and $\mathbf{b} = [b_1, b_2, ..., b_N]$. The PEAR can be formulated as,

$$PEAR = \frac{\sum_{i=1}^{N} a_i b_i - \sum_{i=1}^{N} a_i \sum_{i=1}^{N} b_i}{\sqrt{(\sum_{i=1}^{N} a_i^2 - \frac{(\sum_{i=1}^{N} a_i)^2}{N})(\sum_{i=1}^{N} b_i^2 - \frac{(\sum_{i=1}^{N} b_i)^2}{N})}} \tag{5.1}$$

where **a** and **b** are the input data sets, and N is the window length. This value is limited within the range [-1, 1]. When $\mathbf{a} = \mathbf{b}$, the PEAR represents the autocorrelation coefficient; or else the PEAR represents cross-correlation coefficient. The value of $PEAR = \pm 1$ occurs the only when all the scattering points lie exactly on a straight line; i.e. they are perfectly linearly correlated.

The PEAR relies on determination of similarity between two seismic phenomena by using a standard statistical correlation test. In the calculation of PEAR, one seismic survey can be selected as reference survey and the remaining seismic surveys can be used as monitor surveys. If there were no change between the reference survey and the monitor survey, the calculated PEAR values within the designed window should be close to ± 1. If there were a significant change, the absolute PEAR value should be near zero. Therefore, mapping the PEAR values can provide a measure of repeatability comparison between the time-lapse seismic surveys. The PEAR measure is also insensitive to differences in the amplitude gain between the two traces and captures only differences in shape.

NRMS

NRMS is also called root mean squares (RMS) difference ratio (e.g. *Koster et al.*, 2000). The NRMS of two traces **a** and **b** within the designed time window is defined by the following formula,

$$NRMS = \frac{200\% * RMS(\mathbf{a} - \mathbf{b})}{RMS(\mathbf{a}) + RMS(\mathbf{b})} \tag{5.2}$$

where the RMS function is defined as the summation of squared samples **x** over the designed time window divided by the number of samples N,

$$RMS = \sqrt{\frac{\sum_{i=1}^{N} (x_i)^2}{N}} \tag{5.3}$$

The NRMS value is limited within the range [0, 200]%. The NRMS is very sensitive to the smallest change in the data (e.g. *Kragh and Christie*, 2002). Two identical traces yield 0% NRMS. Two anti-correlated traces or one zero and one non-zero trace equal 200% NRMS. Two traces containing random noise give 141% NRMS.

PRED

The PRED (*Kristiansen et al.*, 2000) is equivalent to the coherence of *White* (1980) (e.g. *Kragh and Christie*, 2002). The PRED of two traces **a** and **b** is defined within the defined time window with the lag τ (τ=[$\tau_1, \tau_2, ..., \tau_M$]). It can be expressed by the following formula,

$$PRED = \frac{\sum_{i=1}^{M} (\varphi_{\mathbf{ab}|_{t_1}^{t_2}}(\tau_i))^2}{\sum_{i=1}^{M} (\varphi_{\mathbf{aa}|_{t_1}^{t_2}}(\tau_i)\varphi_{\mathbf{bb}|_{t_1}^{t_2}}(\tau_i))} \tag{5.4}$$

where the $\varphi_{\mathbf{ab}}$ represents the cross-correlation of the two traces **a** and **b**, the $\varphi_{\mathbf{aa}}$ and $\varphi_{\mathbf{bb}}$ represent the autocorrelation of the trace **a** and **b**. The PRED is sensitive to noise. However, it is insensitive to the time shift and amplitude scalars. For example, one trace with half the amplitude of the other one, or anti-correlation traces, yield 100% PRED. The calculated PRED value changes with the correlation window and the number of lags within that window.

5.5.2 East Senlac quantified seismic repeatability study

PEAR

The PEAR values are calculated from the time-lapse post-stack seismic profiles acquired in East Senlac area. In this calculation, mapping the PEAR values is expected to provide a quality measurement and to provide a criteria for highlighting the regions that have undergone changes within the reservoir area.

The post-stack time-lapse seismic profiles along the W-E direction are shown in Figure 5.14 and the seismic difference profiles are shown in Figure 5.15 with the first acquired seismic survey as the reference survey. The post-stack seismic profiles and the difference profiles along the N-S direction are shown in Figure 5.16 and 5.17.

The calculated PEAR profiles are shown in Figure 5.18(a) and 5.18(b). The calculated values with higher S/N ratio are mainly distributed within the range 0.85~1. The se-

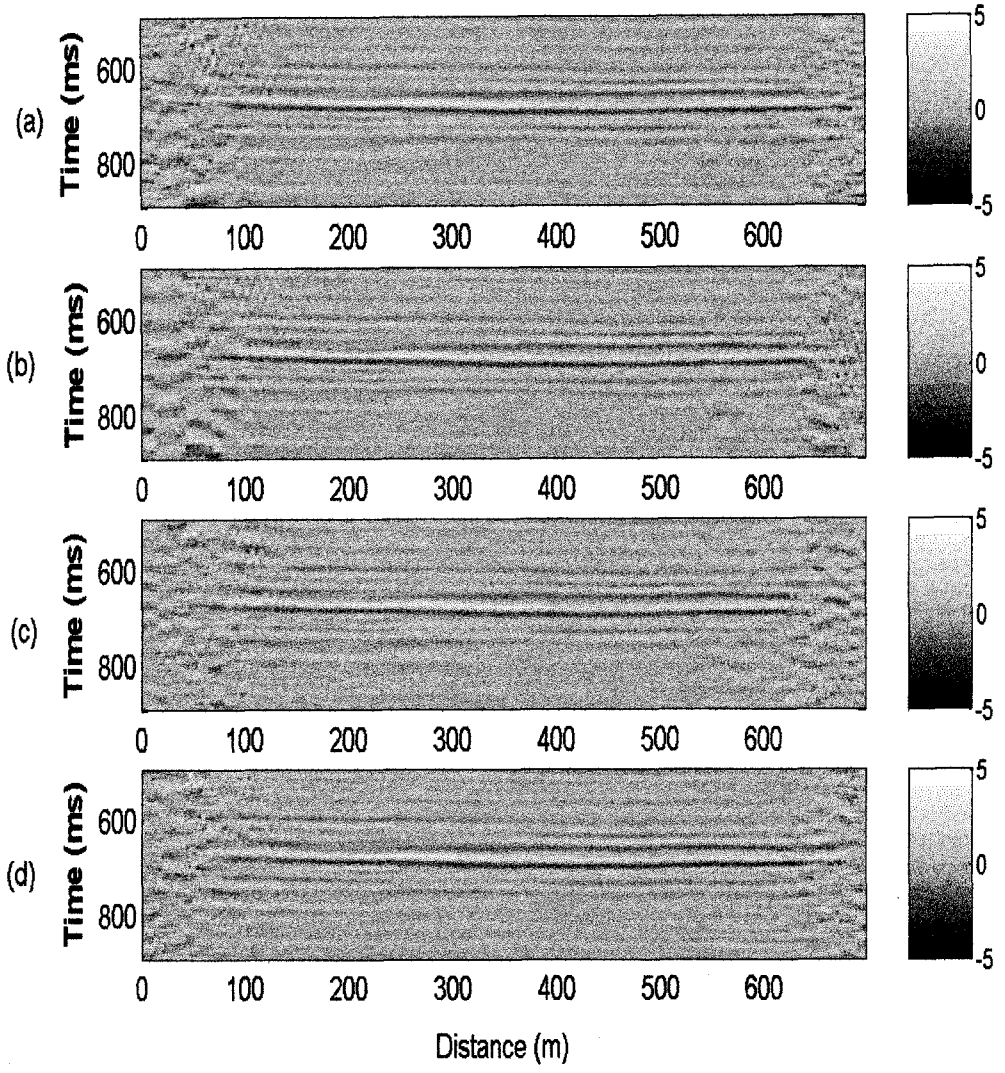

Figure 5.14: Time-lapse seismic profiles along the W-E direction. (a) July 2001; (b) October 2001; (c) June 2002; (d) October 2002.

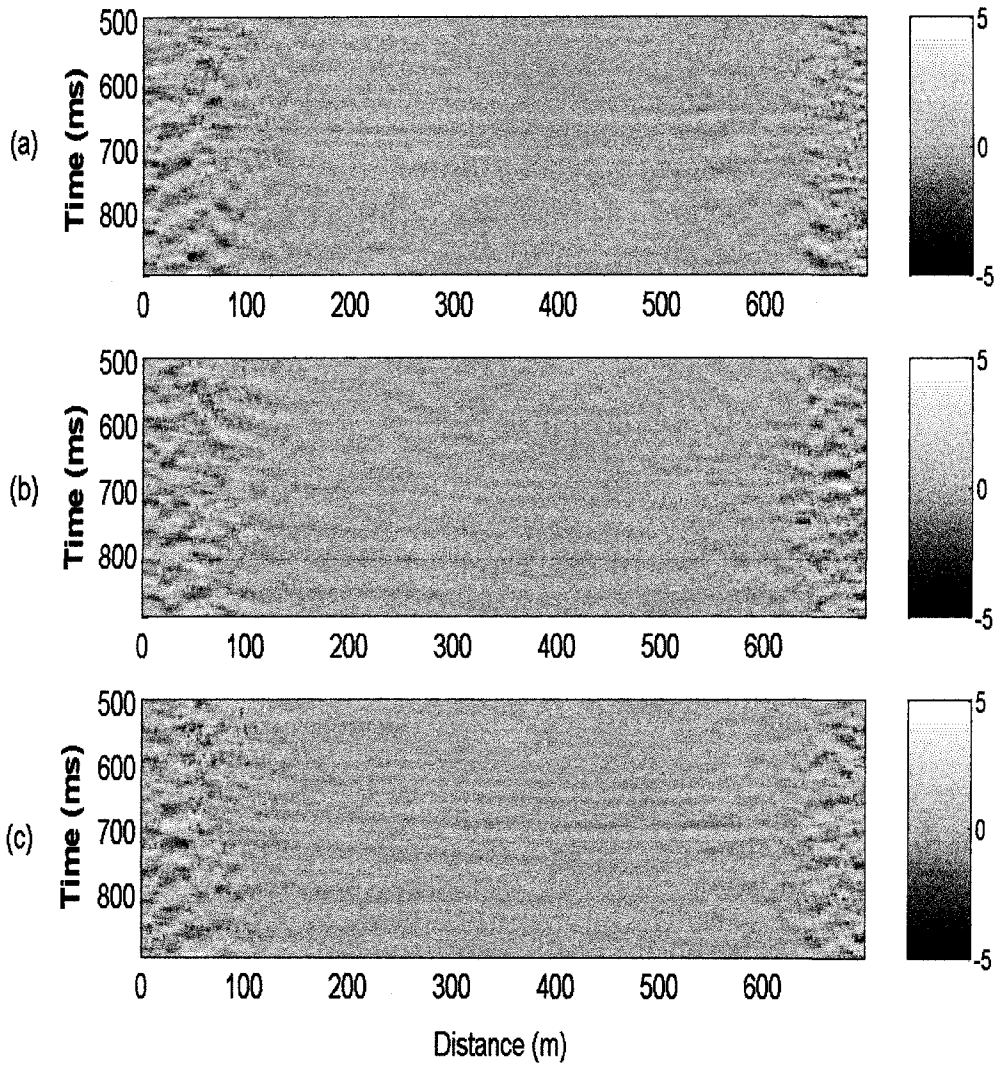

Figure 5.15: Time-lapse seismic difference profiles along the W-E direction. (a) Difference between October 2001 and July 2001; (b) Difference between June 2002 and July 2001; (c) Difference between October 2002 and July 2001.

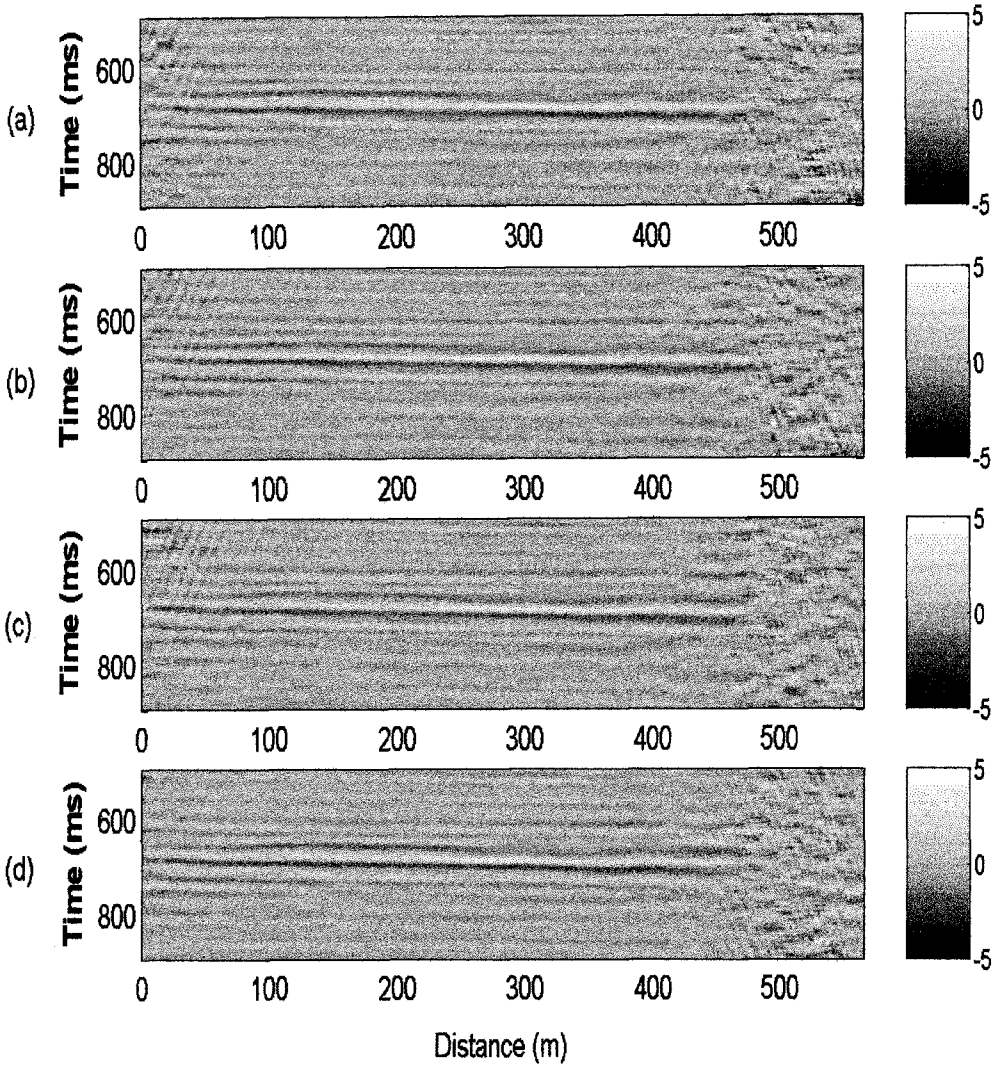

Figure 5.16: Time-lapse seismic profiles along the N-S direction. (a) July 2001; (b) October 2001; (c) June 2002; (d) October 2002.

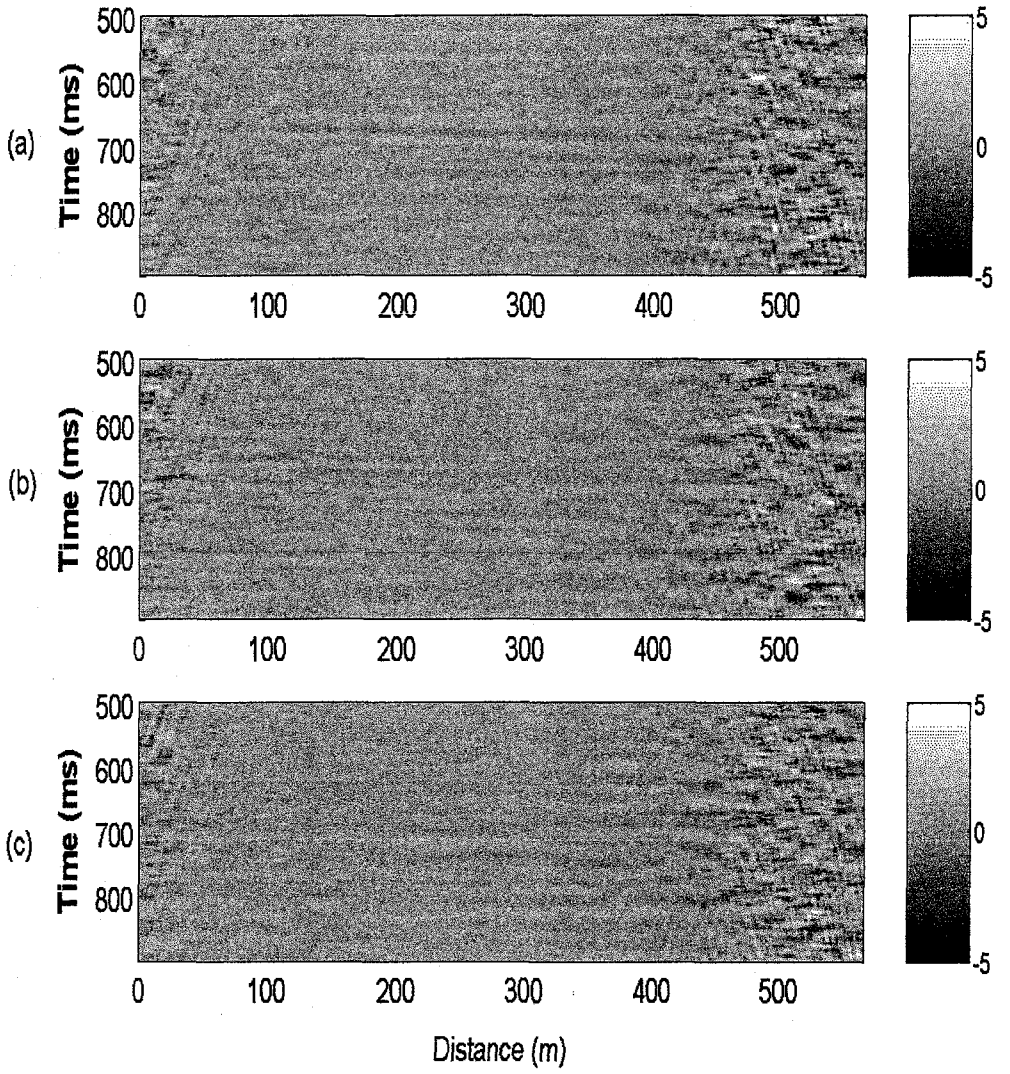

Figure 5.17: Time-lapse seismic difference profiles along the N-S direction. (a) Difference between October 2001 and July 2001; (b) Difference between June 2002 and July 2001; (c) Difference between October 2002 and July 2001.

lected sliding window size is 100 ms. The red color represents a good correlation which is close to 1, and the deep blue color represents a poor correlation. The generally observed variations along the W-E direction are smaller than those along the N-S direction. Since there are no horizontal well pairs to cross the W-E direction seismic line, any variations along this direction can likely be attributed to the non-repeatability during the acquisition and processing. In contrast, the relatively greater variations along the N-S direction seismic line can be considered to be produced under the dynamic geology environment.

The average PEAR values within the sliding window from 633ms to 760ms are shown in Figure 5.19(a) and 5.19(b). The left frames represent correlation values at different CMP positions. Small, even negative values are observed at the edge of these plots while near the central part, the observed values are close to 1. The right frames are scatter plot of the PEAR values as a function of CMP stack fold number. Fitted cubic curves are also shown together with these scattering points. These PEAR values are found proportional to the stack fold number. When the stack fold number is above 40, the calculated PEAR values are close to 1 which shows higher repeatability.

PRED and NRMS

The calculated PRED and NRMS values within the designed window 633 $\sim$ 760 ms are shown in Figure 5.20(a) and 5.20(b). The lags used in PRED are within the range [0, 16]. Within the relatively higher stack fold area, for example [300,500] m along the W-E direction, the calculated NRMS values shown in 5.20(a) are mainly distributed within the range [15%, 35%], and the calculated PRED values are close to 100%. The seismic data distributed within such area are highly repeatable. On the other hand, at the ends of the profile with fewer stack fold numbers, up to 180% NRMS values and close to 0% PRED values are observed. The seismic data distributed within this area are highly unrepeatable. Similar PRED and NRMS features along the N-S direction can be observed (5.20(b)).

5.5.3 Discussion

The selected NRMS and PRED values with higher S/N ratio within 200 $\sim$ 500 m along the W-E direction and within 50 $\sim$ 400 m along the N-S direction are shown in Figure

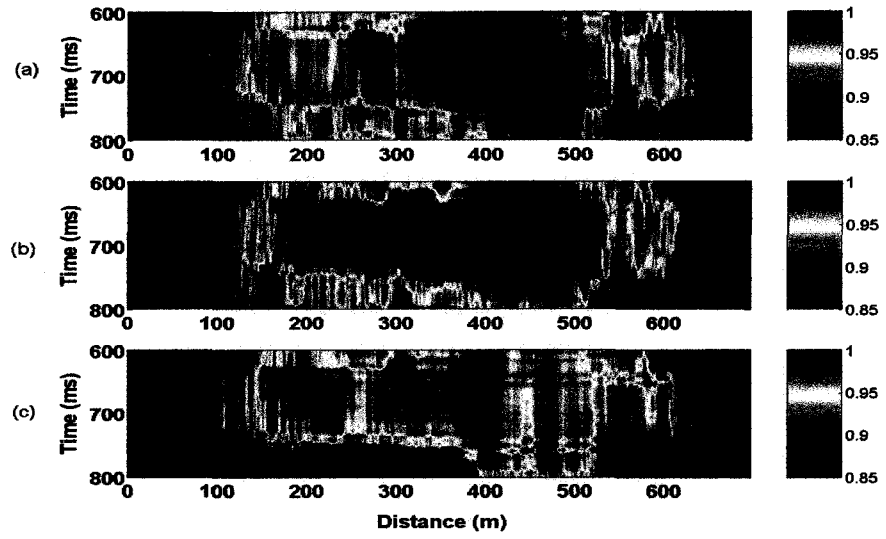

(a)

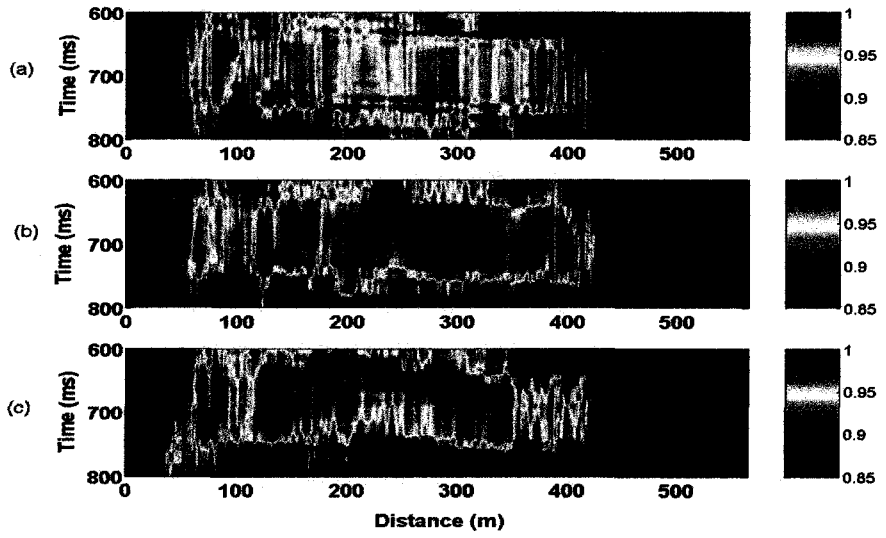

(b)

Figure 5.18: The PEAR profiles with 100 ms sliding window. (a) Profiles along the W-E direction; (b) Profiles along the N-S direction. From top to bottom, each panel represents correlation between October 2001 and July 2001, June 2002 and July 2001, October 2002 and July 2001.

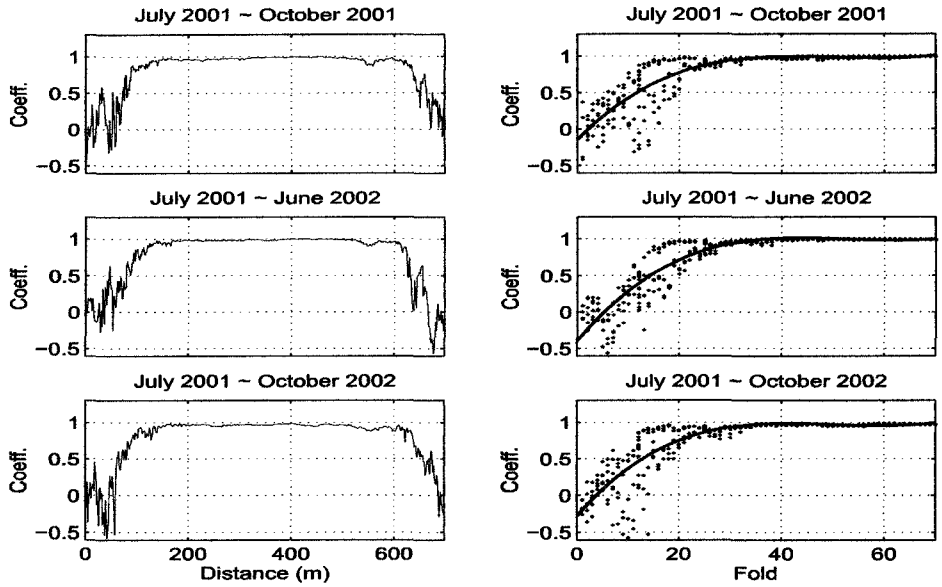

(a)

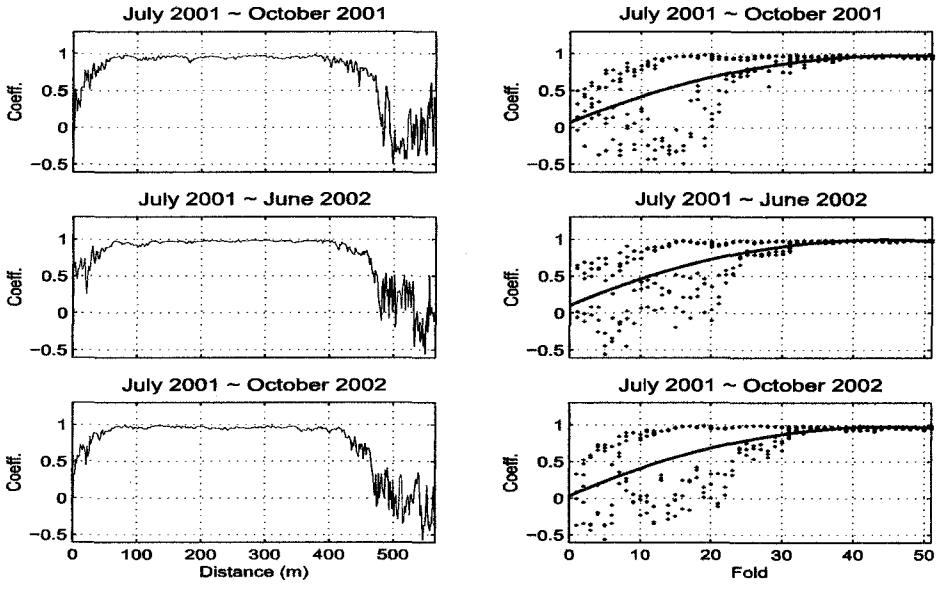

(b)

Figure 5.19: Average PEAR values calculated within the window 633 ~ 760 ms. (a) Along the W-E direction seismic line; (b) Along the N-S direction seismic line.

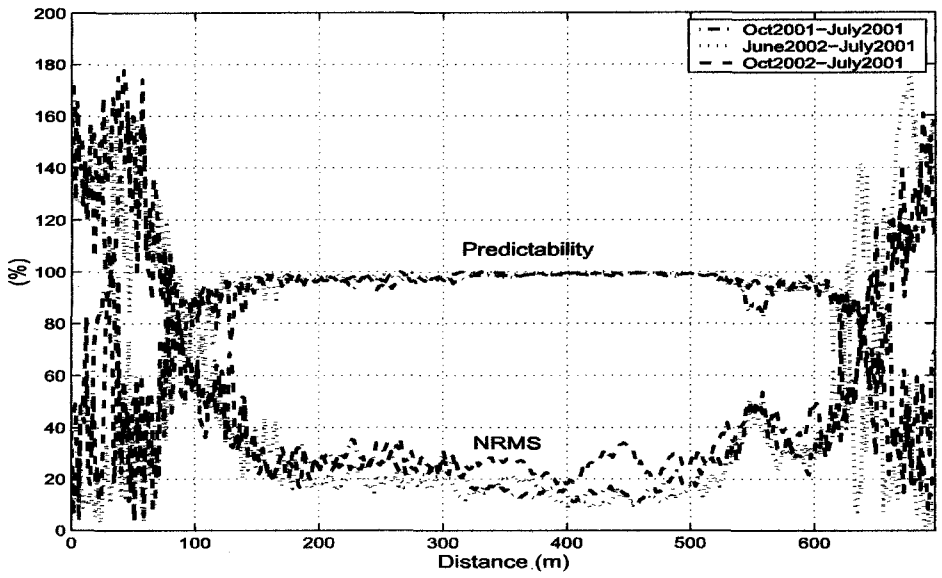

(a)

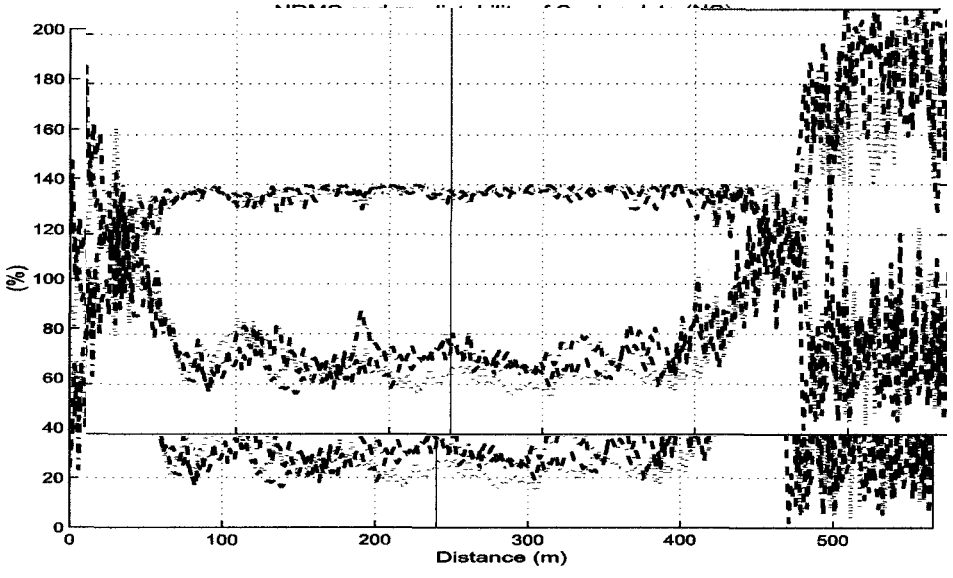

(b)

Figure 5.20: The calculated NRMS and PRED values. (a) Along the W-E direction seismic line; (b) Along the N-S direction seismic line.

5.21(a) and 5.21(b). Along the W-E direction, within the range 400 $\sim$ 480 m , the first two set of NRMS values are found less than 20%, and the third set of NRMS values are within 18% $\sim$ 33%. All the PRED values within the same distance range are found above 98%.

Along the N-S direction, within the range 200 $\sim$ 300 m, the first and the third set of NRMS values are within 25% $\sim$ 40%, and most of these values are above 30%. The second set of NRMS values are distributed within the relatively narrow range 20% $\sim$ 30%. The PRED values within the same distance range are mainly distributed within 92% $\sim$ 100%, and most values are around 96%. Generally, there are higher NRMS values and lower PRED values along the N-S direction than along the W-E direction. Therefore, the seismic repeatability is relatively higher along the W-E direction than along the N-S direction.

In the evaluation of seismic repeatability, a PRED threshold value can be set up, for example 90%. When the PRED values are above this threshold value, the PRED values are generally related to the signals which are considered highly repeatable (*Kristiansen et al.*, 2000). If the same threshold value is selected for East Senlac case, the time-lapse seismic profiles are deemed to be highly repeatable.

The factors to affect seismic repeatability are usually dependent case by case conditions, and the NRMS can be employed in this analysis. For example, in the case of Gulf Mexico, the NRMS values are directly correlated with CMP deviations due to the steamer moving; in the case of North Sea, the NRMS values are directly related to the background random noise and nothing about seismic signals (*Kragh and Christie*, 2002). In the East Senlac case, the NRMS values are found directly related to the CMP stack fold distribution. The correlation between CMP stack fold and NRMS value is illustrated in Figure 5.22(a) and 5.22(b). The NRMS values shown in Figure 5.22(a) for the W-E direction are generally higher in the west than in the east. In contrast, the NRMS values shown in 5.22(b) at the north of N-S direction are generally smaller than the values at the south and there exists wider gap in between. In summary, the CMP stack fold is the main factor to directly affect the calculated NRMS values. However, the presence of different NRMS values at the same stack fold position may imply that in addition to the factor of nonuniform CMP stack fold distribution, some other unknown factors which actually change in the reservoir may also directly affect the calculated NRMS values.

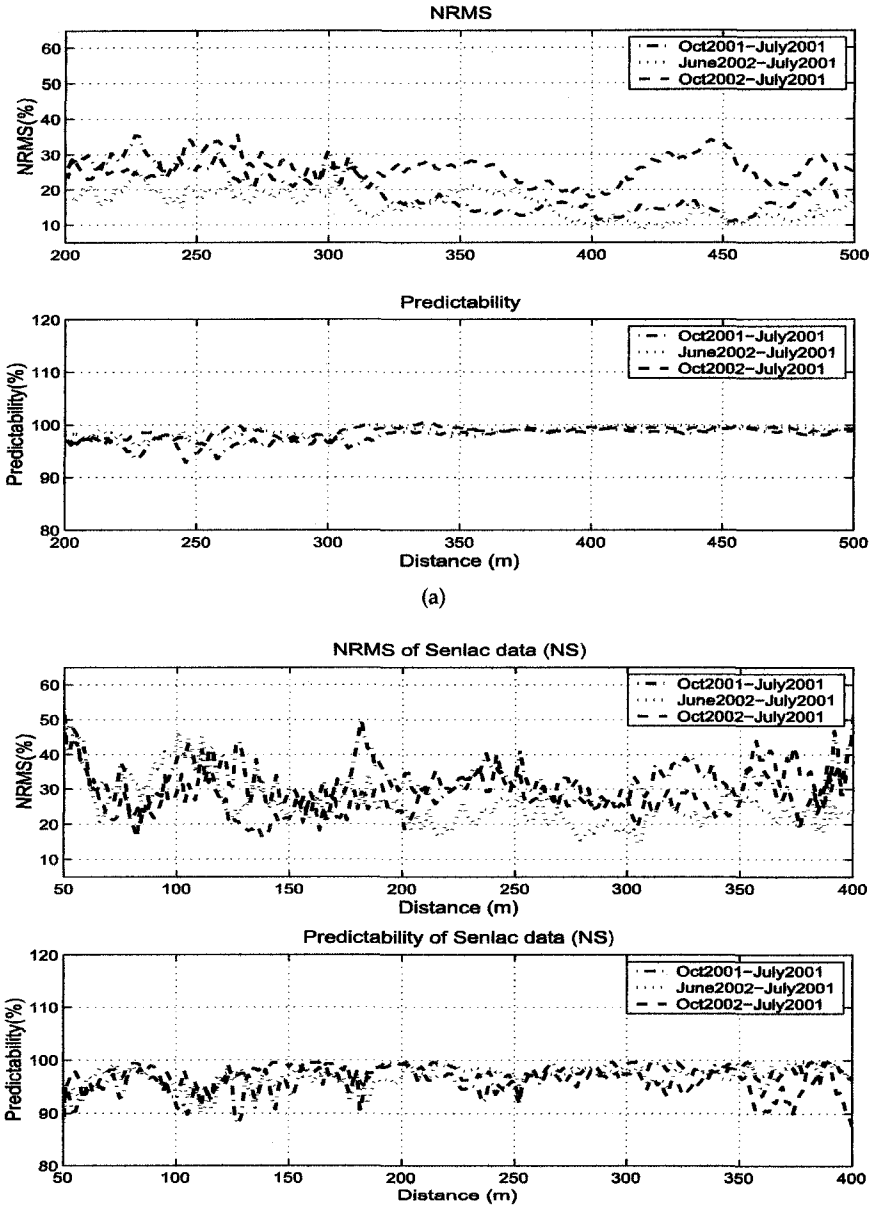

Figure 5.21: The selected NRMS and PRED values with higher S/N ratio. (a) Along the W-E direction; (b) Along the N-S direction.

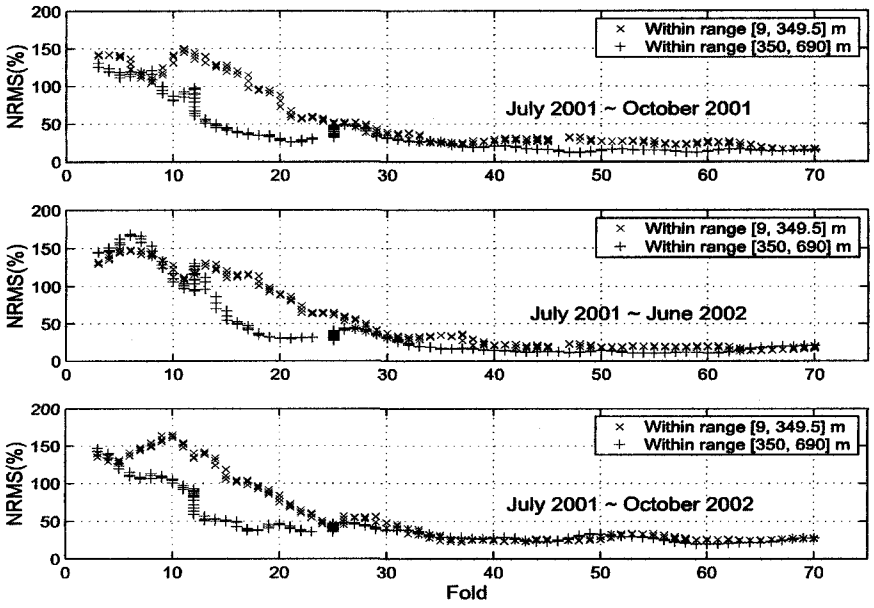

(a)

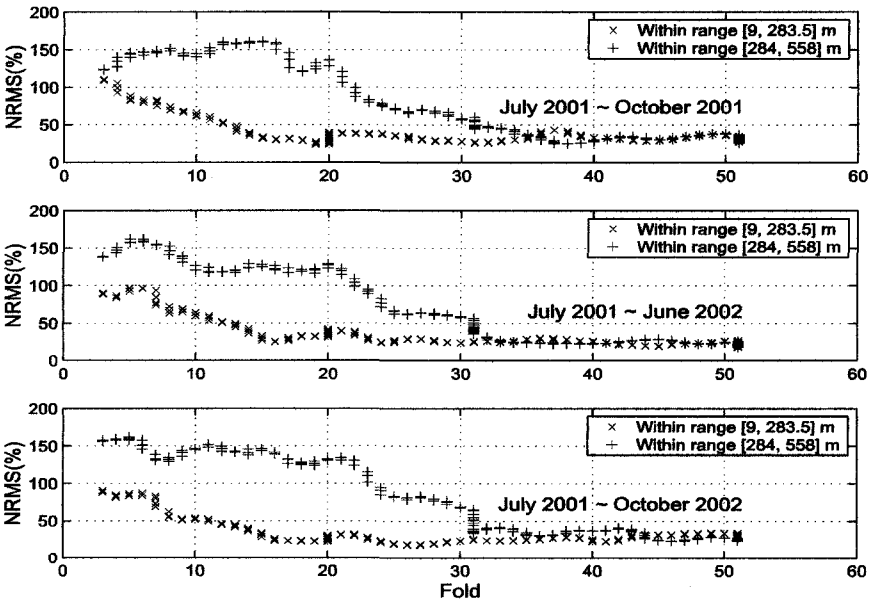

(b)

Figure 5.22: Correlation between the CMP stack fold number and the NRMS value. (a) Along the W-E direction; (b) Along the N-S direction.

5.6 Summary

High repeatability on shot and geophone positions is well maintained between the seismic surveys. The observed maximum deviation is less than 3 meters, and most deviations are in the order of centimeters. Through the repeatability investigation on the recorded source signals and the transformed spectra, it is found that the recorded source signals are unique and non-repeatable due to the differing coupling conditions between the vibrator base plate and the local soil surface.

In addition, the three metrics including PEAR, NRMS and PRED are employed to quantity the post-stack seismic repeatability. The observed higher PEAR values along the W-E direction than along the N-S direction may reflect the two different static and dynamic geology environments. From the calculated PRED values, it is found that the repeatability along the W-E direction is better than along the N-S direction. From the calculated NRMS values, it is found that they are directly related to the CMP stack fold distribution, and it has directly affected the post-stack seismic repeatability.

Chapter 6

Time-lapse seismic attribute analysis and integrated interpretation

6.1 Introduction

A variety of seismic attributes can be employed to detect time-lapse seismic variations, for example, time shift, amplitude variation and spectral variation which have proved useful for indicating the steam heated zone features (e.g. *Dilay and Eastwood*, 1995). The selection of seismic attributes employed are usually dependent on the conditions a particular case is subject to.

In the first part of this chapter, the SAGD scenario occurring in East Senlac area will be briefly described. Then a series of time-lapse rock properties will be estimated based on Gassmann's equation. In the third part, seismic attributes will be derived from the data along both the W-E direction and along the N-S direction. From the estimated seismic attributes, the different geology environment will be further diagnosed. In the fourth part, a complementary seismic attribute, the time-lapse seismic "impedance" will be inverted by using the recently proposed hybrid data transformation method in chapter 2. Integrated interpretation on the inverted "impedance" will be attempted by combining the predicted time-lapse rock properties. The final part is the summary to conclude this chapter.

6.2 SAGD scenario and time-lapse rock property simulation

6.2.1 The SAGD scenario

During the SAGD processes, factors such as temperature, pressure, and fluid saturations may directly affect the subsurface rock properties. Such rock property variations are possibly detected from the recorded seismic data. The recorded history data include the injected steam and gas, produced water, gas and oil (Figure 6.1(a), 6.1(b), 6.1(c)), the recorded pressure (Figure 6.2) and temperature (Figure 6.3) provided by the operator at the time. The relevant history data corresponding to the time when the seismic surveys were acquired are listed in Table 6.1. The abnormal significant jumps in temperature and pressure should be ignored in practical data analysis as these are likely related to changes in the fluids within the injection wellbores. The temperature and the pressure responses in the surrounding reservoir will remain more constant. Some production data not shown in these figures are not available at present. It must be remembered that these values are those measured in the injection (B1) wellbore. The conditions in the broader reservoir, however, will be quite different and would require a full reservoir simulation to better understand. Unfortunately, such information was not available or does not exist.

From the data listed in Table 6.1, it is found that the injected steam decreases significantly from the 7864 m^3 in July 2001 to the 114 m^3 in October 2001, and it continues to decrease until to zero in June 2002. In contrast, the injected gas increases from the initial 325,000 m^3 in July 2001 to the 849,000 m^3 in October 2001, but it decreases to the 438,000 m^3 in June 2002. Meanwhile, the water, oil and gas production volume all decrease at these calendar dates. The pore pressure decreases from the 5.2 MPa in July 2001 to the 4.9 MPa in October 2001. The other two pressures in June 2002 and in October 2002 are not available at present. The temperature decreases from 198 $°C$ in July 2001 to 166 $°C$ in October 2001, then it drops significantly to 81 $°C$ in June 2002. After that, the temperature (85 $°C$) does not change much in October 2002. However, it is not clear how reliable these temperature data are, given the rather large and discontinuous changes observed. Unfortunately, this analysis suffers in terms of the lack of appropriate and sufficient information to completely analyze the problem. This problem stems from short term economic decisions.

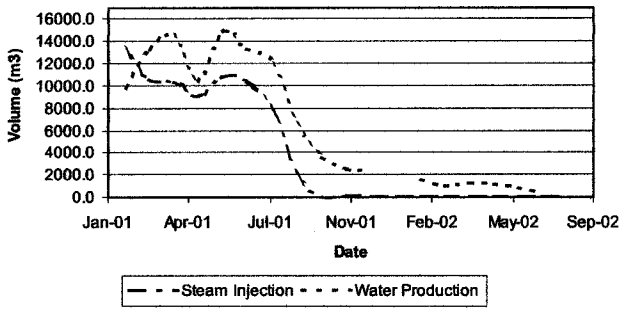

(a)

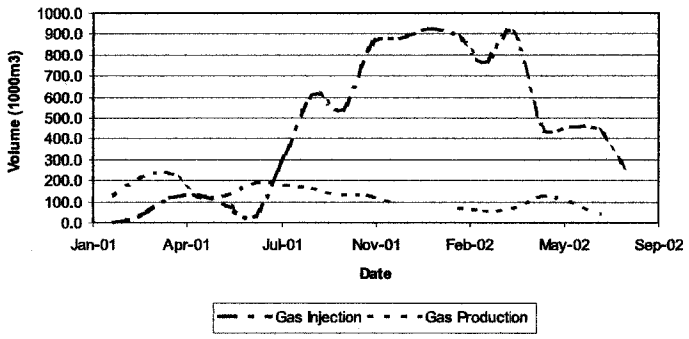

(b)

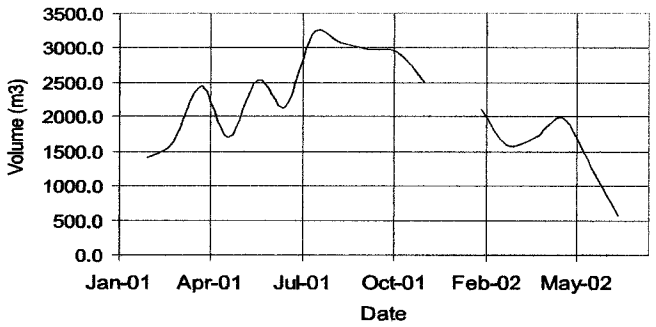

(c)

Figure 6.1: Injection and production data (data is from Saskatchewan government). (a) Monthly water injection and water production data; (b) Monthly gas injection and gas production; (c) Monthly oil production.

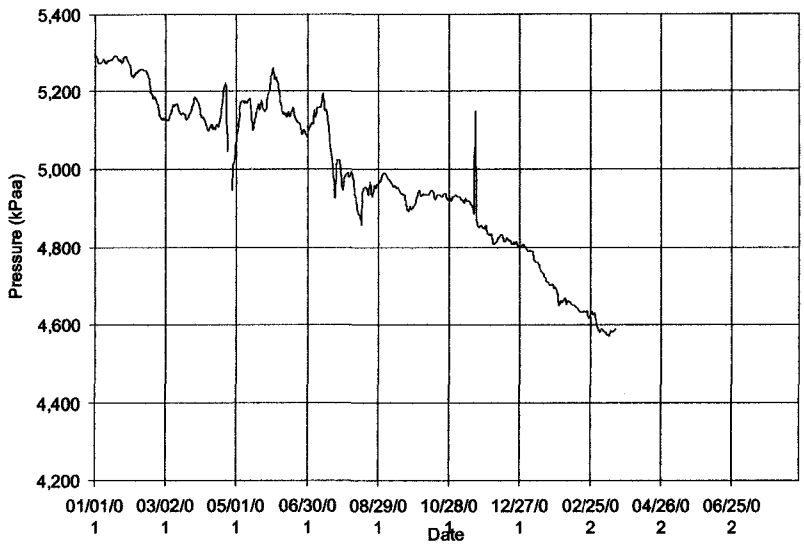

Figure 6.2: B1 bottom hole pressure.

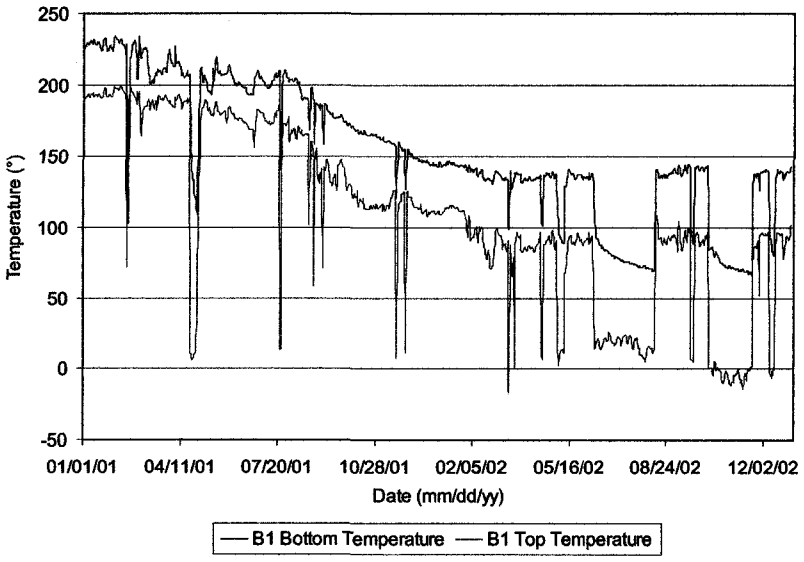

Figure 6.3: B1 temperature.

Table 6.1: Monthly production and injection in East Senlac area (16-12-40-26W3M (B1)).

	July 2001	October 2001	June 2002	October 2002
Steam injection (m^3)	7864	114	0	—
Gas injection ($1000m^3$)	325	849	438	—
Water production (m^3)	12015	2477	398	—
Gas production ($1000m^3$)	178	126	37	—
Oil production (m^3)	3208	2936	557	—
Bottom hole pressure (MPa)	5.2	4.9	—	—
Bottom hole temperature($°C$)	198	166	81	85

6.2.2 The time-lapse rock property simulation

There is insufficient information to completely and deterministically carry out analysis of the steam zone because, as just noted, this would require additional information that is not available. Consequently, a series of randomly distributed fluid saturations are selected to simulate the time-lapse rock property scenarios which are assumed to occur in July 2001, October 2001, and June 2002. The simulated parameters include effective fluid bulk modulus, density, compressional velocity, shear velocity and acoustic impedance.

Fluid/gas substitution model

In this simulation, the estimated rock properties are the function of fluid saturation, temperature and pressure. The fluid consists of gas, water, and oil. The gas used here is methane.

First, fluid parameters at different temperatures and at different pressures are selected. The compressional velocity and density for methane gas and water can be directly obtained from the public web page *http : //webbook.nist.gov/chemistry/fluid.* The compressional velocity and density for oil can be estimated by using *Batzle and Wang* (1992)'s formula (18), (19), and (20a) which can be written as,

$$\rho_P = \rho_0 + (0.00277P - 1.71 * 10^{-7}P^3)(\rho_0 - 1.15)^2 + 3.49 * 10^{-4}P \tag{6.1}$$

$$\rho = \rho_P/[0.972 + 3.81 * 10^{-4}(T + 17.78)^{1.175}] \tag{6.2}$$

$$V = 2096(\frac{\rho_0}{2.6 - \rho_0})^{1/2} - 3.7T + 4.64P + 0.0115[4.12(1.08\rho_0^{-1} - 1)^{1/2} - 1]TP \tag{6.3}$$

Table 6.2: The relevant parameters used for time-lapse rock property simulation.

	July 2001	October 2001	June 2002
k_d [GPa]	8.93		
μ_d [GPa]	4.58		
k_s [GPa]	36		
ρ_s [kg/m^3]	2650		
ϕ [%]	32.3		
T [°C]	198	166	81
P [MPa]	5.2	4.9	4.3
ρ_{Me} [kg/m^3]	21	22	24
k_{Me} [GPa]	0.0065	0.0063	0.0056
ρ_W [kg/m^3]	870	904	973
k_W [GPa]	1.59	1.88	2.34
ρ_O [kg/m^3]	831	857	930
k_O [GPa]	0.71	0.93	1.70

where ρ_0 is a reference density measured at 15.6°C and atmospheric pressure, T represents temperature, and P represents pressure. It must be recognized that all of these results and particularly those for the oil, are based on rather small empirical examples; and it is currently unknown how much this lack of information adds to the uncertainties in this analysis. Therefore, these are still only rough estimates of what the properties might be.

The parameters, such as porosity, solid material bulk modulus, frame bulk modulus and frame shear modulus, can be directly obtained from the previous feasibility study. Temperatures and pressures are taken from Table 6.1. The pressure in June 2002 is not available at present and it is roughly estimated from the fitted line shown in Figure 6.4. All these parameters which will be used in the subsequent rock property simulation are summarized in Table 6.2.

It also needs to be noted that the values given here are only those at the wellbore itself. A more proper analysis is required to account for the spatial variations in pressure, temperature, and saturation away from the wellbore. This requires modelling and is beyond the scope of the current study.

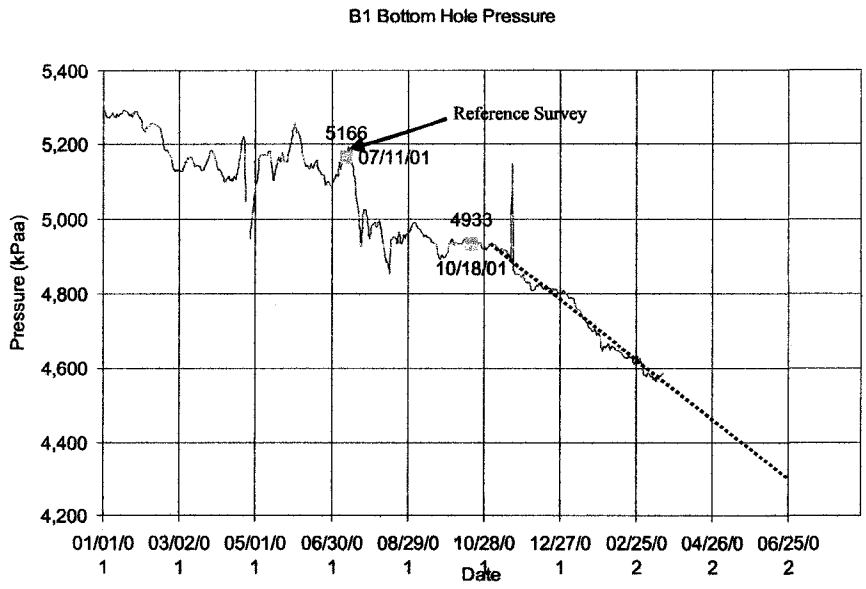

Figure 6.4: The extrapolated pressure based on the available data.

Simulated time-lapse rock properties with randomly distributed fluid saturations

Using the parameters listed in Table 6.2, a series of randomly distributed fluid saturations are selected to simulate the time-lapse rock properties. The selected oil saturation is limited within [0, 0.85]. This is because the SAGD process occurring in East Senlac area tends to decrease oil saturation. Therefore, the maximum oil saturation should not exceed the initial oil saturation 0.85.

In the first set of simulations, the pore pressure (i.e. the reservoir pressure in petroleum engineering parlance) is 5.2 MPa and the temperature is 198°C. The goal of this simulation is to predict rock properties in the immediate vicinity of the wellbore pair in July 2001. The calculated rock properties are shown in Figures 6.5(a), 6.5(d), 6.5(g), and 6.5(j). Frame 6.5(a) represents fluid bulk modulus which decreases with gas saturation and increases with water saturation. Frame 6.5(d) represents density. Higher density values are found to mostly distribute within the higher oil saturation and the higher water saturation area. Frame 6.5(g) and frame 6.5(j) represent compressional velocity and

shear velocity. Both have similar distributions, but have opposite distribution to density. Compressional velocity and shear velocity are found to increase with gas saturations. It seems that the smaller gas density and compressibility has dominated the whole velocity distribution.

In the second simulation, which represents the October 2001 scenario, the pressure is 4.9 MPa and the temperature is 166°C. The simulated results are shown in Figures 6.5(b) 6.5(e), 6.5(h), and 6.5(k).

In the third simulation which represents the June 2002 event, the pressure is 4.3 MPa and the temperature is 81°C. The simulated results are shown in Figure 6.5(c), 6.5(f), 6.5(i), and 6.5(l). The overall tendency distributions in the latter two simulations are similar to those calculated in the first simulation.

Simulated time-lapse rock properties with the constant oil saturation at 20%

For the East Senlac SAGD model, the oil saturation within the mature steam chamber is assumed to be 20% after production. Water and gas saturations change within the range [0%, 80%]. The simulated rock properties are shown in Figure 6.6(a) ~ 6.6(c). Figure 6.6(a) shows effective bulk modulus which is found to change significantly with pore pressure and temperature when the gas saturation is less than 5%. When the gas saturation is more than 5%, the effect of temperature and pressure on effective bulk modulus is hardly observed. Panel 6.6(b) represents the density which is found to decrease linearly with gas saturation at the constant temperature and pressure, and it decreases with temperature and pressure at constant gas saturation.Panel 6.6(c) shows the compressional velocity which is found the greatest when the fluids completely consist of water and oil at the lowest temperature and pressure. Meanwhile, the compressional velocity increases with gas saturation at the constant temperature and pressure. At the constant gas saturation, the compressional velocity is anti correlated with the temperature and pressure.

One additional parameter, the acoustic impedance, is calculated (Figure 6.7). It is found that the acoustic impedance decreases with gas saturation at constant temperature and pressure, and decreases with temperature and pressure at the constant gas saturation. Obviously, the acoustic impedance changes with pressure, temperature, and fluid saturation. When any of these parameters is unknown, it will be very difficult to correctly

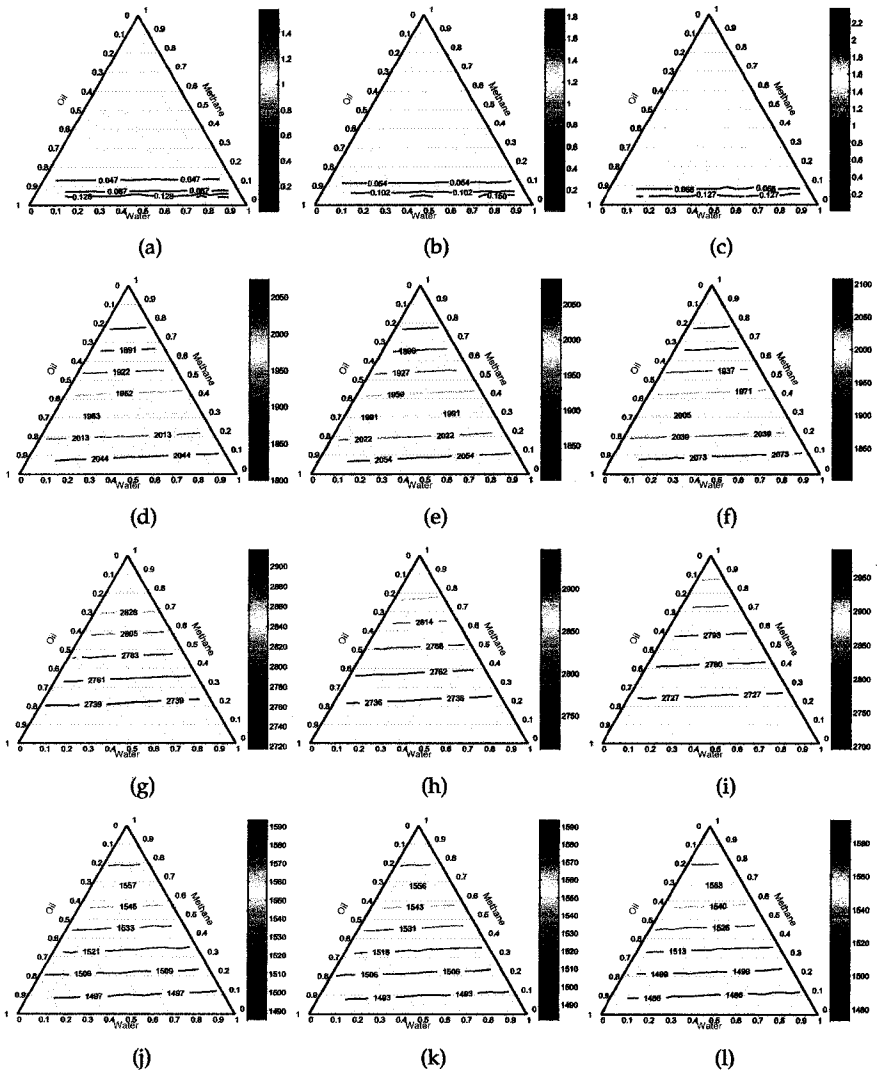

Figure 6.5: The simulated rock properties. (a), (b), (c) - Fluid bulk modulus (GPa); (d), (e), (f) - Density (kg/m^3); (g), (h), (i) - Compressional velocity (m/s); (j), (k), (l) - Shear velocity (m/s). Each column represents the value calculated respectively at pressure 5.2 MPa, 4.9 MPa and 4.3 MPa and at temperature 198°C, 166°C, and 81°C, respectively.

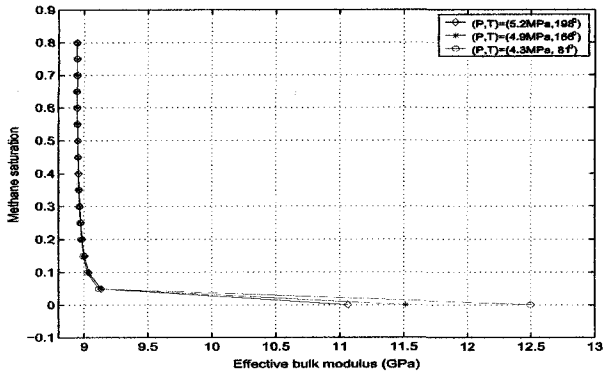

(a)

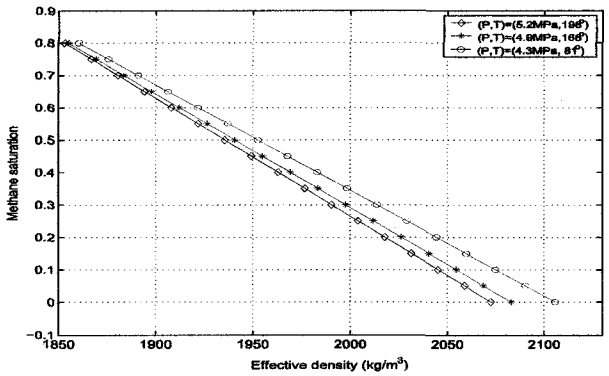

(b)

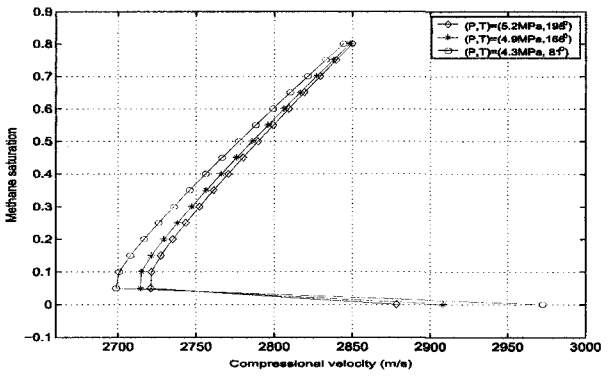

(c)

Figure 6.6: Time-lapse rock properties with the constant oil saturation at 20%. (a) Effective bulk modulus; (b) Density; (c) Compressional velocity.

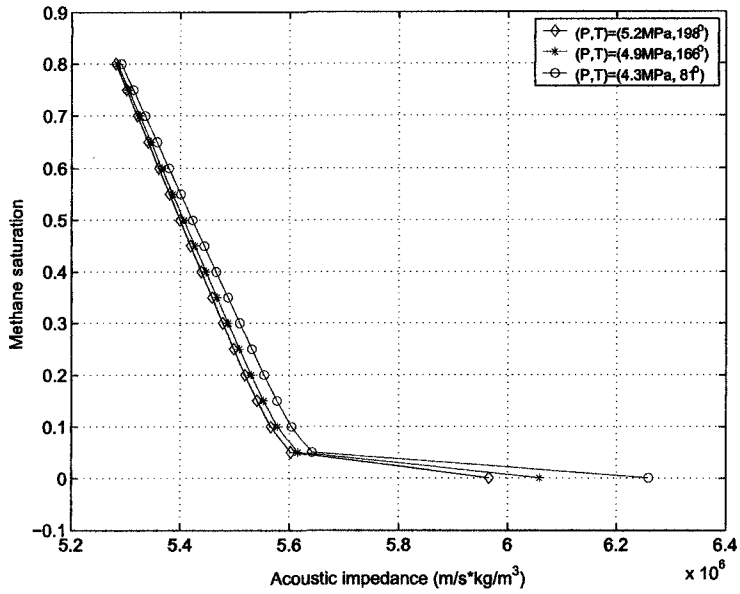

Figure 6.7: The estimated time-lapse acoustic impedance with oil saturation at 20%.

predict the variations in the acoustic impedance.

It is important to note that we have not here considered any changes in the frame modulus due to variations either in pressure or in temperature. We have earlier discussed a possible decay in the shear modulus with pressure due to increasing temperature. However, it needs to be remembered here that the declining pore pressure curves of Figure 6.4 also mean that the effective confining pressure $\sigma_{eff} = \sigma_{conf} - \sigma_{pore}$ is actually increasing. That is, the solid frame of the rock is supporting an even larger stress. While this factor is expected to increase the frame modulus k_d we have ignored this effect.

6.3 Time-lapse seismic attribute analysis

The two horizontal well pairs B1 and B2 which experienced SAGD process crossed the N-S direction seismic line. Rock property variations might be observed from time-lapse seismic data. Conversely, the observed seismic variations can be considered as rock property caused variations under the dynamic geology environment. On the other hand, the B1 and B2 did not cross the W-E direction seismic line. The observed seismic variations

can be considered as non-repeatability caused variations under the static geologic environment. In order to detect these different scenarios, one seismic attribute, the power spectrum, will be employed in this investigation. We do this under the caveat that in this case the time lapse signals are expected to be small particularly as we did not have a baseline survey.

6.3.1 The power spectrum along the W-E direction

The time-lapse seismic profiles along the W-E direction are shown in Figure 6.8. Within the illustrated window area [633, 760] ms, the power spectra are calculated.

The normalized power spectra are shown in Figure 6.9(a) $\sim$ (d). The CMP stack fold distribution at different CMP positions is shown in frame (e) which is used as a proxy to indicate seismic quality as indicated in the previous chapter. These spectra are similar, for example at the illustrated circle positions. Spectra at these two positions are shown in Figure 6.10(a) and 6.10(b). The shapes of these time-lapse spectra are very similar except that there are very small deviations within the higher frequency range [40, 60] Hz. Since the acquired seismic surveys have very high repeatability and the rock property caused variations were not expected at the time of data acquisition, these very similar power spectra should reflect the locally static geology environment. The existing deviations can be attributed to the non-repeatability caused variations.

6.3.2 The power spectrum along the N-S direction

The time-lapse seismic profiles along the N-S direction are shown in Figure 6.11. Within the selected window [633, 760] ms, the calculated power spectra are shown in Figure 6.12(a) $\sim$ (d). The CMP stack fold distribution at different CMP positions is shown in panel (e). From left to right, the two filled circles respectively represent the locations horizontal well pairs B1 and B2. These spectra are very similar, especially around the circle positions shown in panel (e) which possesses relatively higher image quality. The spectra at these circle positions are shown in Figures 6.13(a) $\sim$ (h).

Panel (a) shows the power spectra for the seismic trace located at 24 meters north of the well pair B1. This set of time-lapse power spectra are found to have the same predominate frequencies and to have similar wave shapes. Above 40 Hz, there are small

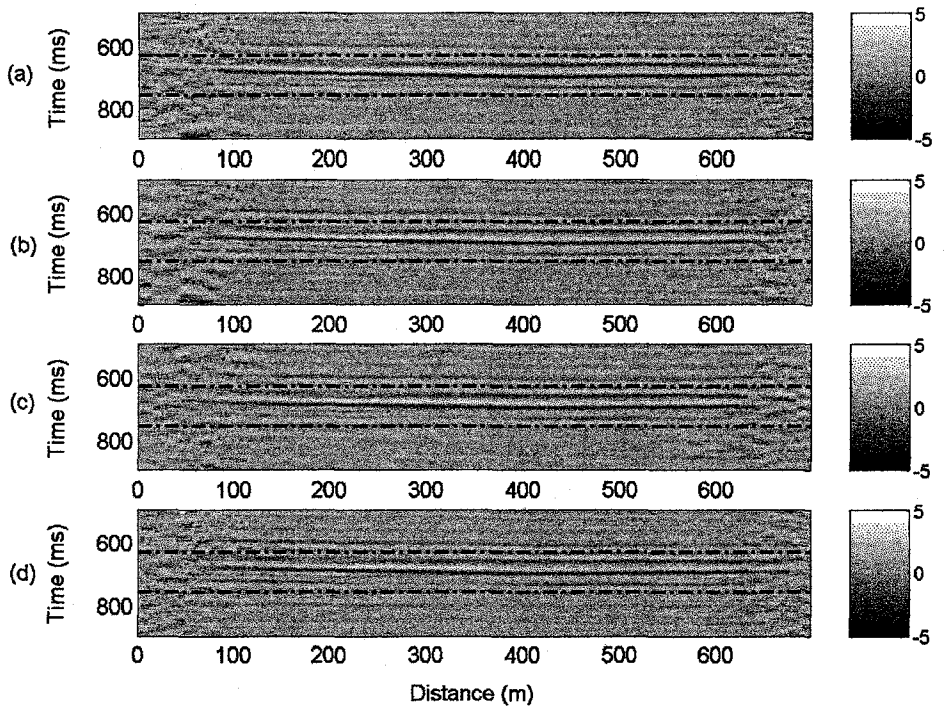

Figure 6.8: The W-E direction time-lapse seismic profiles and the designed window within which to estimate seismic attribute. (a) July 2001; (b) October 2001; (c) June 2002; (d) October 2002.

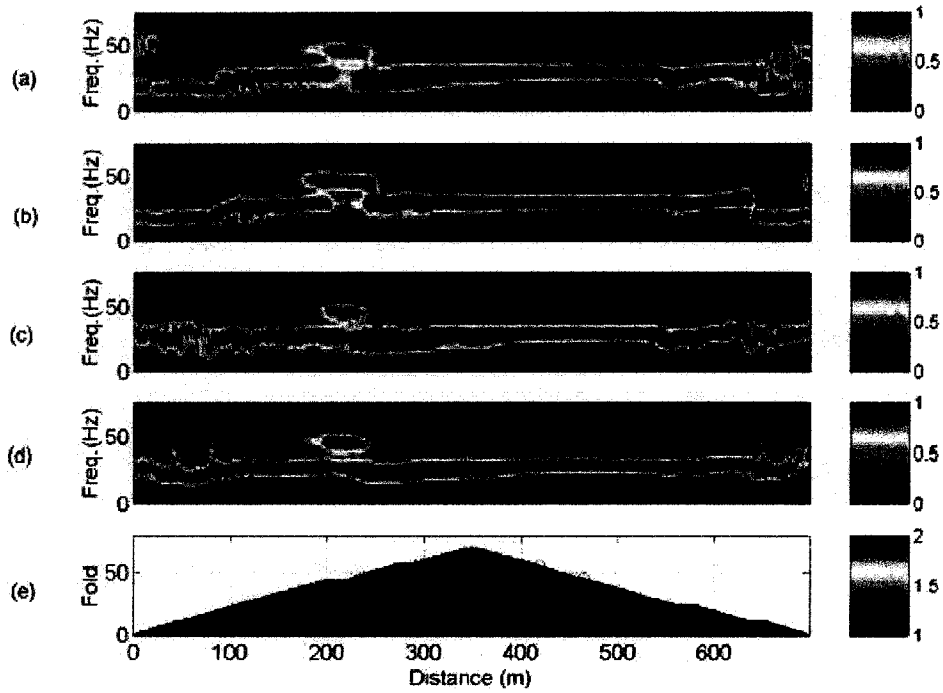

Figure 6.9: The time-lapse power spectrum profiles along the W-E direction. (a) July 2001; (b) October 2001; (c) June 2002; (d) October 2002; (e) The CMP stack fold distribution at different CMP positions.

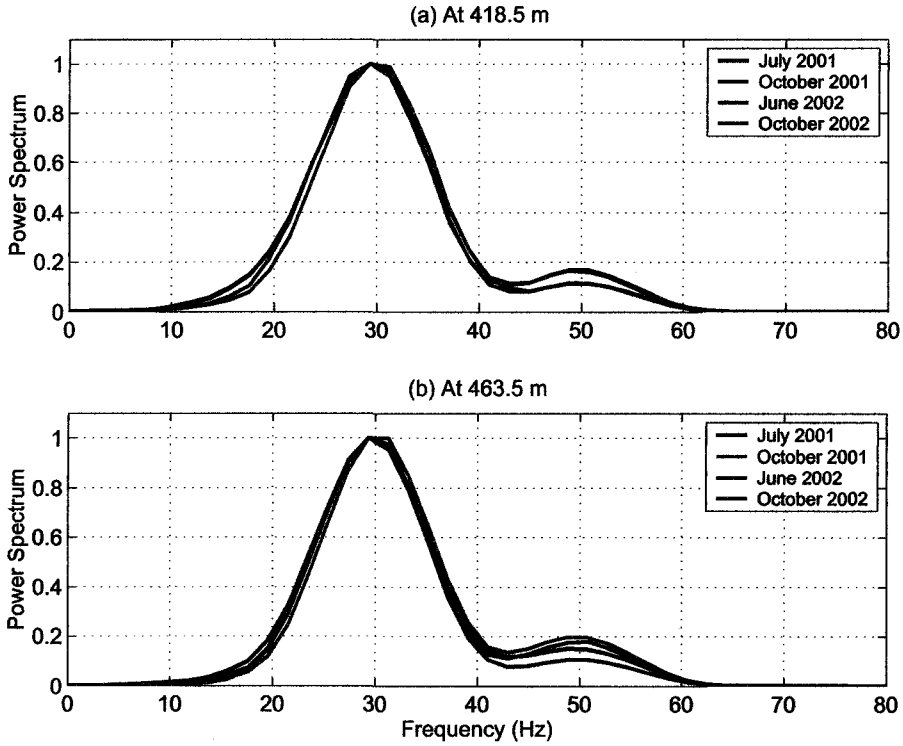

Figure 6.10: Time-lapse power spectra at the 418.5 m and at the 463.5 m.

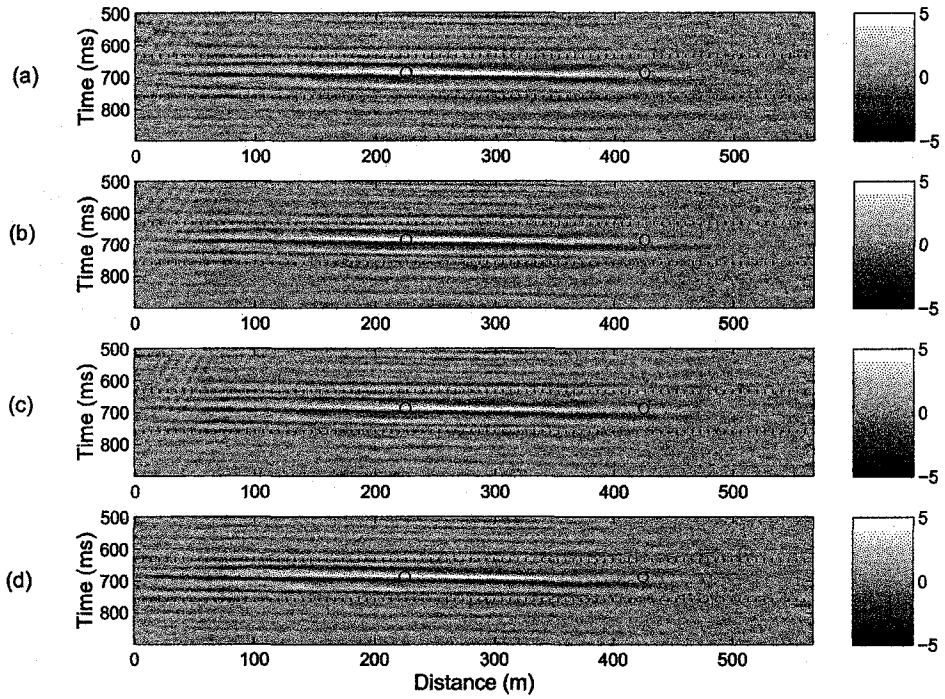

Figure 6.11: The N-S direction time-lapse seismic profiles and the designed window to calculate seismic attribute. (a) July 2001; (b) October 2001; (c) June 2002; (d) October 2002. (Left circle represents horizontal well pair B1; right circle represents horizontal well pair B2.)

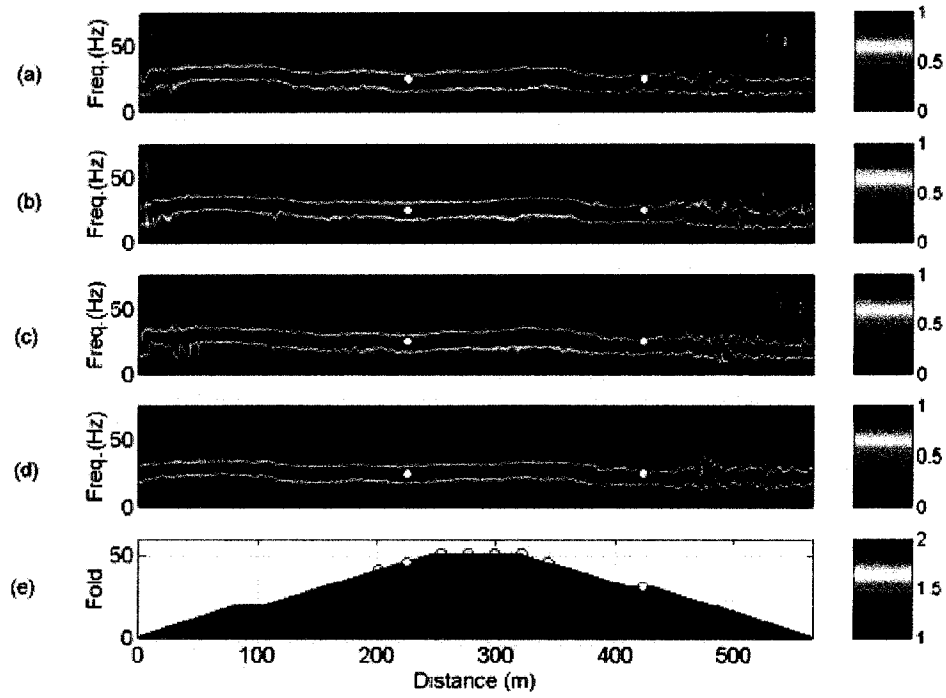

Figure 6.12: The N-S direction time-lapse power spectrum profiles. (a) July 2001; (b) October 2001; (c) June 2002; (d) October 2002; (e) The CMP stack fold distribution at different CMP positions. (The left filled circle represents B1; the right filled circle represents B2.)

deviations. Panel (b) shows the calendar spectra with the seismic traces located at the well pair B1. The main frequencies are found to increase with the calendar time interval with the maximum frequency shift being about +2 Hz. Panel (c) shows the power spectra with the seismic traces located at about 28.5 meters south of the well pair B1. Similar features but larger predominate frequency shifts are observed. In panel (d), (f), and (g), the main frequency shift becomes smaller. The panel (e) shows the almost identical main frequencies. The last panel (h) shows the power spectra with the seismic traces located at B2. This set of time-lapse power spectra are found to have almost identical shapes. Note that B2 terminates to the east of the N-S line and there may not be any variations expected at this location. However, we have no production information on pair B2 provided to us.

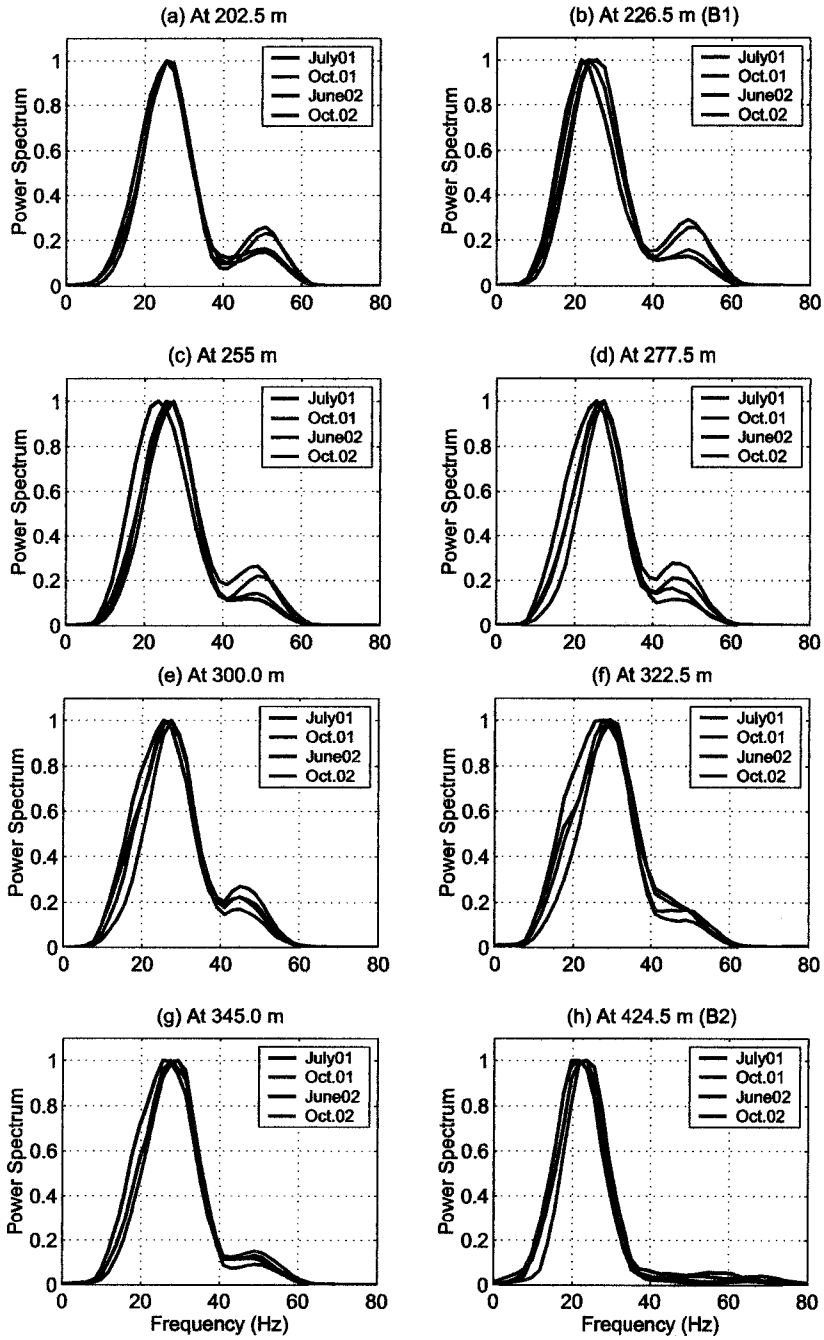

Figure 6.13: Time-lapse power spectra at different CMP positions.

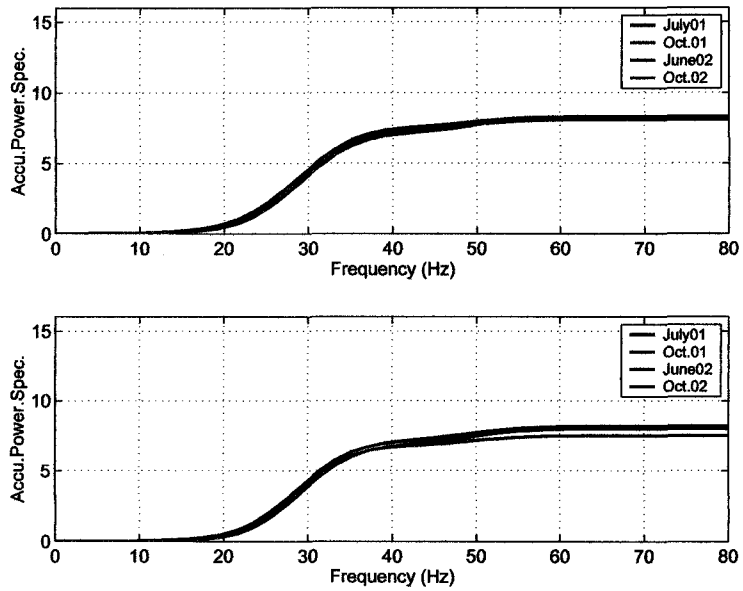

Figure 6.14: Cumulated power spectra at the 418.5 m and at the 463.5 m along the W-E direction.

6.3.3 Interpretation

From the previously presented time-lapse power spectra along the W-E direction, they are found very consistent except that there are very small deviations within the higher frequency range. Since the horizontal well pairs B1 and B2 did not cross the the W-E direction seismic line, these deviations can be attributed to the non-repeatability caused variations which are produced at the stage of seismic data acquisition. More apparent features can be observed from the calculated cumulative power spectra shown in Figure 6.14.

On the other hand, along the N-S direction seismic line, the main frequencies of these calendar spectra are found to increase slightly with the calendar time interval. Since the well pair B1 and B2 crossed this direction seismic line, the observed main frequency shift might be attributed to the ongoing SAGD related activities. However, some other factors, such as geological fracture and nonuniform CMP stack fold distribution, may also contribute to the observed seismic variations. The corresponding cumulative power spectra are shown in Figure 6.15. It is found that the accumulative power spectra for the

most recent survey are isolated from the other three calendar spectrum curves, especially within the higher frequency range.

Generally, the high frequency energy tends to be attenuated when high temperature steam is injected into steam chamber; especially at the initial stage of steam injection, the high frequency energy is attenuated significantly (*Dilay and Eastwood*, 1995). On the other hand, during the opposite process, when the temperature within steam chamber decreases, the high frequency energy should increase. This feature has been observed in East Senlac area that along the N-S direction seismic lines, the high frequency energy tends to increase when the temperature within steam chamber decreases. Another interpretation relies on the drop in pore pressure which increases the effective pressure and hence the rock velocity.

6.4 Impedance inversion and integrated interpretation along the N-S direction seismic lines

6.4.1 Impedance inversion

The recently proposed hybrid data transformation method is employed in this case study to invert for the "impedance". The seismic difference profiles along the N-S direction are selected in this inversion as they are the ones most likely to have detectable changes in the thin reservoir. Several steps can be included in this inversion process. The first step is to select initial "reflectivity" seed values. The second step is to choose an appropriate source wavelet. The method such as the least-squares described in Appendix C can be employed to estimate the source wavelet. Once the initial seed values and the initial source wavelet are selected, a new "reflectivity" can be inverted by using the proposed hybrid data transformation method. Several iterations are usually required until the optimal source wavelet and the optimal "reflectivity" are obtained. From the inverted "reflectivity", "impedance" can be further estimated.

The seismic window from 633 ms to 752 ms is selected in this inversion. Using the hybrid data transformation method, the inverted "impedance" profiles are shown in Figure 6.16.

The circles from left to right represent the horizontal well pair B1 and B2. Negative

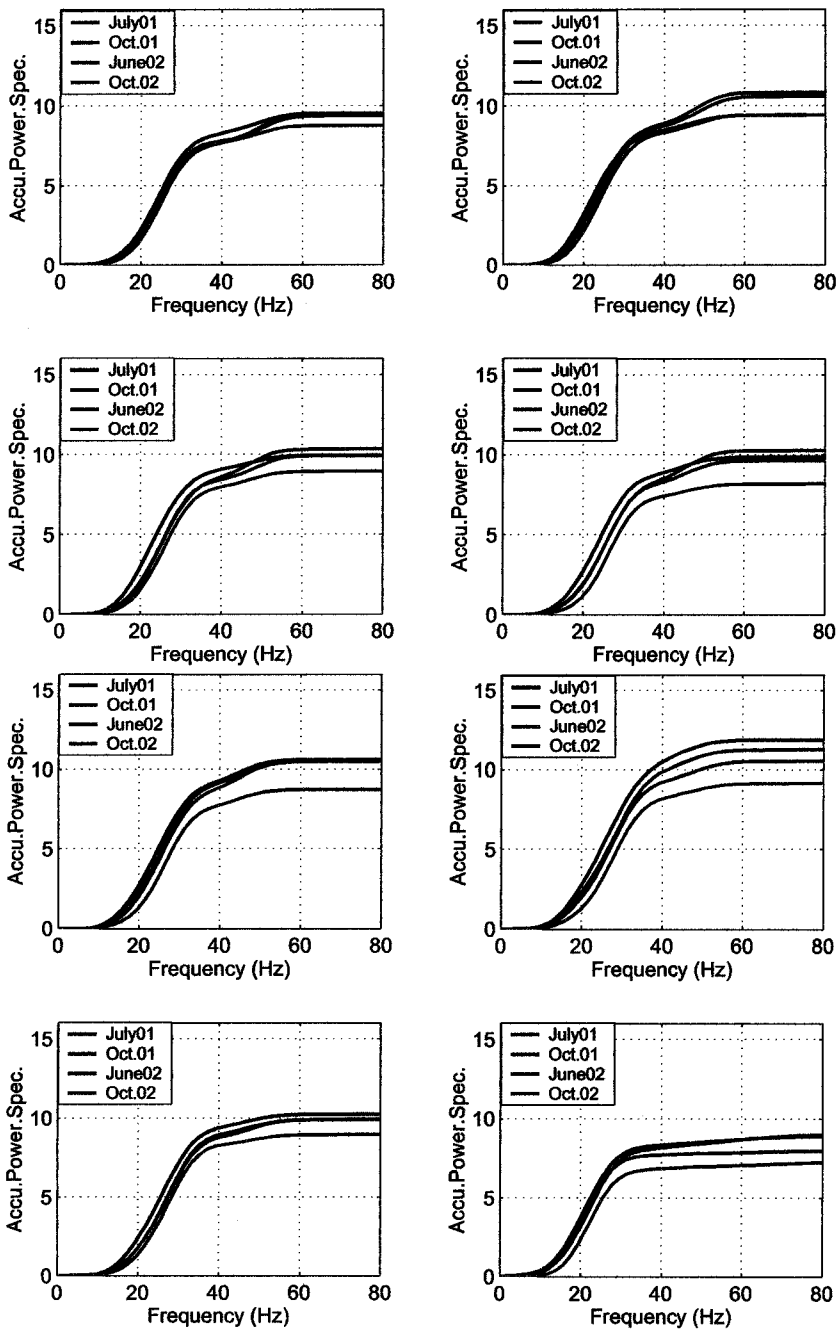

Figure 6.15: Cumulative power spectrum curves at different CMP positions along the N-S direction.

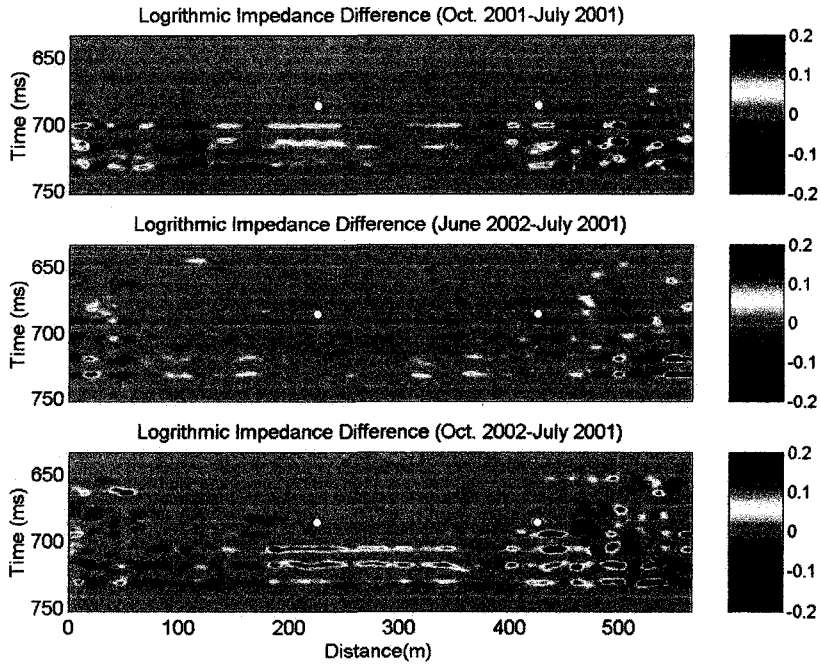

Figure 6.16: Inverted "impedance" profiles along the N-S direction seismic lines.

value in Figure 6.16 represents impedance decrease, and positive value represents impedance increase relative to the reference survey. The top panel shows the "impedance" inverted from July 2001 to October 2001. Above the reservoir, the inverted "impedance" does not change. This indicates the local static geology environment that physical variations are not expected in this area. Below the reservoir, the inverted "impedance" tends to increase, especially below the well pair B1 area, there are greater impedance increase. The middle panel shows the "impedance" inverted from July 2001 to June 2002. Relative to the reference survey, impedance decreases slightly. The bottom frame represents the "impedance" inverted from July 2001 to October 2002. The overall impedance variations are similar to those shown in the top panel except that there is a greater impedance increase.

6.4.2 Impedance interpretation based on rock physics

Theoretically, the pressure and temperature change will modify the rock property distribution within the reservoir area. But the rock properties above the reservoir area should not be affected. In the time domain, the rock property variations will extend below the reservoir area. This can be inferred from the "impedance" formula which is defined as the "reflectivity" integral. If the "reflectivity" is not zero, the estimated "impedance" at that time depth is also not zero, and this non zero "impedance" will accumulate with time depth.

In general, if only the temperature and pressure values are available, it is impossible to correctly predict how impedance changes without knowing the fluid saturations. For example, simply decreasing temperature and pore pressure will increase the acoustic impedance; simply to increase gas saturation will decrease acoustic impedance. These two combined opposite factors will eventually determine the overall impedance variations.

The inverted "impedance" shown in Figure 6.16 can be interpreted based on rock physics as illustrated in Figure 6.17 which is part of Figure 6.7. The selected gas saturation is within the range [0.2, 0.4]. Assume that the point "A" defines conditions in the reservoir with $S_{Me} = 0.25, S_W = 0.55$, and $S_O = 0.2$ in July 2001. From the recorded history data, it is known that from July 2001 to October 2001, gas injection increases and gas production decreases; it is quite possible that the overall gas saturation increases

during this time period. Obviously, the impedance at any point which falls inside the small triangle as shown in 6.17 is larger than the impedance at point "A". If the point "B" is assumed to be representative of reservoir conditions in October 2001, the acoustic impedance increases from "A" to "B". This estimated impedance based on rock physics may be used to interpret that the inverted "impedance" shown in 6.16(a) possibly happens in the field time-lapse seismic monitoring.

From July 2001 to June 2002, gas injection increases and gas production decreases. Therefore, it is reasonable to assume that gas saturation increases during this time period. Therefore, for any point which falls inside the big triangle as shown in 6.17, impedance decreases. If the point "C" is assumed to represent the event occurring in June 2002, the simulated scenario from "A" to "C" can be used in the assistance to interpret the inverted "impedance" shown in frame 6.16(b).

Since the pore temperature and pore pressure in October 2002 are not available at present, the inverted "impedance" shown in 6.16(c) will not be further interpreted in this thesis.

6.5 Summary

In the first part of this chapter, a series of time-lapse rock properties have been calculated based on Gassmann's equation. Then seismic attribute, the power spectrum and the accumulated power spectrum have been estimated from the time-lapse seismic data along the W-E direction and the N-S direction. The small energy variations along the N-S direction may indicate the local dynamic environment and the barely observed energy variations along the W-E direction may reveal the local static environment. Furthermore, the acoustic "impedance" along the N-S direction has been reasonably inverted by using the recently proposed hybrid data transformation method. The inverted acoustic "impedance" is found to increase from July 2001 to October 2001, and from July 2001 to October 2002, but decrease from July 2001 to June 2002. The estimated impedance based on rock physics has shown that the opposite contribution of the increased gas saturation and the simultaneous drop in temperature and pressure have resulted in this mixed impedance variations.

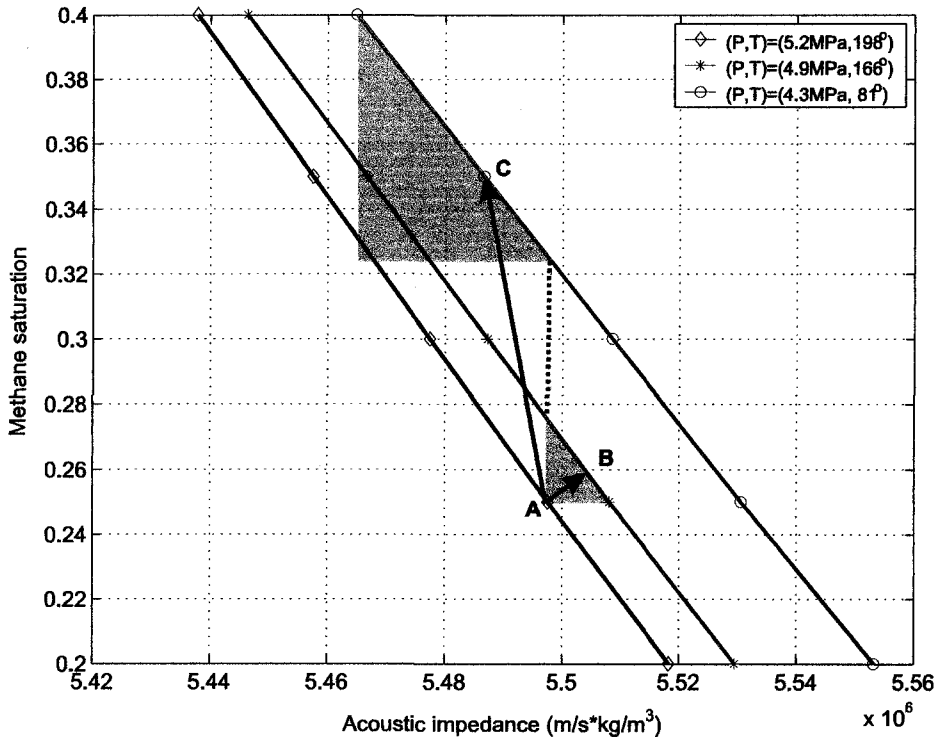

Figure 6.17: Configuration of the simulated time-lapse impedance as a function of gas saturation. Small triangle area represents that impedance increases with gas saturation; big triangle area represents that impedance decreases with gas saturation.

Discussion and Conclusions

Nowadays, exploration of heavy oil has become increasingly important. Due to the special physical properties in these hydrocarbons, special recovery techniques, such as thermal recovery, are required to be used in their commercial oil production. During the process of oil recovery, the subsurface rock property variations are possibly detected by using geophysical methods.

In this case study, several time-lapse seismic surveys were acquired along the W-E and N-S directions in East Senlac area. During the process of seismic data acquisition, the reservoir area was subject to a rather involved SAGD process. In general, during the SAGD process, two horizontal well pairs are drilled close to the bottom of reservoir. Through the top borehole, hot steam is injected into the reservoir area. The steam heats the oil so that the viscosity of the heavy oil reduces significantly and the oil becomes mobile. When the oil density is bigger than the steam density, the viscous oil flows into the bottom borehole where it is produced.

Since the SAGD in this study area has already started for about two years when the first seismic survey was acquired, the communication between the injection borehole and the production borehole should have been completely established. Unfortunately, there was also a great deal of uncertainty as to whether the reservoir was. The main goal of this thesis is to investigate the following question:

1. What risk will be involved in conducting time-lapse seismic monitoring project in East Senlac area?
2. How to evaluate and how to quantify the calendar seismic repeatability?
3. How to process time-lapse seismic signals in a high fidelity manner?

4. How to diagnose and how to interpret the observed time-lapse seismic variations?

5. How to invert the seismic variations into rock property parameters?

The first question of **How big risk will be involved in conducting time-lapse seismic monitoring project in East Senlac area** is mainly related to the subject of feasibility study. It has been systematically examined from four aspects including the prediction of rock property variations, technical risk assessment, generation of forward seismic modelling, and geometry design of seismic data acquisition. Based on Gassmann's equation, the density and the compressional velocity were estimated at different stages of fluid substitutions. In the process of oil substitution by steam, the predicted compressional velocity decreases from the 2957 m/s at 28°C to the 2820 m/s at 263.94 °C. Meanwhile, the density decreases from the 2130 kg/m^3 to the 1890 kg/m^3. The relative compressional velocity variation is -4.6%, and the relative density variation is -11.1%. The risk assessment has been performed by utilizing the technical spreadsheet. Based on this risk analysis, recommendation is made that it is feasible to conduct time-lapse seismic monitoring project in East Senlac area, but great challenge will be encountered due to the existence of the relatively stiff rock matrix within the deeply buried thin reservoir area. Based on the predicted compressional velocity and density, two sets of synthetic seismic data sets were generated by using the 2-D finite difference method. Seismic variations were detected from the seismic difference profiles. In selecting seismic acquisition geometry parameters, it is suggested that the maximum offset should not exceed the reservoir depth. In the East Senlac case, the reservoir depth is about 750 meters. Therefore, the maximum offset should be limited within the 750 meters.

During another process of steam substitution by injected gas with the constant temperature at 263.94 °C and the constant pressure at 5 MPa, the absolute variations in compressional velocity and density are close to zero. In this case, it would be difficult to conduct time-lapse seismic monitoring. That is, one should not expect to recognize difference between water vapor (steam) or methane.

Three metrics were presented to address the second question of **How to evaluate and how to quantify the calendar seismic repeatability**. These metrics include Pearson correlation (PEAR), normalized root mean squares (NRMS), and predictability (PRED).

Better repeatability along the W-E direction than along the N-S direction has been observed from the calculated PEAR profiles. From the further estimated Pear values within the designed window area, the relatively higher values along the W-E direction may demonstrate the local static geologic environment, and the relatively lower PEAR values may indicate the local dynamic geology environment along the N-S direction. The anti-correlated NRMS and PRED values seem to further support these local geology features. The lateral post-stack seismic quality represented by the NRMS values is negatively correlated with the CMP stack fold distribution. The lower stack fold number results in the higher NRMS values which are mainly related to noise. The higher stack fold number, for example, more than 25, corresponds to the lower NRMS values which are mainly related to signals.

The third question of **How to process time-lapse seismic signals in a high fidelity manner** has been clarified by employing different processing strategies. Three category processing strategies are generally included which are the post-stack cross-equalization (XEQ), the prestack parallel processing (PPP), and the prestack simultaneous processing (PSP). The first processing strategy is usually used in the legacy data processing. The second processing strategy PPP lies in using the similar or identical parameters. The third processing strategy PSP is to emphasize the use of identical parameters, and the application of the jointly extracted operators simultaneously to the multi-vintage data. The latter two processing strategies are commonly used in the time-lapse seismic data processing when the calendar surveys are designed for the purpose of time-lapse seismic monitoring. Generally, optimal results can be obtained by using the PSP processing strategy.

The XEQ is another important component in the time-lapse seismic data processing. The matched filtering method (MFM) and the bandwidth-phase equalization method (BPEM) are the two generally used methods. In the application of MFM, small variations are easily erased from seismic difference signals. Since the inherent assumption of the same systematic error existing within the static geology area and within the dynamic geology area may never be satisfied in the real time-lapse seismic monitoring, these two XEQ methods should be used very carefully. For the East Senlac calendar surveys, the two steps of time shifting and amplitude scaling have been adopted in the XEQ.

The Power spectrum as one of the seismic attributes is used to monitor the calendar energy variations. This seismic attribute is used to answer the question **How to diagnose and how to interpret the observed time-lapse seismic variations**. The estimated power spectra along the W-E seismic line direction are found to have very similar shapes. The overall variations are trivial. It is inferred that these calendar seismic surveys are possibly acquired under the static geology environment. In contrast, the main frequencies along the N-S calendar seismic surveys shift slightly. The corresponding power spectra tend to increase with the calendar time interval. This may indicate that these seismic profiles are likely obtained under the dynamic geology environment. The derived accumulated power spectra along these two seismic line directions have further confirmed this observation.

The impedance inversion and rock property simulation are used in order **to invert the seismic variations into rock property parameters**. The hybrid data transformation method is employed to invert for the calendar "impedance". The possible interpretation is assisted by integrating the simulated rock properties. The Gassmann's equation and the recorded history data are employed in this simulation. The acoustic impedance is found to increase from July 2001 to October 2001, and it decreases slightly from July 2001 to June 2002. By combining the simulated time-lapse impedance, the possible increase in gas saturation and the simultaneous drop in temperature and pressure may have made this mixed contribution. Since the history data in October 2002 is not available, the inverted "impedance" from July 2001 to October 2002 will not be interpreted in this thesis.

Future research directions

As time-lapse seismic monitoring covers a variety of topics, the analysis and results presented in this thesis could be extended to accommodate the following aspects:

- **Rock property measurement in laboratory.** This would provide helpful information at the feasibility study stage. The main purpose of this measurement is to simulate the fluid substitution scenario which may occur under the *in situ* reservoir conditions. From the measured rock property parameters, the seismic parameters

including velocity and density can be further estimated. However, these measurements should move toward forced oscillation techniques.

- **Improvement in the seismic data acquisition design.** One relevant aspect is the CMP stack fold distribution. In this case study, the CMP stack fold number changes with CMP position and is distributed in a quasi-triangle shape. This has directly affected the S/N ratio and the lateral seismic event. When the stack fold number is insufficient, the seismic signals will be heavily contaminated with noise. Therefore, in the design of seismic acquisition system, it is important to maintain a uniform stack fold distribution with a reasonable stack fold number.

  Another aspect is in the improvement of seismic resolution. This improvement can be accomplished by increasing the emitted source wavelet frequency and the emitted source energy. In this case study, the main frequency within the target reflection area is about 29 Hz. If higher resolution seismic surveys were acquired, more interesting features might be revealed within the thin reservoir area.

- **Extension of the recently proposed 1-D inversion algorithm to the 2-D or 3-D.** The main challenging technical aspect lies in the design of a two dimensional or three dimensional operator in the deconvolution algorithm.

- **Robust estimation of time-difference and amplitude variations.** In the feasibility study, more robust method such as ray tracing should be adopted in the measurement of the travel time difference at the soil surface. In this case study, the travel time difference is calculated at the reservoir surface which is not easy to assess the relationship between the offset and the time difference at the soil surface.

  Another component is the robust estimation of amplitude variations. In this case study, amplitude variations are predicted based on the *Widess* (1973)'s simple formula. More robust method such as the method based on wave equation should be adopted in the prediction of the amplitude variations since such wave equation represents a better approximation of the subsurface seismic wave propagation.

- **Development of seismic attributes.** In this case study, only the power spectra and the derived accumulated power spectra have been estimated from the calendar seis-

mic surveys since the data set used in this case study had at best only very weak time lapse signals. For the more regular designed time-lapse seismic surveys, a variety of seismic attributes should be be developed and tested from the time-lapse seismic data.

Bibliography

Altan, S., Time-lapse seismic monitoring: Repeatability processing tests, in *SEG annual meeting*, pp. 866–867, SEG, 1997.

Anderson, R. N., A. Boulanger, W. He, L. Xu, P. B. Flemings, T. D. Burkhart, and A. R. Hoover, 4-d time-lapse seismic monitoring in the south timbalier 295 field, gulf of mexico, in *SEG annual meeting*, pp. 868–871, SEG, 1997.

Archer, S., V. Gikas, C. Pinel, D. Ridyard, and P. Cross, 1999, Spatially and temporally correlated navigation errors: how do they manifest themselves in seismic data?, *First Break, 17*, 355–362.

Aritman, B. C., 2001, Repeatability study of seismic source signatures, *Geophysics, 66*, 1811–1817.

Batzle, M., and Z. Wang, 1992, Seismic properties of pore fluids, *Geophysics, 57*, 1396–1408.

Beasley, C. J., R. E. Chambers, R. L. Workman, K. L. Craft, and L. J. Meister, 1997, Repeatability of 3-d ocean-bottom cable seismic surveys, *The Leading Edge, 16*, 1281–1285.

Berryman, J. G., 1999, Origin of gassmann's equations, *Geophysics, 64*, 1627–1629.

Bertrand, A., and C. MacBeth, 2003, Seawater velocity variations and realtime reservoir monitoring, *The Leading Edge, 22*, 351–355.

Biot, M. A., Three-dimensional gravity instability derived from two-dimensional solutions, vol. 31, pp. 153–166, Soc. of Expl. Geophys., 1966.

Butler, R., and C. Yee, 2002, Progress in the situ recovery of heavy oil and bitumen, *J. Can. Pet. Tech., 41*, 31–40.

Chakrabarty, C., J. P. Fossey, G. Renard, and C. Gadelle, SAGD process in the East Senlac field: from reservoir characterization to field application, in 7^{th} *UNITAR conference on heavy crude and tar sands*, Beijing / China, 1998.

Christensen, N. I., and H. F. Wang, 1985a, The influence of pore pressure and confining pressure on dynamic elastic properties of berea sandstone, *Geophysics, 50*, 207–213.

Christensen, N. I., and H. F. Wang, 1985b, The influence of pore pressure and confining pressure on dynamic elastic properties of berea sandstone, *Geophysics, 50*, 207–213.

Christopher, J., Evolution of the Lower Cretaceous Mannville Sedimentary Basin in Saskatchewan., in *In Pemberton, S.G. and James, D.P. (Eds.), Petroleum Geology of the Lower Cretaceous Mannville group, Western Canada*, vol. Memoir 18, pp. 191–210, Canadian Society of Petroleum Geologists, 1997.

Claerbout, J., Earth Soundings Analysis, in *SEP-Report*, vol. 71, pp. 1–304, SEP, 1991.

CSResourcesLimited, Application for an enhanced oil recovery project, senlac, saskatchewan, in *Saskatchewan Energy and Mines*, p. 25, Regina, Saskatchewan, 1995.

Cupcic, F., Extra heavy oil and bitumen impact of technologies on the recovery factor, in *ASPO Annual Meeting*, vol. 1, Rueil, 2003.

Curtis, A., L. Combee, W. Olafsen, and P. Smith, *Acquisition of highly repeatable seismic data using active streamer steering*, pp. 81–84, Soc. of Expl. Geophys., 2002.

Denham, L. R., Field technique design for seismic reflection exploration, in *SEG annual meeting*, SEG, New Orleans, 1979.

Dilay, A., and J. Eastwood, 1995, Spectral analysis applied to seismic monitoring of thermal recovery, *The Leading Edge, 14*, 1117–1122.

Domenico, S. N., 1976, Effect of brine-gas mixture on velocity in an unconsolidated sand reservoir, *Geophysics, 41*, 882–894.

Eastwood, J., 1993, Temperature-dependent propagation of P- and S-waves in Cold Lake oil sands: Comparison of theory and experiment, *Geophysics, 58*, 863–872.

Eastwood, J., P. Lebel, A. Dilay, and S. Blakeslee, 1994, Seismic monitoring of steam-based recovery of bitumen, *The Leading Edge, 13*, 242–251.

Eastwood, J. E., D. Johnston, X. Huang, K. Craft, and R. Workman, Processing for robust time-lapse seismic analysis: Gulf of mexico example, lena field, in *SEG annual meeting*, pp. 20–23, SEG, 1998.

Eberhart-Phillips, D., D. H. Han, and M. D. Zoback, 1989, Empirical relationships among seismic velocity, effective pressure, porosity, and clay content in sandstone, *Geophysics, 54*, 82–89.

Ebrom, D. A., G. Purnell, and P. Krail, Repeatability of marine seismic streamer data for prestack analysis at the orca basin, in *SEG annual meeting*, pp. 59–62, SEG, 1997.

Ebrom, K. P. R. D., D., and L. Scott, 1998, $4 - c/4 - d$ at teal south, *The Leading Edge, 17*, 1450–1453.

Ecker, C., D. E. Lumley, A. Tura, W. Kempner, and L. Klonsky, Estimating separate steam thickness and temperature maps from 4-d seismic data: An example from san joaquin valley, california, in *SEG annual meeting*, pp. 2032–2034, SEG, 1999.

El-Emam, A. H., J. K. Hughes, and H. A. Bunaian, Repeatability of land seismic surveys: A case study from kuwait, in *SEG annual meeting*, pp. 5–8, SEG, 1998.

Eiken, O., H. Aronsen, A. Furre, L. Klefstad, and L. Nordby, *Repeated seismic surveys from the Norwegian Sea using new streamer technology*, pp. 1700–1703, Soc. of Expl. Geophys., 2002.

Gassmann, F., 1951, Elastic waves through a packing of spheres, *Geophysics, 16*, 673–685.

Ghosh, S., 2000, Limitations on impedance inversion of band-limited reflection data, *Geophysics, 65*, 951–957.

Gluck, S., B. Deschizeaux, A. Mignot, C. Pinson, and F. Huguet, Time-lapse impedance inversion of poststack seismic data, in *SEG annual meeting*, pp. 1509–1512, SEG, 2000.

Greaves, R. J., and T. J. Fulp, 1987, Three-dimensional seismic monitoring of an enhanced oil recovery process, *Geophysics, 52*, 1175–1187.

Groeneveld, N., Geology of the lower mannville strata winter-senlac area, western saskatchewan, Unpublished masters thesis, University of Regina, 1990.

Groeneveld, N., and L. Stasiuk, Depositional environment of the cummings coal and associated sediments, winter-senlac area, saskatchewan, in *Oil and Gas in Saskatchewan*, pp. 135–147, 1990.

Han, D. H., A. Nur, and D. Morgan, 1986, Effets of porosity and clay content on wave velocities in sandstones, *Geophysics, 51*, 2093–2107.

Hardage, B. A., Invited introductory paper: Vsp: Where we are and where we are going, in *SEG annual meeting*, p. Session:S13.2, SEG, 1987.

Harris, J. M., R. T. Langan, T. Fasnacht, D. Melton, B. Smith, J. Sinton, and H. Tan, Experimental verification of seismic monitoring of co2 injection in carbonate reservoirs, in *SEG annual meeting*, pp. 1870–1872, SEG, 1996.

Harris, P. E., and B. Henry, Time lapse processing: A north sea case study, in *SEG annual meeting*, pp. 1–4, SEG, 1998.

Hartigan, J., 1983, *Bayes theory*, Springer-Verlag New York, Inc.

He, W., G. Guerin, R. N. Anderson, and U. T. Mello, 1998, Time-dependent reservoir characterization of the lf sand in the south eugene island 330 field, gulf of mexico, *The Leading Edge, 17*, 1434–1438.

Hilterman, F. J., 2001, *Seismic amplitude interpretation*, 235, SEG.

Hirsche, K., M. Batzle, R. Knight, Z. Wang, L. Mewhort, R. Davis, and G. Sedgwick, Seismic monitoring of gas floods in carbonate reservoirs: From rock physics to field testing, in *SEG annual meeting*, pp. 902–905, SEG, 1997.

Hirsche, K. W., and B. Harmony, Time-lapse seismic monitoring of a se asian field-a case history, in *SEG annual meeting*, pp. 24–26, SEG, 1998.

Hughes, J., 2000, Examination of seismic repeatability as a key element of time-lapse seismic monitoring, *SPE RESERVOIR EVALUATION & ENGINEERING, 3*, 517–524.

Ingber, L., 1989, Very fast simulated re-annealing, *Mathl. Comput. Modeling, 12*, 967–993.

Jenkins, S. D., M. W. Waite, and M. F. Bee, 1997, Time-lapse monitoring of the duri steamflood: A pilot and case study, *The Leading Edge, 16*, 1267–1273.

Johnstad, S. E., R. H. Seymour, and P. J. Smith, 1995, Seismic reservoir monitoring over the oseberg field during the period 1989-1992, *First Break, 13*, 169–183.

Johnston, D. H., R. S. McKenny, J. Verbeek, and J. Almond, 1998, Time-lapse seismic analysis of fulmar field, *The Leading Edge, 17*, 1422, 1422–1426, 1428.

Kaaresen, K., and T. Taxt, 1998, Multichannel blind deconvolution of seismic signals, *Geophysics, 63*, 2093–2107.

King, M. S., 1966, Wave velocities in rocks as a function of overburden pressure and pore fluid saturants, *Geophysics, 31*, 56–73.

King, M. S., and J. R. Marsden, 2002, Velocity dispersion between ultrasonic and seismic frequencies in brine-saturated reservoir sandstones, *Geophysics, 67*, 254–258.

Knapp, R. W., and D. W. Steeples, 1986, High-resolution common-depth-point reflection profiling - field acquisition parameter design, *Geophysics, 51*, 283–294.

Kormylo, J., and J. M. Mendel, Maximum-likelihood seismic deconvolution, in *SEG annual meeting*, p. Session:G.77, SEG, 1980.

Koster, K., P. Gabriels, M. Hartung, J. Verbeek, G. Deinum, and R. Staples, 2000, Time-lapse seismic surveys in the north sea and their business impact, *The Leading Edge, 19*, 286–293.

Kragh, E., and P. Christie, *Seismic repeatability, normalized RMS and predictability*, pp. 1656–1659, Soc. of Expl. Geophys., 2001.

Kragh, E., and P. Christie, 2002, Seismic repeatability, normalized rms, and predictability, *The Leading Edge, 21*, 640–647.

Kristiansen, P., P. Christie, J. Bouska, A. O'Donovan, P. Westwater, and E. Thorogood, *Foinaven 4-D: Processing and analysis of two designer 4-Ds*, pp. 1456–1459, Soc. of Expl. Geophys., 2000.

Landro, M., 1999a, Repeatability issues of 3-d vsp data, *Geophysics, 64*, 1673–1679.

Landro, M., Discrimination between pressure and fluid saturation changes from time lapse seismic data, in *SEG annual meeting*, pp. 1651–1654, SEG, 1999b.

Landro, M., 2002, Uncertainties in quantitative time-lapse seismic analysis, *Geophysical Prospecting, 50*, 527–538.

Lavielle, M., 1991, 2-d bayesian deconvolution, *Geophysics, 56*, 2008–2018.

Laws, R., and E. Kragh, Rough seas and time-lapse seismic, in *62th EAGE annual meeting*, vol. Session:L0015, Eur. Assn. Geosci. Eng., 2000.

Lay, T., and T. Wallace, 1995, *Modern global seismology*, Academic Press, New York.

Li, G., G. Purdue, S. Weber, and R. Couzens, 2001, Effective processing of nonrepeatable 4-d seismic data to monitor heavy oil sagd steam flood at east senlac, saskatchewan, canada, *The Leading Edge, 20*, 54–63.

Li, L., Z. Chen, Y. Mu, and X. Chen, 2004, 4d seismic time differences extracted from pre-stack seismic data, *J. Geophys. Eng., 1*, 143–146.

Lumley, D., Time-lapse seismic reservoir monitoring, in *Geophysics*, vol. 66, pp. 50–53, Soc. of Expl. Geophys., 2001.

Lumley, D., A. Nur, S. Strandenes, J. Dvorkin, and J. Packwood, Seismic monitoring of oil production: A feasibility study, in *SEG annual meeting*, pp. 319–322, SEG, 1994.

Lumley, D., A. Nur, S. Strandenes, J. Dvorkin, and J. Packwood, 4-d seismic monitoring of an active steamflood, in *SEG annual meeting*, pp. 203–206, SEG, 1995.

Lumley, D., D. Adams, M. Meadows, S. Cole, and R. Wright, 4d seismic data processing issues and examples, in *73rd Ann. Internat. Mtg.*, pp. 1394–1397, Soc. of Expl. Geophys., 2003.

Lumley, D. E., Seismic time-lapse monitoring of subsurface fluid flow, Phd, Stanford University, 1995.

Lumley, D. E., R. A. Behrens, and Z. Wang, 1997, Assessing the technical risk of a 4-d seismic project, *The Leading Edge, 16*, 1287–1291.

Lumley, D. E., A. G. Nunns, G. Delorme, A. A. Adeogba, and M. F. Bee, Meren field, nigeria: A 4-d seismic case study, in *SEG annual meeting*, pp. 1628–1631, SEG, 1999.

Mavko, G., and T. Mukerji, 1998, Bounds on low-frequency seismic velocities in partially saturated rocks, *Geophysics, 63*, 918–924.

Meunier, J., and F. Huguet, 1998, Cere-la-ronde: A laboratory for time-lapse seismic monitoring in the paris basin, *The Leading Edge, 17*, 1388, 1390, 1392–1394.

Moldoveanu, N., P. van Baaren, D. Addessi, L. Stubbington, and L. Combee, Repeatability of the seismic experiments for 4-d seismic in transition zone surveys, in *SEG annual meeting*, pp. 5–8, SEG, 1996.

Moore, D. E., Using multiple time-lapse 3-d seismic surveys for fluid characterization in consolidated sandstone reservoirs, in *Offshore Technology Conference*, p. 8292, 1997.

Morice, S., S. Ronen, P. Canter, K. Welker, and D. Clark, The impact of positioning differences on 4-d repeatability, in *70th Ann. Internat. Mtg*, pp. 1611–1614, Soc. of Expl. Geophys., 2000.

Mu, R., H. B. Chen, X., and Y. Zhang, Case study from northwest china: application of biot-gassmann's equation to identify sand and isolate oil from the prestack seismic data, in *SEG annual meeting*, pp. 502–505, SEG, 2004.

Nambudiri, E., Palynology of mannville sediments in saskatchewan ii., in *Energy Research Unit Contribution*, 60, p. 37, University of Regina, 1984.

Nur, A., 1989, Four-dimensional seismology and (true) direct detection of hydrocarbons: The petrophysical basis, *The Leading Edge, 8*, 30–36.

Nur, A., C. Tosaya, and D. V. Thanh, Seismic monitoring of thermal enhanced oil recovery processes, in *SEG annual meeting*, p. RS.6, SEG, 1984.

Oldenburg, D. W., T. Scheuer, and S. Levy, 1983, Recovery of the acoustic impedance from reflection seismograms, *Geophysics, 48*, 1318–1337.

Peterson, R. A., W. R. Fillippone, and F. B. Coker, 1955, The synthesis of seismograms from well-log data, *Geophysics, 20*, 516–538.

Porter-Hirsche, J. L., and K. W. Hirsche, Repeatability study of land data acquisition and processing for time lapse seismic, in *SEG annual meeting*, pp. 9–11, SEG, 1998.

Press, W. H., S. A. Teukolsky, W. T. Vetterling, and B. P. Flannery, 1997, *Numerical recipes in C*, 2^{nd} ed., Cambridge University Press, Cambridge.

Pullan, S. E., and J. A. Hunter, Seismic model studies of the overburden bedrock reflection, in *SEG annual meeting*, p. Session:E1.8, SEG, 1983.

Pullin, N., L. Matthews, and K. Hirsche, 1987, Techniques applied to obtain very high resolution three-dimensional seismic imaging at an athabasca tar sands thermal pilot, *The Leading Edge, 6*, 10–15.

Rennie, J., R. Alexandre, and S. Ronen, Sensitivity of repeat 3-d seismic surveys to geometry variations-a controlled experiment, in *SEG annual meeting*, pp. 91–95, SEG, 1997.

Rickett, J., Bandwidth-equalization and phase-matching of time-lapse seismic datasets, in *SEP-Report*, vol. 94, pp. 33–43, SEP, 1997.

Rickett, J., and D. E. Lumley, A cross-equalization processing flow for off-the-shelf 4-d seismic data, in *SEG annual meeting*, pp. 16–19, SEG, 1998.

Rickett, J., and D. E. Lumley, Cross-equalization data processing for time-lapse seismic reservoir monitoring: A case study from the gulf of mexico, vol. 66, pp. 1015–1025, 2001.

Rokosh, C., and D. Schmitt, Geology and production history of the senlac area, in *Shoc report 2002*, edited by D. R. Schmitt, Edmonton, 2002.

Ross, C. P., and M. S. Altan, 1997, Time-lapse seismic monitoring: Some shortcomings in nonuniform processing, *The Leading Edge, 16*, 931–937.

Ross, C. P., G. B. Cunningham, and D. P. Weber, 1996, Inside the cross-equalization black box, *The Leading Edge, 15*, 1233–1240.

Sarkar, S., W. Gouveia, and D. Johnston, On the inversion of time-lapse seismic data, in *SEG annual meeting*, pp. 1489–1492, SEG, 2003.

Schmitt, D. R., 1999, Seismic attributes for monitoring of a shallow heated heavy oil reservoir: A case study, *Geophysics, 65*, 368–377.

Sengbush, R. L., P. L. Lawrence, and F. J. McDonal, 1961, Interpretation of synthetic seismograms, *Geophysics, 26*, 138–157.

Smith, T., C. Sondergeld, and C. Rai, 2003, Gassmann fluid substitutions: A tutorial, *Geophysics, 68*, 430–440.

Sonneland, L., H. H. Veire, B. Raymond, C. Signer, L. Pedersen, S. Ryan, and C. Sayers, 1997, Seismic reservoir monitoring on gullfaks, *The Leading Edge, 16*, 1247–1252.

Talley, D. J., T. L. Davis, R. D. Benson, and S. L. Roche, 1998, Dynamic reservoir characterization of vacuum field, *The Leading Edge, 17*, 1396, 1398–1400, 1402.

Theune, U., Characterization of the rock physics of the senlac reservoir and feasibility testing of seismic monitoring, in *Shoc report 2003*, edited by D. R. Schmitt, Edmonton, 2003.

Theune, U., Seismic monitoring of heavy oil reservoir: rock physics and finite element modelling, Phd, University of Alberta, 2004.

Theune, U., and D. Schmitt, 2004, A comparative case study of the effects of steam injection on seismic responses in differing heavy oilr eservoirs: implications for the feasibility of seismic monitoring, *submitted to Geophysics*.

Thompson, M., and N. Najjar, Improved time-lapse seismic repeatability and impact on quantitative analysis - statfjord field, in *64th EAGE Mtg.*, p. P316, Eur. Assn. Geosci. Eng., 2002.

Timur, A., 1977, Temperature dependence of compressional and shear wave velocities in rocks, *Geophysics, 42*, 950–956.

Tura, A., and D. E. Lumley, 1998, Subsurface fluid flow properties from time-lapse elastic wave reflection data, *Mathematical Methods in Geophysical Imaging, 5*, 125–138.

Tura, A., and D. E. Lumley, Estimating pressure and saturation changes from time-lapse avo data, in *61st Conf. And Tech. Exhibit*, pp. 1–38, Eu. Assn. Geosci. Eng., 1999a.

Tura, A., and D. E. Lumley, Estimatingpressure and saturation changes from time-lapse avo data, in *SEG annual meeting*, pp. 1655–1658, SEG, 1999b.

Vesnaver, A., F. Accaino, G. Bohm, G. Madrussani, J. Pajchel, G. Rossi, and G. Dal Moro, Time-lapse tomography, in *Geophysics*, vol. 68, pp. 815–823, Soc. of Expl. Geophys., 2003.

Waite, M. W., and R. Sigit, 1997, Seismic monitoring of the duri steamflood: Application to reservoir management, *The Leading Edge, 16*, 1275–1278.

Walls, J. D., J. Dvorkin, and B. A. Smith, Modeling seismic velocity in ekofisk chalk, in *SEG annual meeting*, pp. 1016–1019, SEG, 1998.

Wang, Z., 1997, Feasibility of time-lapse seismic reservoir monitoring: The physical basis, *The Leading Edge, 16*, 1327–1329.

Wang, Z., and A. Nur, Effect of temperature on wave velocities in sands and sandstones with heavy hydrocarbons, in *SEG annual meeting*, p. session BHG1.2, SEG, 1986.

Wang, Z., and A. Nur, Effect of temperature on wave velocities in sands and sandstones with heavy hydrocarbons, in *Seismic and Acoustic Velocities in Reservoir Rocks*, edited by A. Nur and Z. Wang, vol. 1 of *Geophysics reprint series*, pp. 188–194, Soc. of Expl. Geophys., 1988.

Wang, Z., and A. Nur, 1990, Wave velocities in hydrocarbon-saturated rocks: Experimental results, *Geophysics, 55*, 723–733.

Wang, Z., M. E. Cates, and R. T. Langan, 1998, Seismic monitoring of a co2 flood in a carbonate reservoir: A rock physics study, *Geophysics, 63*, 1604–1617.

Whitcombe, D., J. Marsh, G. Bagley, A. Lewis, J. McGarrity, T. Nash, R. Parr, and I. Saxby, *Systematic application of 4-D in BP's NW Europe operations*, pp. 1608–1611, Soc. of Expl. Geophys., 2001.

White, R. E., Partial coherence matching of synthetic-seismograms with seismic traces, in *Geophys. Prosp.*, vol. 28, pp. 333–358, Eur. Assn. Geosci. Eng., 1980.

Widess, M. B., 1973, How thin is a thin bed, *Geophysics, 38*, 1176–1254.

Winkler, K. W., 1985, Dispersion analysis of velocity and attenuation in Berea sandstone, *J. Geophys. Res., 90*, 6793–6800.

Wyllie, M. R. J., A. R. Gregory, and G. H. Gardner, 1958, An experimental investigation of factors affecting elastic wave velocities in porous media, *Geophysics, 23*, 459–493.

Yee, C., and A. Stroich, 2004, Flue gas injection into a mature sagd steam chamber at the dover project (formerly utf), *JOURNAL OF CANADIAN PETROLEUM TECHNOLOGY, 43*, 54–61.

Zaitlin, B. A., and B. Schultz, *Wave-influenced Estuarine Sand Body, Senlac Heavy Oil Pool, Saskatchewan, Canada*, pp. 363–386, Springer-Verlag, New York, 1990.

Zhang, Y., and D. Schmitt, Cross-equalization in time-lapse seismic data processing, in *CSEG Convention*, CSEG, Calgary, 2002.

Zhang, Y., and D. Schmitt, A comparison between local and global inversion of poststack seismic data to estimate acoustic impedance, in *SEG annual meeting*, pp. 738–741, SEG, 2003a.

Zhang, Y., and D. Schmitt, Strategies for the acquisition and processing of high-fidelity time-lapse seismic data, in *CSPG/CSEG Convention*, CSPG/CSEG, Calgary, 2003b.

Zhang, Y., and D. Schmitt, Time-lapse impedance inversion using hybrid data transformation and the spike deconvolution method, in *SEG annual meeting*, pp. 2303–2306, SEG, 2004a.

Zhang, Y., and D. Schmitt, A case study: Qc analysis of time-lapse seismic monitoring in a heavy oil reservoir, in *CSEG National Convention*, CSEG, 2004b.

Zhang, Y., and D. Schmitt, A new method to invert time-lapse impedance using hybrid data transformation, in *CSEG National Convention*, CSEG, 2005a.

Zhang, Y., and D. Schmitt, Quantitative evaluation of the quality of seismic repeatability: a case study using differing metrics, in *CSPG/CSEG/CWLS Annual Convention*, CSPG/CSEG/CWLS, 2005b.

Zhang, Y., D. Schmitt, and C. Rokosh, High resolution seismic monitoring of a heavy oil reservoir, in *CSPG National Convention*, CSPG, Calgary, 2002.

Zou, Y., and L. Bentley, 2003, Time lapse well log analysis, fluid substitution and avo, *The Leading Edge*, 22, 550–555.

Appendix A

Derivation of time differences from time-lapse pre-stack seismic data

Assume that the earth consists of horizontal layers, travelling time through reservoir before and after rock properties change can be written as,

$$t_1^2 = \frac{4h^2 + x^2}{v_1^2} \tag{A.1}$$

and

$$t_2^2 = \frac{4h^2 + x^2}{v_2^2} \tag{A.2}$$

where h is the reservoir thickness, x is the offset, v_1 and v_2 are the travelling velocities before and after reservoir property changes, and t_1 and t_2 are the corresponding travel times. Equation A.2 minus equation A.1, we get,

$$t_2^2 - t_1^2 = (4h^2 + x^2)(\frac{1}{v_2^2} - \frac{1}{v_1^2}) \tag{A.3}$$

Equation A.3 can also be written as,

$$(t_1 + t_2)\Delta t = -\frac{(4h^2 + x^2)(v_1 + v_2)\Delta v}{v_1^2 v_2^2} \tag{A.4}$$

where $\Delta t = t_2 - t_1$ and $\Delta v = v_2 - v_1$. Writing the equation A.4 in a differential form, we get,

$$dt = -\frac{(4h^2 + x^2)dv}{v_1^3 t_1} \tag{A.5}$$

Assume that reservoir thickness does not change before and after rock property variation, reservoir thickness can be written as the following equation,

$$h = \frac{v_1 t_{01}}{2} = \frac{v_2(t_{01} + \Delta t_0)}{2} \tag{A.6}$$

where t_{01} represents two-way vertical travel time, and Δt_0 represents vertical time difference. Since reservoir thickness does not change and we can set $dv = dv_1$, differentiate the first part of equation, we get, A.6, we get,

$$dh = \frac{v_1 dt_{01}}{2} + \frac{t_{01} dv}{2} = 0 \tag{A.7}$$

which leads to

$$\frac{v_1}{t_{01}} = -\frac{dv}{dt_{01}} \tag{A.8}$$

In equation A.8, the negative sign means that as velocity increases, vertical time difference decreases. From equation A.8, velocity variation dv can be written as,

$$dv = -\frac{v_1 dt_{01}}{t_{01}} \tag{A.9}$$

Substitute the formula A.9 into the equation A.5, we obtain,

$$dt = \frac{t_{01}(1+k)dt_{01}}{t_1} \tag{A.10}$$

where $k = x^2/(4h^2)$.

Appendix B

Sparse spike deconvolution by using iterated window maximization (IWM)

Here, we use the iterated window maximization (IWM) based sparse spike deconvolution method to invert the time-lapse difference in reflectivity. This method was compared with different methods such as SA, and demonstrating that this algorithm is more stable and faster than other methods (*Kaaresen and Taxt*, 1998).

In this method, the source wavelet is fixed and the reflectivity model assumes that only a limited number of reflection coefficients have non-zero values. Such signals are usually called "sparse spike trains". Such models can be found in time-lapse seismic monitoring in which case variations only occur within small region. In the derivation, maximum a posteriori (MAP) is estimated based on Bayesian theory. The optimization can be separated into two subproblems: the detection of the reflector times t and the estimation of the reflector amplitudes R for the given t.

In seismic exploration, the seismic response may be approximated by convolving the source signature wavelet with the reflectivity time series in a discrete form:

$$d(n) = \sum_{k=-\infty}^{\infty} w(n-k)r(k) + e(n) \tag{B.1}$$

where w represents the source wavelet, r the reflectivity, e the additive noise, and d the seismic response. Rewriting the above formula in a matrix form,

$$\mathbf{D=WR+E} \tag{B.2}$$

If considered in a time-lapse scenario, **W** represents the source wavelet, **R** the time-lapse reflectivity difference, **E** the additive time-lapse noise, and **D** the time-lapse seismic difference. Assume that a window w which is used to maximize the posterior density has been chosen. Partition **t** into two parts, consisting of those components t^w inside the window and those components $t^{\bar{w}}$ outside the window, respectively. Partition **a** in the similar way. Let W^w be the columns of **W** corresponding to reflectors inside the window and $W^{\bar{w}}$be the columns corresponding to reflectors outside the window. Let $\gamma_r = \sigma_e^2/\sigma_r^2$ which is the inverse S/N ratio. Now introduce the matrices:

$$S^w = (W^w)'(W^w) + \gamma_r I \tag{B.3}$$

and

$$v^w = (W^w)'D - (W^w)'W^{\bar{w}}r^{\bar{w}} \tag{B.4}$$

The optimal value of $\hat{r}^w$, given $r^{\bar{w}}$, **t**, and **D**, is

$$\hat{r}^w = (S^w)^{-1}v^w \tag{B.5}$$

The $(t^w, \hat{r}^w)$ pair corresponding to the largest value of the posterior is the one that yields the larger value of the criterion

$$l(\vec{t}) = (v^w)'\hat{r}^w + g(\vec{t}) \tag{B.6}$$

In the above formula, the first term measures the fit to the data, and the second term $g(\vec{t})$ is the regularization or penalty term. Under the Bernoulli-Gaussian assumption, this term can be expressed the particularly simple form

$$g(\vec{t}) = -\theta M^w \tag{B.7}$$

where M^w is the number of reflectors inside the window and the θ is the sparsity parameter which is usually within the range [10, 20].

The correlation functions can be computed and stored prior to the iterations. These functions can be written as

$$c_{ww} = \sum_{k=n}^{K} W(k-n)W(k)(n = 0, 1, ..., K) \tag{B.8}$$

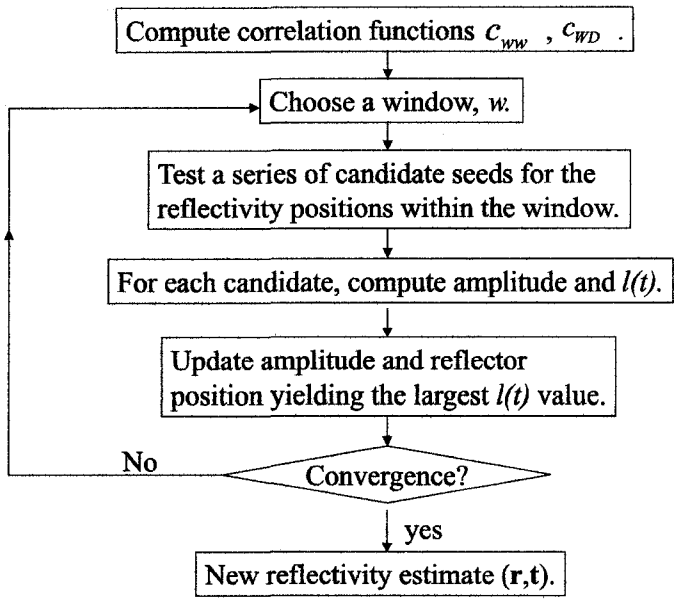

Figure B.1: The procedure to calculate reflectivity.

and

$$c_{WD} = \sum_{k=max(1,n)}^{min(N,n+K)} W(k-n)D(k)(n=0,1,...,N) \tag{B.9}$$

Using these functions, the initialization can be written as

$$S_{ij}^{w} = c_{ww}(|t_i^w - t_j^w|) + \gamma_r \delta(i-j) \tag{B.10}$$

and

$$v_i^w = c_{WD}(t_i^w) - \sum_{l} r_l^{\bar{w}} c_{ww}(|t_i^w - t_l^{\bar{w}}|) \tag{B.11}$$

for $i, j = 1, 2, ..., M^w$. The detailed process to calculate reflectivity is illustrated in Figure B.1.

Appendix C

Wavelet estimation by using the least-squares method

Seismic response can be written in a matrix format:

$$\mathbf{D} = \mathbf{RW} + \mathbf{E} \tag{C.1}$$

Here, the **D**, **R**, **W**, and **E** individually represents seismic response, reflectivity, source wavelet, and additive noise.

Based on the Gaussian assumptions on **R** and **E**, in this linear model, the maximum a posteriori estimator can be written as (see *Hartigan* (1983)):

$$\hat{\mathbf{W}} = (\mathbf{R}'\mathbf{R} + \gamma_w \mathbf{I})^{-1}\mathbf{R}'\mathbf{D} \tag{C.2}$$

The parameter $\gamma_w = \sigma_e^2/\sigma_r^2$ is an inverse S/N ratio (σ_e^2 represents variance in error; σ_r^2 represents variance in signal). When $\gamma_w = 0$, solution C.2 reduces to the standard least-squares estimate; when γ_w is a constant, solution C.2 reduces to the damped least-squares estimate.